RICE UNIVERSITY

Representation and Estimation of Seismic Sources via Multipoles

by

Mario J. Bencomo

A Thesis Submitted
in Partial Fulfillment of the
Requirements for the Degree
Doctor of Philosophy

Approved, Thesis Committee:

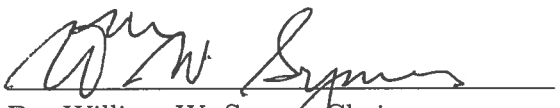

Dr. William W. Symes, Chair
Noah G. Harding Professor of
Computational and Applied Mathematics
Professor of Earth Science

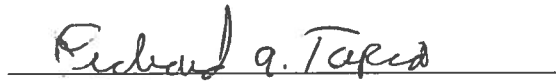

Dr. Richard A. Tapia
University Professor
Maxfield-Oshman Professor in
Engineering
Professor of Computational and Applied
Mathematics

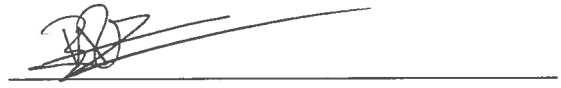

Dr. Béatrice M. Rivière
Noah G. Harding Chair
Department Chair of Computational and
Applied Mathematics

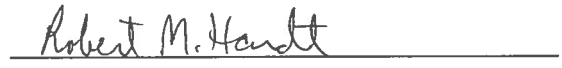

Dr. Robert Hardt
W.L. Moody Professor of Mathematics

Houston, Texas
March, 2017

ABSTRACT

Representation and Estimation of Seismic Sources via Multipoles

by

Mario J. Bencomo

Accurate representation and estimation of seismic sources are essential to the seismic inversion problem. General sources can be approximated by a truncated series of multipoles depending on the source anisotropy. Most research in the joint inversion of source and medium parameters assumes seismic sources can be modeled as isotropic point-sources resulting in an inability to fit the anisotropy observed in data, ultimately impacting the recovery of medium parameters. In this thesis I lay the groundwork for joint source-medium parameter inversion with potentially anisotropic seismic sources via full waveform inversion through three key contributions: a mathematical and computational framework for the modeling and inversion of sources via multipoles, construction and analysis of discretizations of multipole sources on regular grids, and preconditioners based on fractional time derivative/integral operators for the ill-conditioned source estimation subproblem. As an application of my multipole framework, I also study the efficacy of multipoles in modeling the airgun array source, the most common type of active source in marine seismic surveying. Inversion results recovered a dominating isotropic component of the multipole source model that accounted for 84% of the observed radiation pattern. An extra 10% of the observed output pressure field can be explained when incorporating dipole terms in the source representation, thus motivating the use of multipoles to capture source anisotropy.

Acknowledgements

My graduate school years have indeed been arduous and yet some of the most gratifying ones of my life. There are many people I would like to thank for guiding and supporting me through this journey.

Firstly, I would like to thank my advisor, Dr. William W. Symes, for being a tremendous source of guidance and inspiration during my academic development at Rice. This thesis is the culmination of my work and his mentorship. One of the many lessons that I have learned under his supervision is that a successful career in mathematics need not come at the cost of personality, accessibility or compassion, but in fact can be complemented by these traits. I would also like to thank Dr. Béatrice M. Rivière, Dr. Robert Hardt, and Dr. Richard A. Tapia for serving as members of my thesis committee and their contributions to my graduate school experience outside of the Ph.D. project. In particular, Dr. Rivière has been an excellent instructor and mentor during my first years at Rice; I especially enjoyed taking her finite elements course. I have also enjoyed the many courses I have taken in the math department, particularly those taught by Dr. Hardt, i.e., functional analysis and PDEs. Lastly, I am very thankful to Dr. Tapia for his invaluable mentorship and ever continuing support. Throughout the years Dr. Tapia and his wife, Jean, have graciously opened their home to me during holidays, birthdays, and celebrations of all sorts. The sense of community that Dr. Tapia has established was one of the main factors that drove me to pursue a graduate degree at Rice and has also been what has sustained me through the years. Thank you, Dr. Tapia.

None of this work would have been possible if it were not for the financial support I have received throughout my tenure. I would like to thank the *Richard Tapia*

Center for Excellence and Equity for their support during my first and last years of graduate school through the *Alliances for Graduate Education and the Professoriate* (AGEP), *Rice Graduate Education for Minorities* (RGEM), and XSEDE scholarship programs. These programs have been fundamental not only to my research but also to my professional development. I would also like to thank the *NSF Graduate Research Fellowship* program for funding during some of my core years at Rice. Lastly, I would like to thank sponsors of *the Rice Inversion Project* (TRIP) for their continuing financial support of the research group over the years.

My time at Rice would not have been the same without my friends and coworkers. In particular, the administrative staff of the CAAM department has been extremely accommodating and professional. Special thanks to Daria Lawrence and Ivy Gonzalez for all their help. I would also like to thank my fellow research members from TRIP, graduate students from the CAAM department, and my officemates over the years. I especially thank Cynthia Woods for her help when I was applying for the NSF fellowship, working late nights editing my research proposal. Above all, thank you for your friendship Cynthia!

My advice for first-year graduate students would be to nurture a hobby outside of graduate school, something that will provide perspective and will complement the graduate school experience. I am deeply grateful to Rice University's Mariachi Luna Llena for being my anchor and giving me the opportunity to express myself through mariachi music. I am not sure if I would have made it if it were not for the mariachi group.

Last, but not least, I want to thank my mother, Gabriela Sanchez. I am forever grateful for the sacrifices she has made in her life in the prospect of a better future for her children.

Contents

Abstract ii

Acknowledgements iii

List of Illustrations vii

List of Tables xiii

1 Introduction 1

1.1 Motivation 2

1.2 Contributions 6

2 Multipole Source Representation 9

2.1 Introduction 9

2.2 Multipole Representation: Multipole Spaces 11

3 Singular Source Approximation 19

3.1 Introduction 19

3.2 (Continuous) Moment Conditions 21

3.3 Discrete Moment Conditions 26

3.3.1 Tensor Product Construction 28

3.3.2 Relating Discrete and Continuous Moments Conditions 33

3.4 Examples 38

4 Wave Modeling with Multipole Sources 41

4.1 Introduction 41

4.2 Singular Source Approximation and Energy Conservative FD Schemes 44

4.3 Computational Framework 48
4.4 Numerical Convergence Rate Tests 62

5 Multipole Source Inversion 78
5.1 Introduction 78
5.2 Multipole Source Estimation via FWI 80
5.3 Preconditioners 83
5.4 Numerical Experiments 86

6 Airgun Array Sources 113
6.1 Background 113
6.2 Modeling 117
6.3 Preliminary Inversions 119

7 Conclusions 134

A Multipole Sources and Seismic Moment Tensors 138

B Analytical Solutions to Wave Equation with Multipole Sources 144

C Fractional Derivative/Integral Operators 152

Bibliography 154

Illustrations

3.1 Plots of η_H, 1-D approximations to $D^s\delta$ with $h = 1$. 39

3.2 Plots of η_H, 2-D approximations to $D^{\mathbf{s}}\delta$ with $h = 1$. 40

4.1 Staggered space-time grid distribution of gridded functions p^h, v_1^h, v_2^h for the 2-2 and 2-4 staggered grid method. 45

4.2 $5Hz$ peak frequency Ricker wavelet. 64

4.3 Physical domain and source-receiver geometry specifications for 2-D convergence rate tests; constant density ($1g/cm^3$) and velocity ($3km/s$) medium, receiver positions $\mathbf{x}_{i_r} = (-200m, 0m : 40m : 6000m)$, source position $\mathbf{x}^* = (-203m, 3003m)$. Receivers and source depicted by a dashed line and a cross, respectively. 64

4.4 Physical domain and source-receiver geometry specifications for 3-D convergence rate tests; constant density ($1g/cm^3$) and velocity ($3km/s$) medium, receiver positions $\mathbf{x}_{i_r} = (-200m, 0m : 40m : 6000m, 100m)$, source position $\mathbf{x}^* = (-203m, 3003m, 103m)$. Receivers and source depicted by a dashed line and a cross, respectively. 65

4.5 Pressure field traces (2-D acoustics) using 2-4 finite difference scheme (with $h = 10m$ and $\Delta t = 0.5ms$) and fourth-order source approximation for scalar multipole of type $f(\mathbf{x}, t) = w_1(t)D^{\mathbf{s}}\delta(\mathbf{x} - \mathbf{x}^*)$. 67

4.6 Approximate convergence rates of finite difference solutions to 2-D acoustics (pressure data only) using 2-2 scheme and second-order source approximation for scalar multipole of type $f(\mathbf{x},t) = w_1(t)D^{\mathbf{s}}\delta(\mathbf{x}-\mathbf{x}^*)$. Rates computed using L^2 (solid blue) and L^∞ (−− red) norms. 68

4.7 Approximate convergence rates of finite difference solutions to 2-D acoustics (pressure data only) using 2-4 scheme and fourth-order source approximation for scalar multipole of type $f(\mathbf{x},t) = w_1(t)D^{\mathbf{s}}\delta(\mathbf{x}-\mathbf{x}^*)$. Rates computed using L^2 (solid blue) and L^∞ (−− red) norms. 69

4.8 Approximate convergence rates of finite difference solutions to 2-D acoustics (pressure data only) using 2-4 scheme and second-order source approximation for scalar multipole of type $f(\mathbf{x},t) = w_1(t)D^{\mathbf{s}}\delta(\mathbf{x}-\mathbf{x}^*)$. Rates computed using L^2 (solid blue) and L^∞ (−− red) norms. 70

4.9 Pressure field traces (3-D acoustics) using 2-4 finite difference scheme (with $h = 10m$ and $\Delta t = 0.5ms$) and fourth-order source approximation for scalar multipole of type $f(\mathbf{x},t) = w_1(t)D^{\mathbf{s}}\delta(\mathbf{x}-\mathbf{x}^*)$. 71

4.10 Approximate convergence rates of finite difference solutions to 3-D acoustics (pressure data only) using 2-2 scheme and second-order source approximation for scalar multipole of type $f(\mathbf{x},t) = w_1(t)D^{\mathbf{s}}\delta(\mathbf{x}-\mathbf{x}^*)$. Rates computed using L^2 (solid blue) and L^∞ (−− red) norms. 72

4.11 Approximate convergence rates of finite difference solutions to 3-D acoustics (pressure data only) using 2-4 scheme and fourth-order source approximation for scalar multipole of type $f(\mathbf{x},t) = w_1(t)D^{\mathbf{s}}\delta(\mathbf{x}-\mathbf{x}^*)$. Rates computed using L^2 (solid blue) and L^∞ (−− red) norms. 73

4.12 Approximate convergence rates of finite difference solutions to 3-D acoustics (pressure data only) using 2-4 scheme and second-order source approximation for scalar multipole of type $f(\mathbf{x},t) = w_1(t)D^{\mathbf{s}}\delta(\mathbf{x}-\mathbf{x}^*)$. Rates computed using L^2 (solid blue) and L^∞ ($--$ red) norms. 74

5.1 Time trace and frequency spectrum of $10Hz$ peak frequency Ricker and derivative of Gaussian wavelet. 90

5.2 Medium and source-receiver geometry specifications for 2-D and 3-D source inversion test with homogeneous medium parameters, constant density ($1kg/m^3$) and velocity ($3km/s$). Receivers and source depicted by dashed lines and a crosses respectively. 91

5.3 Pressure time traces used as "observed data" in source inversions of the type $f(\mathbf{x},t) = w_1(t)D^{\mathbf{s}}\delta(\mathbf{x}-\mathbf{x}^*)$ in 2-D and 3-D. Homogeneous unbounded model test case. 92

5.4 Estimated MPS coefficient w_1 for scalar multipoles of type $f(\mathbf{x},t) = w_1(t)D^{\mathbf{s}}\delta(\mathbf{x}-\mathbf{x}^*)$ in 2-D and 3-D. True solution (solid blue) and estimated solution via CGNE with ($--$ black) and without ($-\cdot-$ red) preconditioning. 93

5.5 CGNE convergence plots for source estimation of scalar multipoles of type $f(\mathbf{x},t) = w_1(t)D^{\mathbf{s}}\delta(\mathbf{x}-\mathbf{x}^*)$ in 2-D and 3-D test cases. Log of L^2-norms (in data and MPS space resp.) of residuals (red/top) and gradients (blue/bottom) plotted for CGNE iterates with (solid) and without ($--$) preconditioning. 94

5.6 Pressure time traces used as "observed data" in source inversions for mixed first-order multipole in 2-D and 3-D. Homogeneous unbounded model test case. 98

5.7 Pressure time traces used as "observed data" in source inversions for mixed first-order multipole in 3-D with better data coverage. Homogeneous unbounded model test case. 98
5.8 Estimated MPS coefficients for scalar mixed first-order multipole in 2-D. True solution (solid blue) and estimated solution via CGNE with ($--$ black) and without ($-\cdot-$ red) preconditioning. 99
5.9 Estimated MPS coefficients for scalar mixed first-order multipole in 3-D. True solution (solid blue) and estimated solution via CGNE with ($--$ black) and without ($-\cdot-$ red) preconditioning. 100
5.10 Estimated MPS coefficients for scalar mixed first-order multipole in 3-D with better data coverage. True solution (solid blue) and estimated solution via CGNE with ($--$ black) and without ($-\cdot-$ red) preconditioning. 101
5.11 CGNE convergence plots for source estimation of scalar mixed first-order multipoles in 2-D and 3-D. Log of L^2-norms (data and MPS space resp.) of residuals (red/top) and gradients (blue/bottom) plotted for CGNE iterates with (solid) and without ($--$) preconditioning. 102
5.12 CGNE convergence plots for source estimation of scalar mixed first-order multipole in 3-D with better data coverage. Log of L^2-norms (data and MPS space resp.) of residuals (red/top) and gradients (blue/bottom) plotted for CGNE iterates with (solid) and without ($--$) preconditioning. 102
5.13 Dome model and source-receiver geometry specifications for 2-D mixed multipole source inversion with reflection setup. 105
5.14 Pressure time traces used as "observed data" in source estimation for scalar mixed first order multipole in 2-D with dome model and reflection source-receiver setup. 106

5.15 CGNE convergence plots or scalar mixed first-order multipole in 2-D with dome model and reflection source-receiver setup. Log of L^2-norms (data and MPS space resp.) of residuals (red/top) and gradients (blue/bottom) plotted for CGNE iterates with (solid) and without $(--)$ preconditioning. 106
5.16 Estimated MPS coefficients for scalar mixed first order multipole in 2-D with dome model and reflection source-receiver setup. True solution (solid blue) and estimated solution via CGNE with $(--$ black) and without $(-\cdot-$ red) preconditioning. 107

6.1 Diagram of oscillating bubble phenomenon, p_{int} and p_{ext} denoting interior and exterior pressures with respect to the bubble, and $R(t)$ is the radius of the bubble as a function of time. 114
6.2 Illustrative source signature for single in time domain and its amplitude spectrum. 116
6.3 Illustrative source signature of an airgun array. 117
6.4 Configuration of airgun array and source-receiver geometry for numerical tests. 121
6.5 Notional airgun signatures computed from AGORA. 122
6.6 Processed notional airgun signatures into point-source wavelets. . . . 122
6.7 Low pass filtered (cutoff at $30Hz$) observed data from airgun array, simulated by solving acoustic equations in first order form with $c = 1.5km/s$, $\rho = 1.024g/cm^3$, using 2-4 staggered grid finite difference with $\Delta x = 5m$ and $\Delta t = 1ms$. 124
6.8 Data residual from recomputed time-traces with estimated multipole sources. 127

6.9 Comparison of observed data (solid-blue) at trace number 300 with recomputed data using estimated multipoles of order zero (dashed-black) and order one (dotted-red). 128
6.10 Estimated MPS coefficient w_1 for isotropic point-source case and its signature. 128
6.11 Estimated MPS coefficients for multipole source of order at most one. 129
6.12 Signature of estimated MPS coefficients for multipole source of order at most one. 130

A.1 Body V with surface ∂V and internal surface Σ oriented by ν. 139
A.2 Corresponding point-couples for different $\mathcal{M}_{pq}$ components. 141

B.1 Pressure waveforms (left column) and fractional time derivatives (right column) related to scalar multipole source $f(\mathbf{x},t) = w_1(t)D^{\mathbf{s}}\delta(\mathbf{x}-\mathbf{x}^*)$ in a 2-D homogeneous unbounded acoustic medium. MPS coefficient $w_1(t)$ is a Ricker wavelet with peak frequency of $10Hz$. Source location $\mathbf{x}^* = (-1km, 1km)$ and receiver location $\mathbf{x}_r = (-800m, 800m)$. 151

Tables

5.1 Summary of results for single scalar MPS inversions with and without preconditioning, containing data residual reduction, gradient reduction, and errors in MPS coefficients with respect to $\|\cdot\|_{\mathfrak{W}}$ and $\|\cdot\|_{\mathfrak{W}'}$ norms. 108

5.2 Summary of results for mixed scalar multipole source inversions with and without preconditioning, containing data residual reduction, gradient reduction, and errors in MPS coefficients with respect to $\|\cdot\|_{\mathfrak{W}}$ and $\|\cdot\|_{\mathfrak{W}'}$ norms. 3-D hom.+ refers to 3-D test case with optimal/improved data coverage. 109

6.1 Airgun array parameters for numerical tests. 123

B.1 Analytical solutions to wave equation with multipole point sources in 1-D, 2-D, and 3-D. 149

Chapter 1

Introduction

The seismic inversion problem consists of recovering geophysical information about the subsurface of the earth given data in the form of recorded pressure or particle displacement/velocity field perturbations or in other words *seismic waves*. These waves are generated by *seismic sources* whose nature can vary from man-made sources, such as airgun arrays in marine seismic surveying, to naturally occurring sources, for example, earthquakes in global seismology. Characteristics of the seismic source, that is its spatial and temporal distribution and anisotropy, are inextricably linked to seismic data, thus an accurate representation and estimation of seismic sources are essential to the seismic inversion problem.

General seismic sources can be approximated by a truncated series of *multipole sources* depending on the complexity of the source output. Most research in joint determination of source and medium parameters model the source as isotropic and of point support resulting in an inability to fit the anisotropy observed in data, ultimately impacting the recovery of model parameters. In this thesis, I propose a mathematical and computational framework for the modeling and inversion of seismic sources represented as linear combinations of multipoles, the groundwork for joint source-medium inversion of arbitrarily anisotropic sources. In particular, I focus on

tackling the difficulties arising from finite difference discretizations of PDE's involving singular source terms and the ill-conditioning of the multipole source estimation subproblem.

1.1 Motivation

Seismic data contain information about source and receiver responses as well as properties of the earth's medium, the latter being of priority in exploration seismology. Conventional methodology initially focused on removing the source response from data as a preprocessing step in seismic imaging by estimating the source signature through statistical methods like predictive deconvolution (Robinson, 1957) and homomorphic deconvolution (Ulrych, 1971). Ziolkowski has criticized these statistical methods for imposing unrealistic and at times theoretically unjustifiable constraints on both the source and medium, yielding results vulnerable to subjectivity, (Ziolkowski, 1991). Alternatively, source signatures for the Vibroseis^{TM} and airgun arrays have been estimated using near-field measurements with some success, see Ziolkowski (1991) and Landrø and Sollie (1992). It should be noted that source estimation with near-field measurements still depends on how the source is modeled (i.e., represented mathematically) and the data's dependency on the medium which can be unknown in applications where the source-receiver path is partially submerged in unknown medium or the direct arrival cannot be clearly discerned from the data.

Starting in the late 1980's, efforts in decoupling source-medium interactions shifted

from preprocessing the source signature out of seismic traces to the joint inversion of source and medium parameters. Early attempts focused on proving theoretically the co-determinability of source time-dependent parameters and medium parameters from reflectivity data under simplifying assumptions: acoustic layered medium, quasi-impulsive and non-impulsive sources, primaries only data, inverting for only one medium parameter (reflectivity), (Ramm, 1985; Lewis, 1989; Bube et al., 1988; Minkoff and Symes, 1995). Later works have implemented and tested the feasibility of joint source-medium inversion in a variety of synthetic and field data testing the limits on the assumptions of recoverability theory and going beyond in some cases, e.g., Minkoff and Symes (1997), Wang et al. (2009), Zhou et al. (1997).

Despite some successful inversions, the joint determination of source and medium parameters under more realistic and general model assumptions can be difficult and in some cases impossible as demonstrated by Delprat-Jannaud and Lailly (2005). A 1-D isotropic acoustic medium is considered while inverting for an isotropic point-source and a "not so simple" impedance profile, assuming the background velocity is known. Errors due to incorrect source time-dependency (i.e., wrong phase, amplitude, and time shift) were shown to lead to accumulating errors in depth. Moreover, source-medium ambiguity is shown to be significant for both constant and varying velocity cases leading authors to conclude that codetermination is infeasible. Delprat-Jannaud and Lailly highlight a fundamental difficulty of joint inversion but also, from an optimistic point of view, motivate the study of such source-medium ambiguities in order

to overcome them. More importantly, their work emphasizes just how detrimental errors in the source can be, or conversely how important a "correct" source is to the seismic inversion problem.

Accurate estimation of seismic sources raises the more fundamental question of source representation. All of the works mentioned above, with the exception of Minkoff and Symes (1997), idealize the source contribution to that of an isotropic source localized at a single point in space (i.e., point-source). The point-source assumption for seismic sources is justified by the fact that the spatial source dimensions considered in exploration seismology are considerably smaller (typically by a magnitude) than the propagating wavelengths of seismic waves. The isotropy assumption, however, is questionable, especially when the source is known or potentially expected to exhibit directivity or anisotropy in its radiation pattern. A perfect example is the airgun array used in marine seismic surveying where the output pressure field of the source is known to exhibit vertical directivity. As a matter of example, Minkoff and Symes demonstrate the importance of accounting for anisotropy when modeling airgun array sources in marine reflection field data where both reflectivity and source parameters were estimated. Their results show that inverting for anisotropic source terms, as opposed to using a given modeled source or even inverting for an isotropic point-source, allows them to account for 25% more of the data and were able to achieve 90% data fit up to a gas-sand target. Moreover recovered reflectivity matched closely expected lithology, but only with an anisotropic source model.

Active work in anisotropic seismic source inversion primarily focuses on the determination of earthquake mechanisms, and as of in applications to microseismic events (small earthquakes) resulting from hydraulic fracturing. Sources are typically assumed to be point double-couples as to approximate the radiation pattern exhibited by a slipping fault. I refer to Aki and Richards (2002), Shearer (2009), Jost and Herrmann (1989), Julian et al. (1998) for a detailed discussion on this topic. Higher order multipole representations have also been considered in cases where finiteness of source (i.e., fault size) leads to anisotropy unaccounted in a double-couple model (Li et al., 2006; Stump and Johnson, 1982).

The work presented here concerns general seismic sources represented as a truncated series of multipole sources depending on anisotropy of the source. Given this choice of source representation results in a linear relationship between source parameters and seismic data, and hence joint source-medium parameter estimation via *full waveform inversion* (FWI) can be posed as a *separable* nonlinear least squares problem. The *variable projection* (VP) method (Golub and Pereyra, 1973) seeks to exploit the structure of separable nonlinear least squares problems by eliminating the linear parameters via an orthogonal projection resulting from a linear least squares problem. Algorithmically, VP is posed as a nested optimization scheme, where linear and nonlinear parameters are updated in the inner and outer optimization routines respectively. In practice, VP coupled with Gauss-Newton type algorithms for solving nonlinear least squares has been proven to outperform other multiparameter estima-

tion algorithms in some cases (Ruhe and Wedin, 1980). Rickett (2013) demonstrate the effectiveness of VP over simultaneous descent and alternating direction in the context of joint source-medium inversion via FWI. Future work regarding inversion of source-medium parameters will incorporate VP as a means to mitigate the difficulty of multiparameter inversion.

1.2 Contributions

This thesis focuses on laying the groundwork for joint source-medium parameter estimation with general sources via FWI, through three key contributions:

(i) a mathematical and computational framework for the modeling and inversion of general seismic sources via multipoles,

(ii) construction and analysis of discretizations of multipole sources on regular grids,

(iii) and preconditioners based on fractional time derivative/integral operators for the ill-conditioned multipole source estimation subproblem.

(i): In chapter 2, I formalize the representation of seismic sources as linear combinations of base multipoles, thus defining a natural finite dimensional vector space for source parameters referred to as the *MPS space*. Moreover, the multipole representation results in a source parametrization that is linear with respect to seismic data, which can be implemented as a *multichannel convolution* with appropriate kernels. Source representation is then coupled to generic finite difference solvers, assuming a

multipole discretization on regular grids as developed in chapter 3, to yield a flexible object-oriented framework that follows closely the structure of the underlying mathematics. I implement a particular instance of my multipole source framework in chapter 4 using the C++ packages IWave, a framework for finite difference solvers over regular grids, and Rice Vector Library (RVL), a library containing classes for expression of gradient-based optimization algorithms over Hilbert spaces.

(ii): Discretizations of multipole sources on regular grids for the application of finite difference solvers is at the heart of my framework and the forward modeling code. In chapter 3, I construct singular source approximations based on the discrete moment matching conditions as an extension of work by Waldén (1999) and Tornberg and Engquist (2004). Moreover, I show that these discrete approximations are related to a sequence of approximations in the continuum analog and prove their convergence in the weak-$*$ topology. Numerical tests in 2-D and 3-D acoustics demonstrate the accuracy of discretized multipole sources coupled with finite difference solvers of varying order. In particular, optimal convergence rates, as suggested by spatial approximation order of numerical schemes, are obtained away from the source location when using appropriate source approximation order.

(iii): Lastly, the source estimation subproblem is studied in chapter 5. The multipole source inversion subproblem poses challenges stemming from ill-conditioning of the source-to-data map. I develop an approach that seeks to better condition the problem from a fundamental angle: redefine the domain space of the source-to-data

map to yield a better-bounded operator, thus improving the condition number associated with solving the normal equations that result from a least squares formulation of the inversion problem. My preconditioners consist of fractional derivative/integral operators whose order is chosen semi-heuristically based on the analytical solutions of the acoustic wave equation in an unbounded media with a multipole source term. Numerical experiments demonstrate dramatic accelerations of conjugate gradient iterates and accuracy of estimated sources with preconditioning.

As an application of my multipole framework, I also study the efficacy of the multipole model on the airgun array source, the most common type of active source in marine seismic surveying. Synthetic data used for the numerical experiments was generated using open source airgun modeling software that takes into account the physics of airguns and airgun arrays, in particular, the nonlinear source-to-source interactions that occur in array setups. Inversion results recovered a dominating isotropic component of the multipole source model that accounted for 84% of the observed radiation pattern. An extra 10% of the observed output pressure field can be explained when incorporating dipole terms in the source representation, thus motivating the use of multipoles to capture source anisotropy.

Chapter 2

Multipole Source Representation

2.1 Introduction

Seismic sources are commonly idealized as concentrated at a source point, due to their small spatial extent relative to seismic wavelengths. A simple and familiar example of a wave propagation model with spatially concentrated source is the isotropic point radiator problem for the acoustic wave equation in Euclidean 3-space (Courant and Hilbert, 1962):

$$\begin{aligned} \frac{\partial^2}{\partial t^2} p(\mathbf{x},t) - c^2 \nabla^2 p(\mathbf{x},t) &= f_0(t)\delta(\mathbf{x}), \\ p(\mathbf{x},t) &= 0, \quad t << 0. \end{aligned} \tag{2.1}$$

The solution p is spherically symmetric:

$$p(\mathbf{x},t) = \frac{f_0\left(t - \frac{r}{c}\right)}{4\pi r}, \quad r = \sqrt{\mathbf{x}^T\mathbf{x}}. \tag{2.2}$$

Both active (man-made) and earthquake seismic sources, however, generate spatially asymmetric wave fields; see for example Shearer (2009) and Yilmaz (2001). The acoustic isotropic point radiator is, therefore, inadequate as a model of seismic wave

generation and propagation because of its prediction of spatial symmetry, on top of other inadequacies in its representation of wave physics. The symmetry of the solution arises in part from the spherical symmetry of the right-hand side in equation 2.1. Therefore accurate modeling of seismic wave fields must include energy source (right-hand side) representations generating anisotropic radiation patterns.

A *multipole*, or *multipole source* in the context of source modeling, is a finite linear combination of partial derivatives of a spatial delta function. Such sources combine localization of energy and anisotropic radiation pattern. In fact, Peetre's Theorem (theorem 1.5.3 in Hörmander (1969)) implies that any function (in reality a distribution) of space and time $f(\mathbf{x}, t)$ concentrated entirely at a point in space (of *point support*) is a multipole of finite order $N \geq 0$, namely

$$f(\mathbf{x}, t) = \sum_{|\mathbf{s}|=0}^{N} f_{\mathbf{s}}(t)\ D^{\mathbf{s}}\delta(\mathbf{x} - \mathbf{x}^*), \tag{2.3}$$

in which I have used standard *multi-index notation*: for spatial dimension d and multi-index (integer d-tuple) $\mathbf{s} = (s_1, ..., s_d)$, the $\mathbf{s}$-mixed partial derivative operator $D^{\mathbf{s}}$ and its (total) order $|\mathbf{s}|$ are

$$D^{\mathbf{s}} = \prod_{i=1}^{d} \left(\frac{\partial}{\partial x_i} \right)^{s_i}, \quad |\mathbf{s}| = \sum_{i=1}^{d} s_i.$$

The coefficient time functions $f_{\mathbf{s}}(t)$ may be scalar-, vector-, or tensor-valued, according to the nature of quantity being updated (pressure, velocity, or stress) in the

equation in which $f(\mathbf{x}, t)$ appears as right-hand side. Multipoles may approximate arbitrary sources highly localized on the wavelength scale, in the sense of generating approximately the same field away from the source location, and for this reason, have enjoyed widespread use in modeling seismic sources (Shearer, 2009).

This chapter describes a multipole source representation with a natural parametrization, namely, the coefficient time functions $\{f_{\mathbf{s}}\}$, subsequently defining a vector space of multipoles.

2.2 Multipole Representation: Multipole Spaces

The localized sources modeled in this work occur as right-hand sides in the first order forms of time domain linear acoustics and elasticity:

(velocity-pressure form of acoustic equations)

$$\begin{aligned} \frac{\partial}{\partial t} p(\mathbf{x}, t) + \kappa(\mathbf{x}) \frac{\partial}{\partial x_j} v_j(\mathbf{x}, t) &= f(\mathbf{x}, t), \\ \frac{\partial}{\partial t} v_i(\mathbf{x}, t) + \beta(\mathbf{x}) \frac{\partial}{\partial x_i} p(\mathbf{x}, t) &= f_i(\mathbf{x}, t), \end{aligned} \tag{2.4}$$

(velocity-stress form of linear elasticity equations)

$$\begin{aligned} \frac{\partial}{\partial t} v_i(\mathbf{x}, t) - \beta(\mathbf{x}) \frac{\partial}{\partial x_j} \sigma_{ij}(\mathbf{x}, t) &= f_i(\mathbf{x}, t), \\ \frac{\partial}{\partial t} \sigma_{ij}(\mathbf{x}, t) - c_{ijmn}(\mathbf{x}) \frac{\partial}{\partial x_n} v_m(\mathbf{x}, t) &= f_{ij}(\mathbf{x}, t), \end{aligned} \tag{2.5}$$

for $\mathbf{x} \in \Omega \subset \mathbb{R}^d$ and $t \in (0, T]$ with homogeneous (free-surface) boundary and initial conditions, where

- β = buoyancy (reciprocal of density),
- κ = bulk modulus,
- $c_{ijmn} = ijmn$-component of fourth-order Hooke's tensor,
- p = pressure field,
- $v_i = i$-component of particle-velocity vector,
- $\sigma_{ij} = ij$-component of second-order stress tensor,
- f = scalar pressure source = defect in acoustic constitutive law,
- $f_i = i$-component of velocity source vector $\mathbf{f}$= body force,
- $f_{ij} = ij$-component of second-order tensor stress source $\mathbf{F}$= defect in elastic constitutive law.

Indices i, j, m, n run from $1, ..., d$, where d is the space dimension. Einstein summation convention is assumed, that is, repeated indices are summed. Scalar, vector, and second-order tensor right-hand sides occur in these equations, representing energy sources of several types. There is some redundancy amongst these possibilities, for example, a spatially localized constitutive law defect (pressure or stress source) may be exchanged for an equivalent body force that generates the same acoustic or elastic field away from the source location. Because of these trade-off possibilities, I will tacitly assume that only one of the three types of source terms - scalar, vector, or tensor - is present.

The scalar multipole of order N centered at $\mathbf{x}^* \in \mathbb{R}^d$ has already been introduced in equation 2.3. Expressions for vector and tensor multipoles of order N are similar:

$$f_i(\mathbf{x}, t) = \sum_{|\mathbf{s}| \leq N} f_{i;\mathbf{s}}(t)\ D^{\mathbf{s}}\delta(\mathbf{x} - \mathbf{x}^*),$$

$$f_{ij}(\mathbf{x}, t) = \sum_{|\mathbf{s}| \leq N} f_{ij;\mathbf{s}}(t)\ D^{\mathbf{s}}\delta(\mathbf{x} - \mathbf{x}^*).$$

Evidently multipoles of each type and order form vector spaces. Subspaces of these spaces are determined by linear constraints (for example, tensor symmetry). To describe vector spaces of multipoles conveniently, I introduce *multipole bases* $\{b_i\}$, $\{\mathbf{b}_i\}$, and $\{\mathbf{B}_i\}$. These are simply linearly independent sets of multipoles, whose linear combinations with scalar time function coefficients $\{w_i\}$, called the *multipole coefficients*, span various vector spaces of multipoles:

$$\begin{aligned} f(\mathbf{x}, t) &= \sum_i w_i(t) b_i(\mathbf{x}), \\ \mathbf{f}(\mathbf{x}, t) &= \sum_i w_i(t) \mathbf{b}_i(\mathbf{x}), \\ \mathbf{F}(\mathbf{x}, t) &= \sum_i w_i(t) \mathbf{B}_i(\mathbf{x}), \end{aligned} \tag{2.6}$$

Each basis element combines scalar, vector, or tensor coefficients $c_{ij}, \mathbf{c}_{ij}$ or $\mathbf{C}_{ij}$, and mixed partial derivatives of the spatial delta function, parametrized by multi-indices $\mathbf{s}_{ij}$:

$$
\begin{aligned}
b_i(\mathbf{x}) &= \sum_j c_{ij} D^{\mathbf{s}_{ij}} \delta(\mathbf{x} - \mathbf{x}^*), \\
\mathbf{b}_i(\mathbf{x}) &= \sum_j \mathbf{c}_{ij} D^{\mathbf{s}_{ij}} \delta(\mathbf{x} - \mathbf{x}^*), \\
\mathbf{B}_i(\mathbf{x}) &= \sum_j \mathbf{C}_{ij} D^{\mathbf{s}_{ij}} \delta(\mathbf{x} - \mathbf{x}^*).
\end{aligned}
\tag{2.7}
$$

Many choices of combinations $c_{ij}, \mathbf{s}_{ij}$ (and so on) are possible - I show some of these possible choices below. I will assume in practice that such a choice has been made.

As a first example, the scalar multipole basis of order zero centered at $\mathbf{x}^*$ consists of one element, b_1, given by

$$b_1(\mathbf{x}) = \delta(\mathbf{x} - \mathbf{x}^*).$$

A maximal choice of scalar multipole basis of order one (in 3-D) centered at $\mathbf{x}^*$ is

$$
\begin{aligned}
&b_1(\mathbf{x}) = \delta(\mathbf{x} - \mathbf{x}^*), \\
&b_2(\mathbf{x}) = \frac{\partial}{\partial x_1}\delta(\mathbf{x} - \mathbf{x}^*), \quad b_3(\mathbf{x}) = \frac{\partial}{\partial x_2}\delta(\mathbf{x} - \mathbf{x}^*), \quad b_4(\mathbf{x}) = \frac{\partial}{\partial x_3}\delta(\mathbf{x} - \mathbf{x}^*).
\end{aligned}
\tag{2.8}
$$

A maximal vector multipole basis of order zero (in 3-D) centered at $\mathbf{x}^*$ is

$$
\mathbf{b}_1(\mathbf{x}) = \delta(\mathbf{x} - \mathbf{x}^*) \begin{bmatrix} 1 \\ 0 \\ 0 \end{bmatrix}, \quad \mathbf{b}_2(\mathbf{x}) = \delta(\mathbf{x} - \mathbf{x}^*) \begin{bmatrix} 0 \\ 1 \\ 0 \end{bmatrix}, \quad \mathbf{b}_3(\mathbf{x}) = \delta(\mathbf{x} - \mathbf{x}^*) \begin{bmatrix} 0 \\ 0 \\ 1 \end{bmatrix}.
$$

A maximal tensor multipole basis of order zero (in 3-D) centered at $\mathbf{x}^*$ is

$$\mathbf{B}_1(\mathbf{x}) = \delta(\mathbf{x}-\mathbf{x}^*)\begin{bmatrix} 1,0,0 \\ 0,0,0 \\ 0,0,0 \end{bmatrix}, \quad \mathbf{B}_2(\mathbf{x}) = \delta(\mathbf{x}-\mathbf{x}^*)\begin{bmatrix} 0,1,0 \\ 0,0,0 \\ 0,0,0 \end{bmatrix}, \quad \mathbf{B}_3(\mathbf{x}) = \delta(\mathbf{x}-\mathbf{x}^*)\begin{bmatrix} 0,0,1 \\ 0,0,0 \\ 0,0,0 \end{bmatrix},$$

$$\mathbf{B}_4(\mathbf{x}) = \delta(\mathbf{x}-\mathbf{x}^*)\begin{bmatrix} 0,0,0 \\ 1,0,0 \\ 0,0,0 \end{bmatrix}, \quad \mathbf{B}_5(\mathbf{x}) = \delta(\mathbf{x}-\mathbf{x}^*)\begin{bmatrix} 0,0,0 \\ 0,1,0 \\ 0,0,0 \end{bmatrix}, \quad \mathbf{B}_6(\mathbf{x}) = \delta(\mathbf{x}-\mathbf{x}^*)\begin{bmatrix} 0,0,0 \\ 0,0,1 \\ 0,0,0 \end{bmatrix},$$

$$\mathbf{B}_7(\mathbf{x}) = \delta(\mathbf{x}-\mathbf{x}^*)\begin{bmatrix} 0,0,0 \\ 0,0,0 \\ 1,0,0 \end{bmatrix}, \quad \mathbf{B}_8(\mathbf{x}) = \delta(\mathbf{x}-\mathbf{x}^*)\begin{bmatrix} 0,0,0 \\ 0,0,0 \\ 0,1,0 \end{bmatrix}, \quad \mathbf{B}_9(\mathbf{x}) = \delta(\mathbf{x}-\mathbf{x}^*)\begin{bmatrix} 0,0,0 \\ 0,0,0 \\ 0,0,1 \end{bmatrix}.$$

Some applications may require constraints on the source representation for physical reasons or assumptions on the radiation field of the source. For example, in the study of earthquake source mechanisms, sources are commonly represented by the *seismic moment tensor* which in the terminology introduced here is precisely a tensor multipole of order $N = 0$; I make this relation definite in appendix A. Earthquake sources must preserve angular momentum so the moment tensor source must be symmetric: $f_{ij} = f_{ji}$, for $i, j = 1, 2, 3$. This symmetry constraint suggests another tensor

multipole basis of order zero,

$$\mathbf{B}_1(\mathbf{x}) = \delta(\mathbf{x}-\mathbf{x}^*)\begin{bmatrix} 1,0,0 \\ 0,0,0 \\ 0,0,0 \end{bmatrix}, \quad \mathbf{B}_2(\mathbf{x}) = \delta(\mathbf{x}-\mathbf{x}^*)\begin{bmatrix} 0,0,0 \\ 0,1,0 \\ 0,0,0 \end{bmatrix}, \quad \mathbf{B}_3(\mathbf{x}) = \delta(\mathbf{x}-\mathbf{x}^*)\begin{bmatrix} 0,0,0 \\ 0,0,0 \\ 0,0,1 \end{bmatrix},$$

$$\mathbf{B}_4(\mathbf{x}) = \delta(\mathbf{x}-\mathbf{x}^*)\begin{bmatrix} 0,1,0 \\ 1,0,0 \\ 0,0,0 \end{bmatrix}, \quad \mathbf{B}_5(\mathbf{x}) = \delta(\mathbf{x}-\mathbf{x}^*)\begin{bmatrix} 0,0,1 \\ 0,0,0 \\ 1,0,0 \end{bmatrix}, \quad \mathbf{B}_6(\mathbf{x}) = \delta(\mathbf{x}-\mathbf{x}^*)\begin{bmatrix} 0,0,0 \\ 0,0,1 \\ 0,1,0 \end{bmatrix}.$$

Multipole expansions 2.6 are determined by

- the source location $\mathbf{x}^*$
- the choices of multipole basis functions $b_i(\mathbf{x})$ (for the scalar case, similar for vector and tensor cases),
- and the coefficient time functions $w_i(t)$.

I collect the time-dependent coefficients and refer to them as the *multipole source (MPS) coefficient vectors* $w = \{w_i(t) : i = 1, 2, ...\}$, and endow them with the obvious definition of linear combination: for MPS coefficient vectors $w^{(1)}$ and $w^{(2)}$ and scalars a_1, a_2,

$$a_1 w^{(1)} + a_2 w^{(2)} = \{a_1 w_i^{(1)}(t) + a_2 w_i^{(2)}(t)\}. \tag{2.9}$$

With definition 2.9, the set of MPS coefficient vectors becomes a vector space, an

MPS space. I regard the other two identifying items listed above (source location, choice of multipole basis) as attributes of an MPS space as well.

Remark: While not important for current purposes, it should be mentioned that norms and inner ("dot") products can also be implemented for MPS spaces. For example, the obvious (Euclidean or L^2) inner product is

$$\langle w^{(1)}, w^{(2)} \rangle = \sum_i \int dt \, w_i^{(1)}(t) \; w_i^{(2)}(t). \tag{2.10}$$

However many other inner products are possible. As I shall show in chapter 5, a better choice of inner product than that given in equation 2.10 is possible, in that it improves the condition number of the linear map from MPS coefficients to data traces, hence accelerates the convergence of iterative inversion algorithms.

Given a choice of MPS space $\mathfrak{W}$, equation 2.6 defines a linear mapping L from $\mathfrak{W}$ to distributions in physical space: in the scalar case,

$$(Lw)(\mathbf{x}, t) = \sum_i w_i(t) b_i(\mathbf{x}), \tag{2.11}$$

I call L the *MPS-to-RHS* map, since Lw may be used as a right-hand side source, that is as f or $\mathbf{f}$ in the system 2.4, $\mathbf{f}$ or $\mathbf{F}$ in the system 2.5.

Summary

The MPS space presents a natural way of representing multipole sources by time-dependent coefficients, assuming that source information (primarily source location, choice of MPS basis) is encoded in the space. In other words, given an MPS space, a multipole is uniquely determined by its MPS coefficient vector. Moreover, the mapping from MPS coefficients -to- multipoles (referred to the MPS-to-RHS map) is linear, which will play a key role in coupling multipole representations 2.6 to forward modeling and ultimately inversion. Concerning forward modeling, it should be noted that a multipole representation poses some interesting mathematical and computational difficulties. Mainly, how does one go about solving acoustic or elasticity systems 2.4 and 2.5 with singular sources (i.e., multipoles) via finite difference on regular grids? This is the subject matter for the next chapter.

Chapter 3

Singular Source Approximation

3.1 Introduction

While finite element methods are also used in earthquake seismic modeling and inversion (Komatisch et al., 2000; Cohen, 2002; Epanomeritakis et al., 2009), in this thesis I focus on regular (rectangular) grid finite difference methods, which are widely used for basin- and exploration-scale modeling; see Moczo et al. (2006) for an excellent overview and many older references. Such methods pose an immediate problem for singular source models such as multipoles: finite difference algorithms "know" only gridded fields, so a source located at an arbitrary point $\mathbf{x}^*$ in space must be represented somehow by virtual sources at nearby grid points. This task is complicated by the nature of the field: as is evident for instance from inspection of the 3-D analytical function 2.2, solutions of the wave equations 2.4, 2.5 with singular right-hand sides are generally themselves singular at the source point, so the Taylor-series based analysis of finite difference accuracy does not apply. Imitating finite-element singular source representation, for example by using adjoint interpolation, may reduce the accuracy of the modeled field, in the sense of convergence order: visually, large errors can pollute the field near the source, and propagate throughout the simulation domain.

Waldén (1999) developed approximations to singular source terms (derivatives of the delta function) in a finite difference and finite element setting for the 1-D Helmholtz equation for which his analysis and numerical examples demonstrated point-wise convergence of numerical solutions with optimal convergence rates away from the source. Tornberg and Engquist (2004) refined these ideas for the delta function in higher dimensions and provided further error analysis, primarily for finite difference solutions to simple ODEs, and parabolic and elliptic PDEs. Recently, Hosseini et al. (2016) presented a unified theory for the approximation, or regularizations, of the delta function independent of numerical scheme and their application to prototypical elliptic and hyperbolic PDEs.

The goal of this chapter is to develop a systematic approach for generating gridded functions over regular grids that approximate, in some sense, multipoles as the grid is refined. This is accomplished in the second section through the *discrete moment conditions* as an extension of Waldén (1999) and Tornberg and Engquist (2004) for general derivatives of the delta function in dimensions higher than one. I also show that the discrete moment conditions, in fact, define a sequence of continuum functions that converge to target distributions in a weak sense, a new result. As a precursor to the discrete case, I first discuss the approximation theory for the continuum case, introducing the *(continuous) moment conditions* based on work by Hosseini et al. (2016).

3.2 (Continuous) Moment Conditions

I begin by noting that the delta function and its derivatives (and thus multipoles) are not actually functions but rather so-called distributions which are operators that return a value when applied to a test function. Let $\mathcal{D}$ denote the *space of test functions* over $\mathbb{R}^d$, that is the space of $C_0^\infty(\mathbb{R}^d)$ endowed with the standard topology of test functions. The set of *distributions* is given by the dual of the space of test functions, denoted by $\mathcal{D}'$. It is conventional to represent the application of a distribution on a function by the integral of the product, even when the distribution is not actually a function that can be integrated in the usual sense. I introduce, however, the following notation to emphasize that the delta function and its derivatives are distributions. Given multi-index $\mathbf{s} = (s_1, ..., s_d)$, the $\mathbf{s}$-mixed partial derivative of the delta function shifted by $\mathbf{x}^* \in \mathbb{R}^d$, denoted by $D^{\mathbf{s}}\delta(\cdot; \mathbf{x}^*) \in \mathcal{D}'$, as a distribution is defined by

$$D^{\mathbf{s}}\delta(\psi; \mathbf{x}^*) = (-1)^{|\mathbf{s}|} D^{\mathbf{s}}\psi(\mathbf{x}^*), \quad \forall \psi \in \mathcal{D}.$$

The distribution $D^{\mathbf{s}}\delta(\cdot; \mathbf{0})$ is simply denoted by $D^{\mathbf{s}}\delta$.

The key idea for constructing approximations to $D^{\mathbf{s}}\delta(\cdot, \mathbf{x}^*)$ is based on mimicking the behavior of the target distribution on polynomials, reminiscent of finite difference approximations for differential operators. Consider $\psi(\mathbf{x}) = (\mathbf{x} - \mathbf{x}^*)^\alpha$, with multi-index $\alpha = (\alpha_1, ..., \alpha_d)$, where multi-indexed monomials are interpreted as the product

of monomials in each dimension,

$$(\mathbf{x}-\mathbf{x}^*)^\alpha = \prod_{k=1}^{d}(x_k - x_k^*)^{\alpha_k}.$$

It can be shown that

$$D^{\mathbf{s}}\delta(\psi;\mathbf{x}^*) = \mathbf{s}!(-1)^{|\mathbf{s}|}\delta_{\mathbf{s}\alpha}$$

where $\delta_{\mathbf{s}\alpha}$ is the Kronecker delta, defined as follows for multi-indexes,

$$\delta_{\mathbf{s}\alpha} := \prod_{k=1}^{d}\delta_{s_k\alpha_k}.$$

Given $\eta \in L_0^1(\mathbb{R}^d)$ (i.e., absolutely integrable and of compact support) and multi-index α, the *α-moment* of η centered at $\mathbf{x}^* \in \mathbb{R}^d$, denoted by $M_\alpha(\cdot;\mathbf{x}^*)$, is defined as

$$M_\alpha(\eta,\mathbf{x}^*) := \int_{\mathbb{R}^d} d\mathbf{x}\ \eta(\mathbf{x}-\mathbf{x}^*)(\mathbf{x}-\mathbf{x}^*)^\alpha. \tag{3.1}$$

Note that integration in equation 3.1 is translation invariant hence $M_\alpha(\eta,\mathbf{x}^*)$ is constant with respect to $\mathbf{x}^*$, which I denote by $M_\alpha(\eta)$. For given $q \in \mathbb{N}$ and multi-index $\mathbf{s}$, the function η is said to satisfy the *$(q,\mathbf{s})$-moment conditions* if

$$M_\alpha(\eta) = \mathbf{s}!(-1)^{|\mathbf{s}|}\delta_{\mathbf{s}\alpha}, \quad \forall|\alpha| = 0,...,q+|\mathbf{s}|-1. \tag{3.2}$$

If η satisfies the $(q,\mathbf{s})$-moment conditions, then its induced distribution $\tilde{\eta} \in \mathcal{D}'$

given by

$$\tilde{\eta}(\psi) = \int_{\mathbb{R}^d} d\mathbf{x}\, \eta(\mathbf{x})\psi(\mathbf{x}), \quad \forall \psi \in \mathcal{D},$$

is an approximation to $D^{\mathbf{s}}\delta$ in that it is exact on polynomials of order $q + |\mathbf{s}| - 1$. The following theorem states that a sequence of (regular) distributions of compact support, satisfying the $(q, \mathbf{s})$-moment conditions, will converge in the weak-$*$ topology at a rate q to the target distribution as the width of the supports approach zero.

Theorem 3.1. *Let $q \in \mathbb{N}$ and multi-index $\mathbf{s}$ be given. Suppose $\{\eta_H\} \subset L_0^1(\mathbb{R}^d)$ is a sequence of functions as $H \to 0$, where $supp(\eta_H) \subset B(\mathbf{0}, H)$; $B(\mathbf{0}, H)$ is the ball of radius H in $\mathbb{R}^d$ centered at the origin. Furthermore, suppose that there exists a constant $K > 0$ independent of H such that*

$$\int_{\mathbb{R}^d} d\mathbf{x}\, |\eta_H(\mathbf{x})|\, |\mathbf{x}^\alpha| \leq K, \quad \forall |\alpha| = |\mathbf{s}|. \tag{3.3}$$

If $\{\eta_H\}$ satisfy the $(q, \mathbf{s})$-moment conditions, equation 3.2, then the sequence of distributions $\{\tilde{\eta}_H\}$, defined by

$$\tilde{\eta}_H(\psi) := \int_{\mathbb{R}^d} d\mathbf{x}\, \eta_H(\mathbf{x})\psi(\mathbf{x}), \quad \forall \psi \in \mathcal{D},$$

converges to $D^{\mathbf{s}}\delta$ in the weak-$*$ topology as $H \to 0$. In particular, if ψ is of class $C^{q+|\mathbf{s}|}$ over $B(\mathbf{0}, H)$, then

$$|D^{\mathbf{s}}\delta(\psi) - \tilde{\eta}_H(\psi)| = O(H^q).$$

Remark: Theorem 3.1 can be replicated for the shifted delta function and its derivatives by simply shifting the sequence $\tilde{\eta}_H$ accordingly, i.e., define the shifted distribution $\tilde{\eta}_H(\cdot;\mathbf{x}^*)$ by

$$\tilde{\eta}_H(\psi;\mathbf{x}^*) := \int_{\mathbb{R}^d} d\mathbf{x}\ \eta_H(\mathbf{x}-\mathbf{x}^*)\psi(\mathbf{x}).$$

Proof. I start by applying multi-variate Taylor's theorem (Evans, 1997), replacing $\psi(\mathbf{x})$ in equation 3.1 by its Taylor series centered at the origin and truncated after $N = q + |\mathbf{s}| - 1$ terms;

$$\begin{aligned}\tilde{\eta}_H(\psi) &= \int_{B(\mathbf{0},H)} d\mathbf{x}\ \eta_H(\mathbf{x}) \left(\sum_{|\alpha|=0}^{N} \frac{D^\alpha\psi(\mathbf{0})}{\alpha!}\ \mathbf{x}^\alpha + \sum_{|\beta|=N+1} R_\beta(\mathbf{x})\mathbf{x}^\beta \right) \\ &= \sum_{|\alpha|=0}^{N} \frac{D^\alpha\psi(\mathbf{0})}{\alpha!} \left(\int_{B(\mathbf{0},H)} d\mathbf{x}\ \eta_H(\mathbf{x})\mathbf{x}^\alpha \right) + \sum_{|\beta|=N+1} \int_{B(\mathbf{0},H)} d\mathbf{x}\ \eta_H(\mathbf{x})R_\beta(\mathbf{x})\mathbf{x}^\beta,\end{aligned}$$

where R_β is the remainder term,

$$R_\beta(\mathbf{x}) = \frac{|\beta|}{\beta!} \int_0^1 dt\ (1-t)^{|\beta|-1} D^\beta\psi(t\mathbf{x}).$$

Note that the term in the parenthesis in the bottom equation corresponds to the α-moment with $|\alpha| \leq q + |\mathbf{s}| - 1$, hence the $(q,\mathbf{s})$-moment conditions apply;

$$\begin{aligned}\tilde{\eta}_H(\psi) &= \sum_{|\alpha|=0}^{N} \frac{1}{\alpha!} D^\alpha\psi(\mathbf{0}) \Big(\mathbf{s}!(-1)^{|\mathbf{s}|}\delta_{\mathbf{s}\alpha} \Big) + \sum_{|\beta|=N+1} \int_{B(\mathbf{0},H)} d\mathbf{x}\ \eta_H(\mathbf{x})R_\beta(\mathbf{x})\mathbf{x}^\beta \\ &= (-1)^{|\mathbf{s}|} D^{\mathbf{s}}\psi(\mathbf{0}) + \sum_{|\beta|=N+1} \int_{B(\mathbf{0},H)} d\mathbf{x}\ \eta_H(\mathbf{x})R_\beta(\mathbf{x})\mathbf{x}^\beta.\end{aligned}$$

The remainder term is bounded uniformly over $B(\mathbf{0}, H)$,

$$\sup_{\mathbf{x}\in B(\mathbf{0},H)} |R_\beta(\mathbf{x})| \leq C(\beta,\psi) := \frac{1}{\beta!} \max_{|\alpha|=|\beta|} \max_{\mathbf{y}\in B(\mathbf{0},H)} |D^\alpha \psi(\mathbf{y})|,$$

using the fact that $\psi \in C^{N+1}(B(\mathbf{0}, H))$. This gives the following error estimate,

$$|D^{\mathbf{s}}\delta(\psi) - \tilde{\eta}_H(\psi)| \leq \sum_{|\beta|=N+1} C(\beta,\psi) \int_{B(\mathbf{0},H)} d\mathbf{x}\, |\eta_H(\mathbf{x})|\, |\mathbf{x}^\beta|.$$

Let γ be a multi-index such that $|\gamma| = q$, thus $|\beta - \gamma| = |\mathbf{s}|$. This yields,

$$\begin{aligned}
|D^{\mathbf{s}}\delta(\psi) - \tilde{\eta}_H(\psi)| &\leq \sum_{|\beta|=N+1} C(\beta,\psi) \left(\sup_{\mathbf{x}\in B(\mathbf{0},H)} |\mathbf{x}^\gamma| \right) \int_{B(\mathbf{0},H)} d\mathbf{x}\, |\eta_H(\mathbf{x})|\, |\mathbf{x}^{\beta-\gamma}| \\
&\leq \sum_{|\beta|=N+1} C(\beta,\psi) \left(\sup_{\mathbf{x}\in B(\mathbf{0},H)} |\mathbf{x}^\gamma| \right) K \\
&= O(H^q)
\end{aligned}$$

□

The moment conditions given in equation 3.2 and theorem 3.1 are extensions of what is presented in Hosseini et al. (2016) for $|\mathbf{s}| \neq 0$. Given the theorem above, I refer to q as the *singular source approximation order*, and η_H as being a q-order, or $O(H^q)$, approximation of $D^{\mathbf{s}}\delta$.

3.3 Discrete Moment Conditions

For convenience, I define the regular grid centered at $\mathbf{x}_0 \in \mathbb{R}^d$ with cell size $\mathbf{h} \in \mathbb{R}^d$, $\mathbf{h} > \mathbf{0}$, as the collection of points denoted by $\mathcal{G}(\mathbf{x}_0, \mathbf{h})$,

$$\mathcal{G}(\mathbf{x}_0, \mathbf{h}) := \{\mathbf{x}_\mathbf{n} = (x_{1,n_1}, ..., x_{d,n_d}) = (x_{0,1} + n_1 h_1, ..., x_{0,d} + n_d h_d),\ \mathbf{n} \in \mathbb{Z}^d\}.$$

The dependence of real-valued grid functions with respect to a given regular grid $\mathcal{G}(\mathbf{x}_0, \mathbf{h})$, say $\eta^h : \mathcal{G}(\mathbf{x}_0, \mathbf{h}) \to \mathbb{R}$, is made implicit through the use of multi-indexing notation. For example, given $\mathbf{x}_\mathbf{n} \in \mathcal{G}(\mathbf{x}_0, \mathbf{h})$ for some multi-index $\mathbf{n} = (n_1, ..., n_d)$,

$$\eta^h_\mathbf{n} = \eta^h(\mathbf{x}_\mathbf{n}).$$

Note that there is no reason to assume that the grid cell is cubical: it may have different lengths along different axes. However, I assume that the grid is refined by scaling a characteristic grid cell size h (e.g., $h = \max_k h_k$) and continue to denote grid functions and other grid-dependent quantities with superscript h even in dimensions higher than one.

The obvious definition of the *discrete α-moment*, centered at $\mathbf{x}^* \in \mathbb{R}^d$, of a grid function $\eta^h : \mathcal{G}(\mathbf{x}_0, \mathbf{h}) \to \mathbb{R}$ is given as follows:

$$M^h_\alpha(\eta^h, \mathbf{x}^*) := \left(\prod_{k=1}^{d} h_k\right) \sum_\mathbf{n} \eta^h_\mathbf{n}\, (\mathbf{x}_\mathbf{n} - \mathbf{x}^*)^\alpha.$$

It is worth pointing out that, unlike the continuum case, the discrete moment defined above is dependent on choice of grid, and subsequently dependent on $\mathbf{x}^*$. Similar to the continuous moment conditions 3.2, grid function η^h is said to satisfy the *discrete* $(q, \mathbf{s})$*-moment conditions* at $\mathbf{x}^* \in \mathbb{R}^d$ if

$$M_\alpha^h(\eta^h, \mathbf{x}^*) = \mathbf{s}!(-1)^{|\mathbf{s}|}\delta_{\mathbf{s}\alpha}, \quad \forall |\alpha| = 0, ..., q + |\mathbf{s}| - 1. \tag{3.4}$$

The following theorem is a discrete analogue of theorem 3.1.

Theorem 3.2. *Let $q \in \mathbb{N}$, multi-index $\mathbf{s}$, and $\mathbf{x}^* \in \mathbb{R}^d$ be given. Suppose $\{\eta^h\}$ is a sequence of grid functions $\eta^h : \mathcal{G}(\mathbf{x}_0, \mathbf{h}) \to \mathbb{R}$ as $h \to 0$. Furthermore, assume that the support of η^h is contained in $B(\mathbf{x}^*, H)$ with $H = O(h)$, and that there exists constant $K > 0$ independent of H such that*

$$\left(\prod_{k=1}^{d} h_k\right) \sum_{\mathbf{n}} |\eta_{\mathbf{n}}^h| \, |(\mathbf{x}_{\mathbf{n}} - \mathbf{x}^*)^\alpha| \leq K, \quad \forall |\alpha| = |\mathbf{s}|.$$

If $\{\eta^h\}$ satisfy the discrete $(q, \mathbf{s})$-moment conditions at $\mathbf{x}^*$ (equation 3.4) and ψ is of class $C^{q+|\mathbf{s}|}$ over $B(\mathbf{x}^*, H)$, then

$$\left| D^{\mathbf{s}}\delta(\psi; \mathbf{x}^*) - \left(\prod_{k=1}^{d} h_k\right) \sum_{\mathbf{n}} \eta_{\mathbf{n}}^h \, \psi(\mathbf{x}_{\mathbf{n}}) \right| = O(h^q).$$

Proof. The proof of this theorem is omitted since it is nearly identical to that of the continuum case (theorem 3.1), replacing integrals with summations over multi-

indexes. The jump from $O(H^q)$ to $O(h^q)$ follows from $H = O(h)$. □

Theorem 3.2 and discrete moment conditions 3.4 are generalizations of work by Tornberg and Engquist (2004) for $|\mathbf{s}| \neq 0$. Moment conditions are also an extension of Waldén (1999) for dimensions higher than one. I now discuss with more detail how to construct said sequences of gridded functions as the tensor product of 1-D grid functions that satisfy appropriate discrete moment conditions as suggested by Tornberg and Engquist (2004).

3.3.1 Tensor Product Construction

Multivariate gridded functions $\eta^h : \mathcal{G}(\mathbf{x}_0, \mathbf{h}) \to \mathbb{R}$ will be generated by taking tensor products of one dimensional grid functions $\eta^{h_k} : \mathcal{G}(x_{0,k}, h_k) \to \mathbb{R}$, that is

$$\eta^h(\mathbf{x}_\mathbf{n}) = \prod_{k=1}^{d} \eta^{h_k}(x_{k,n_k}),$$

or in index notation,

$$\eta^h_\mathbf{n} = \prod_{k=1}^{d} \eta^{h_k}_{n_k}.$$

Thus it suffices to focus on the construction of gridded approximations in 1-D. For convenience, the k subindex is dropped and all gridded quantities are assumed to be one-dimensional.

Gridded approximations are assumed to be zero outside interval $[-R + a^*, R + a^*)$ with $2R = Nh$, for some positive integer N and $a^* \in \mathbb{R}$ such that x^* is in the interior of

the interval. Such supports allow for the possibility of centered (case where $x^* = a^*$) or skewed ($x^* \neq a^*$) gridded functions relative to center point x^*. For gridded functions of said support it follows that there exists a subset of N grid points, denoted by $\{\tilde{x}_\ell\}_{\ell=1}^N \subset \mathcal{G}(x_0, h)$, such that they are contained in the interval $[-R + a^*, R + a^*)$. These grid points $\{\tilde{x}_\ell\}_{\ell=1}^N$ are referred to as the *stencil points* of the approximation. I will assume that these stencil points are ordered, i.e., $\tilde{x}_1 < \tilde{x}_2 < \cdots < \tilde{x}_N$. The discrete (q, s)-moment conditions thus result in a $N \times (q + s)$ system of equations for the grid function η^h evaluated at stencil points,

$$\mathbf{Ad} = \mathbf{b}$$

with

$$\{\mathbf{A}\}_{k\ell} = (\tilde{x}_\ell - x^*)^{k-1}, \quad \{\mathbf{d}\}_\ell = \eta^h(\tilde{x}_\ell), \quad \{\mathbf{b}\}_k = \frac{s!(-1)^s}{h}\delta_{s,k-1},$$

for $\ell = 1, ..., N$ and $k = 1, ..., q + s$. Note that $\mathbf{A}$ is a Vandermonde matrix of full rank and is guaranteed a solution if $N \geq q + s$ (unique if $N = q + s$) and no solution for $N < q + s$ under general $x^* \in \mathbb{R}$. It will be of benefit to pick grid functions of minimal support, that is $N = q + s$; this will be more apparent when coupling source approximations with finite difference schemes (chapter 4).

Taking $N = q + s$, the system above will result in a unique solution for a given $x^* \in \mathbb{R}$. In fact the inverse matrix for $\mathbf{A}$ can be written explicitly using the following

Vandermonde matrix inverse formula,

$$\{\mathbf{A}^{-1}\}_{\ell k} = \begin{cases} (-1)^{N-k} \dfrac{\displaystyle\sum_{\mathbf{m}\in\mathcal{I}(N,k,\ell)} (\tilde{x}_{m_1} - x^*)\cdots(\tilde{x}_{m_{N-k}} - x^*)}{\displaystyle\prod_{\substack{1\le m\le N \\ m\neq\ell}} (\tilde{x}_\ell - \tilde{x}_m)}, & \text{for } 1 \le k \le N \\ \dfrac{1}{\displaystyle\prod_{\substack{1\le m\le N \\ m\neq\ell}} (\tilde{x}_\ell - \tilde{x}_m)}, & \text{for } k = N \end{cases}$$

where I have introduced the multi-index set $\mathcal{I}(N,k,\ell)$ to alleviate the expression above,

$$\mathcal{I}(N,k,\ell) := \{(m_1,...,m_{N-k}) : 1 \le m_1 < ... < m_{N-k} \le N \text{ and } m_1,\cdots,m_{N-k} \neq \ell\}.$$

Given the particular form of right-hand side vector $\mathbf{b}$, it follows that $\mathbf{d}$ is simply the scaled $(s+1)$-column of $\mathbf{A}^{-1}$. Thus,

$$\eta^h(\tilde{x}_\ell) = \begin{cases} s!(-1)^{N-1} \dfrac{\displaystyle\sum_{\mathbf{m}\in\mathcal{I}(N,k,\ell)} (\tilde{x}_{m_1} - x^*)\cdots(\tilde{x}_{m_{N-k}} - x^*)}{h^N \displaystyle\prod_{\substack{1\le m\le N \\ m\neq\ell}} (\ell - m)}, & \text{for } q > 1 \\ \dfrac{s!(-1)^s}{h^N \displaystyle\prod_{\substack{1\le m\le N \\ m\neq\ell}} (\ell - m)}, & \text{for } q = 1 \end{cases} \tag{3.5}$$

Equation 3.5 is used to generate gridded functions η^{h_k} satisfying the discrete (q, s_k)-moment conditions at $x_k^* \in \mathbb{R}$ on each dimension $k = 1, ..., d$. Approximations on higher dimension are then constructed by taking the tensor product of the 1-D approximations. Note, however, that in order for theorem 3.2 to apply it is required that the multi-variate grid function, that is $\eta^h(\mathbf{x}) = \eta^{h_1}(x_1) \cdots \eta^{h_d}(x_d)$, satisfy the discrete $(q, \mathbf{s})$-moment conditions. Though it may not appear obvious, the proposition below shows that my tensor construction indeed satisfies the appropriate discrete moment conditions.

Theorem 3.3. *Let $q \in \mathbb{N}$, multi-index $\mathbf{s}$, and $\mathbf{x}^* \in \mathbb{R}^d$ be given. Suppose $\eta^h : \mathcal{G}(\mathbf{x}_0, \mathbf{h}) \to \mathbb{R}$ is a multi-variate grid function given by the tensor product of 1-D grid functions $\eta^{h_k} : \mathcal{G}(x_{0,k}, h_k) \to \mathbb{R}$. If η^{h_k} satisfy the discrete (q, s_k)-moment conditions at x_k^* for all $k = 1, ..., d$, then it follows that η^h satisfies the discrete $(q, \mathbf{s})$-moment conditions at $\mathbf{x}^*$.*

Proof. Suppose for each $k = 1, ..., d$ that η^{h_k} satisfies the discrete (q, s_k)-moment conditions at x_k^*. Let α be some multi-index with $0 \leq |\alpha| \leq q + |\mathbf{s}| - 1$. Note that,

$$M_\alpha^h(S^h, \mathbf{x}^*) = \prod_{k=1}^{d} M_{\alpha_k}^{h_k}(\eta^{h_k}, x_k^*).$$

Clearly, if $\alpha_k \leq q + s_k - 1$ for all $k = 1, ..., d$, then the result follows from the supposition. Same applies for $\alpha = \mathbf{s}$. Suppose then, that there exists index ℓ such

that $\alpha_\ell > q + s_\ell - 1$, that is $a_\ell = q + s_\ell - 1 + i$ for some $i \in \mathbb{N}$. Thus,

$$|\alpha| = \sum_{k \neq \ell} \alpha_k + \alpha_\ell = \sum_{k \neq \ell} \alpha_k + q + s_\ell - 1 + i \leq q + |\mathbf{s}| - 1$$

$$\Longrightarrow \sum_{k \neq \ell} \alpha_k + i \leq \sum_{k \neq \ell} s_k.$$

which implies that $\alpha_k < s_k$ for at least one $k \neq \ell$; for this particular k, it follows that

$$M_{\alpha_k}^{h_k}(\eta^{h_k}, x_k^*) = s_k!(-1)^{s_k}\delta_{s_k\alpha_k} = 0$$

since it has been established that $\alpha_k \neq s_k$, i.e., the product over k is zero if $\mathbf{s} \neq \alpha$. $\square$

It is important to note that grid functions η^h as computed by equation 3.5, will be dependent on three things:

1. source location $\mathbf{x}^*$,
2. choice of grid $\mathcal{G}(\mathbf{x}_0, \mathbf{h})$,
3. and choice of support of η^h.

The last point refers to the fact that the center of the support, that is a^*, was never specified above; different choices of a^* will result in different grid functions. In practice, however, I will consider only grid functions that are centered at source location x^*, as shown in section 3.4.

3.3.2 Relating Discrete and Continuous Moments Conditions

The discrete $(q, \mathbf{s})$-moment conditions, for a given $\mathbf{x}^*$, yield gridded approximations from an explicit formula (equation 3.5) assuming that the diameter of the support of the grid function is equal to $(q + s_k)h_k$ in each dimension. Given that equation 3.5 is unique for a particular $\mathbf{x}^*$, I show that imposing the discrete moment conditions for all $\mathbf{x}^* \in \mathbb{R}^d$ in fact defines a function over the reals. Moreover, I show that these continuum functions satisfy the continuous moment conditions and thus define a sequence of distributions that converge to $D^{\mathbf{s}}\delta(\cdot; \mathbf{x}^*)$ in the weak-$*$ topology, a result previously not known.

Working in 1-D, I will assume that the continuum approximation η_H is of the following form:

$$\eta_H(x) = \begin{cases} P_\ell(x), & x \in [a_\ell, a_{\ell+1}), \text{ for } \ell = 1, ..., N \\ 0, & \text{otherwise} \end{cases} \tag{3.6}$$

where P_ℓ is some polynomial over the considered interval, and $a_\ell = a_1 + (\ell - 1)h$ for $\ell = 1, ..., N + 1$, given $a_1 < 0$ and $N = q + s$. In other words, η_H is a piecewise polynomial with support width of Nh and thus contained in $B(0, H)$ for $Nh \leq 2H < 2Nh$ depending on the choice of a_1.

Consider uniform grid $\mathcal{G}(0, h)$. Then there exists grid points $\{\tilde{x}_\ell\}_{\ell=1}^N \subset \mathcal{G}(0, h)$ contained in the interval $[a_1, a_{N+1})$ such that $\tilde{x}_\ell \in [a_\ell, a_{\ell+1})$ for each $\ell = 1, ..., N$. Let ℓ^* be the index where $0 \in [a_{\ell^*}, a_{\ell^*+1})$ (this is possible since $a_1 < 0$). Note that $\tilde{x}_{\ell^*} = 0$,

thus implying that $\tilde{x}_\ell = a_{\ell+1} - a_{\ell^*+1}$. Now consider x^* in the following interval,

$$\begin{aligned} & x^* \in (\tilde{x}_{\ell^*} - a_{\ell^*}, \tilde{x}_{\ell^*} - a_{\ell^*}] \\ \iff \quad & \tilde{x}_{\ell^*} - x^* \in [a_{\ell^*}, a_{\ell^*}). \end{aligned}$$

For such x^* it follows that

$$\begin{aligned} \tilde{x}_\ell - x^* &= (a_{\ell+1} - a_{\ell^*+1}) - x^* + \tilde{x}_{\ell^*} \\ &< (a_{\ell+1} - a_{\ell^*+1}) + a_{\ell^*+1} = a_{\ell+1} \end{aligned}$$

and

$$\begin{aligned} \tilde{x}_\ell - x^* &= (a_{\ell+1} - a_{\ell^*+1}) - x^* + \tilde{x}_{\ell^*} \\ &\geq (a_{\ell+1} - a_{\ell^*+1}) + a_{\ell^*} = a_\ell. \end{aligned}$$

In other words, $\tilde{x}_\ell - x^* \in [a_\ell, a_{\ell+1})$ for all $\ell = 1, ..., N$.

Let $\eta^h(\cdot; x^*)$ denote the grid function that satisfies the discrete (q, s)-moment conditions for a given $x^* \in (\tilde{x}_{\ell^*} - a_{\ell^*+1}, \tilde{x}_{\ell^*} - a_{\ell^*}]$. Then $\eta^h(\tilde{x}_\ell; x^*) = \eta_H(\tilde{x}_\ell - x^*)$ defines η_H over $[a_\ell, a_{\ell+1})$ by allowing x^* to vary over the prescribed interval. Moreover, I slightly modifying equation 3.5 as a function of $x = \tilde{x}_\ell - x^*$ defines the $P_\ell(x)$ polynomials of η_H,

$$P_\ell(x) = \begin{cases} s!(-1)^{N-1} \dfrac{\displaystyle\sum_{\mathbf{m}\in\mathcal{I}(N,s+1,\ell)} (h(m_1-\ell)+x)\cdots(h(m_{q-1}-\ell)+x)}{h^N \displaystyle\prod_{\substack{1\le m\le N \\ m\neq\ell}} (\ell-m)}, & \text{for } q>1 \\ \dfrac{s!(-1)^s}{h^N \displaystyle\prod_{\substack{1\le m\le N \\ m\neq\ell}} (\ell-m)}, & \text{for } q=1. \end{cases} \tag{3.7}$$

Inspection of equation 3.7 reveals that P_ℓ is a polynomial of degree $q-1$.

Given (q,s) and $a_1 < 0$ and $h > 0$ (to determine the support), equation 3.7 by construction defines a piecewise polynomial function η_H that in theory satisfies the discrete (q,s)-moment conditions for an arbitrary choice of grid origin $x_0 \in \mathbb{R}$, of the regular grid $\mathcal{G}(x_0,h)$, and source location x^* if the continuum function is adequately shifted. This conjecture is verified in the lemma below.

Lemma 3.1. *Let $q \in \mathbb{N}$ and $s \in \mathbb{N}_0$ be given. Let η_H be a piecewise polynomial function as given by equations 3.6 and 3.7 for a given $a_1 < 0$, $h > 0$. Then it follows that grid function $\eta^h(x_n; x^*) := \eta_H(x_n - x^*)$ satisfies the discrete (q,s)-moment conditions for a given regular grid $\mathcal{G}(x_0,h)$ and source location $x^* \in \mathbb{R}$. Thus, η_H is said to satisfy the discrete (q,s)-moment conditions for all $x^* \in \mathbb{R}$ independent of grid origin.*

Proof. Let $x_0, x^* \in \mathbb{R}$ be given. Then there exists $\{\tilde{x}_\ell\}_{\ell=1}^N \subset \mathcal{G}(x_0,h)$, with $N = q+s$, such that

$$\tilde{x}_\ell - x^* \in (a_\ell, a_{\ell+1}], \quad \forall \ell = 1, ..., N.$$

Replacing x with $\tilde{x}_\ell - x^*$ in equation 3.7 gives back equation 3.5, which implies that $\eta^h(\tilde{x}_\ell; x^*)$ satisfies the discrete (q,s)-moment conditions at x^*. □

Theorem 3.4. *Let $q \in \mathbb{N}$ and $s \in \mathbb{N}_0$ be given. Suppose η_H satisfies the discrete (q,s)-moment conditions for all $x^* \in \mathbb{R}$ independent of grid origin. In other words η_H is a piece-wise polynomial as given by equations 3.6 and 3.7 for a given $a_1 < 0$ and $h > 0$. Then it follows that η_H also satisfies the (q,s)-moment conditions.*

Proof. Evaluate the α-moment of η_H for $\alpha = 0, ..., q+s-1$;

$$\begin{aligned} M_\alpha(\eta_H) &= \int_{\mathbb{R}} \eta_H(x) x^\alpha \, dx \\ &= \sum_{\ell=1}^{N} \int_{a_\ell}^{a_{\ell+1}} P_\ell(x) x^\alpha \, dx. \end{aligned}$$

Apply the following change of variables, $x = a_\ell + \xi$ with $\xi \in [0, h)$ over each interval $[a_\ell, a_{\ell+1})$;

$$\begin{aligned} M_\alpha(\eta_H) &= \sum_{\ell=1}^{N} \int_0^h P_\ell(a_\ell + \xi)(a_\ell + \xi)^\alpha \, d\xi \\ &= \int_0^h \frac{1}{h} \left[h \sum_{\ell=1}^{N} P_\ell(a_\ell + \xi)(a_\ell + \xi)^\alpha \right] \, d\xi. \end{aligned}$$

Note that the term in the bracket coincides with the discrete α-moment of η_H with respect to a uniform grid $\mathcal{G}(x_0, h)$ containing stencil points $\{a_\ell\}_{\ell=1}^{N+1}$ for a source

located at $x^* = -\xi$. Using lemma 3.1 I can conclude

$$M_\alpha(\eta_H) = \int_0^h \frac{1}{h} \left[s!(-1)^s \delta_{s\alpha} \right] \, d\xi$$
$$= s!(-1)^s \delta_{s\alpha}.$$

□

Results of theorem 3.4 can be extended to higher dimensions by taking tensor product of the 1-D constructions as suggested in the previous subsection, and applying the same logic as in theorem 3.3. Convergence (point-wise in the distribution sense) as $H \to 0$ of η_H of the form given by equation 3.6 and 3.7 follows from theorem 3.1 if it can be shown that the sequence of functions satisfy estimate 3.3 uniformly in $H > 0$. In 1-D, note that η_H consist of piecewise polynomials of order $q - 1$ divided by a factor of h^N, where $N = q + s$. Since $H = O(h)$ it follows that

$$\sup_{x \in B(0,H)} |\eta_H(x)| = O(H^{-s-1}).$$

Thus

$$\int_{B(0,H)} dx \, |\eta_H(x)| \, |x^s| \leq \sup_{B(0,H)} |\eta_H(x)| \int_{B(0,H)} dx \, |x^s| = O(1).$$

Similar for constructions η_H in higher spatial dimensions.

3.4 Examples

Convergence rate results in the next chapter will employ the singular source approximation discussed here, replacing multipole terms with gridded functions to be used in finite difference schemes. Equations 3.6 and 3.7 define the continuum form of the approximations, where gridded functions are obtained by shifting and sampling over a given grid. The following figures plot 1-D and 2-D continuum approximations η_H related to grid functions used throughout the numerical tests in upcoming chapters. In particular I plot second- and fourth-order approximations of $D^s\delta$ for $s = 0, 1, 2$ in 1-D and $\mathbf{s} = (0,0), (0,1), (0,2)$ in 2-D, with $h = 1$. 2-D approximations are constructed via tensor product of 1-D approximations as discussed in this chapter.

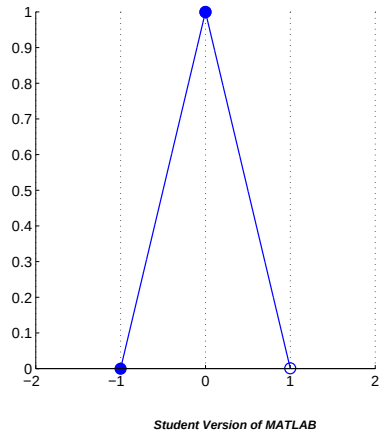

(a) $s = 0,\ q = 2$

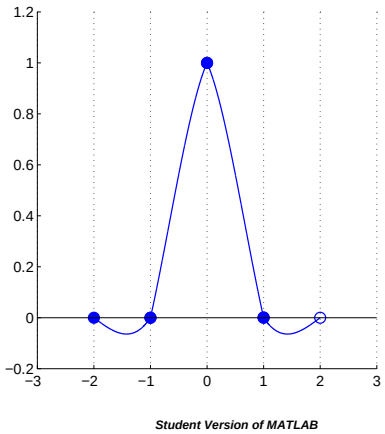

(b) $s = 0,\ q = 4.$

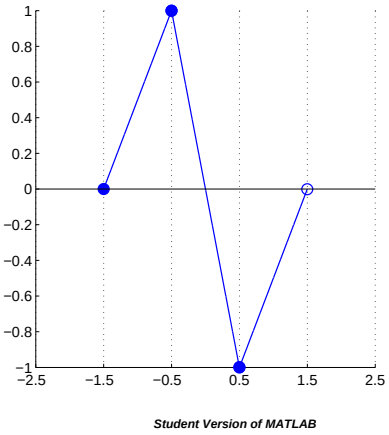

(c) $s = 1,\ q = 2$

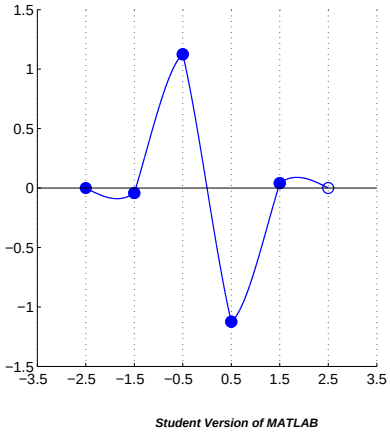

(d) $s = 1,\ q = 4$

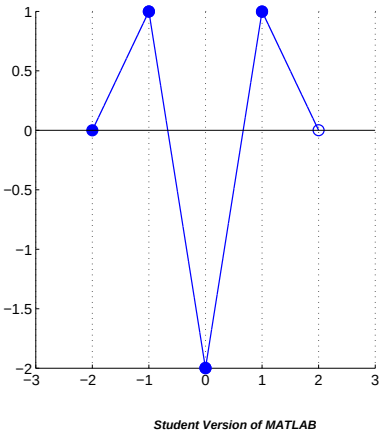

(e) $s = 2,\ q = 2$

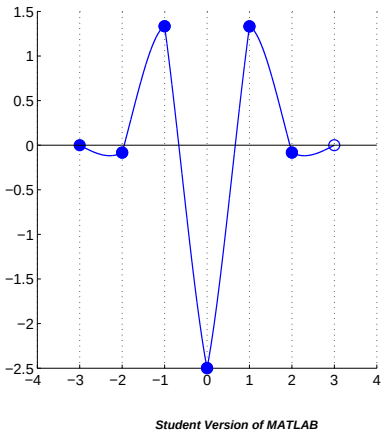

(f) $s = 2,\ q = 4$

Figure 3.1 : Plots of η_H, 1-D approximations to $D^s\delta$ with $h = 1$.

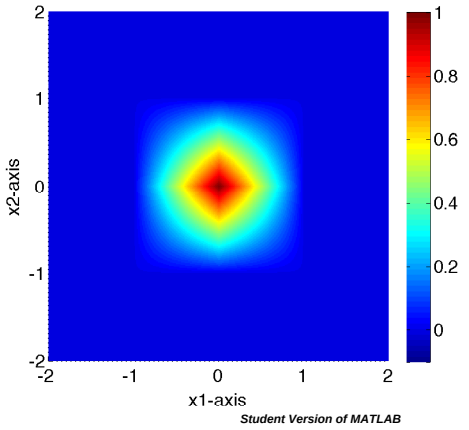

(a) $\mathbf{s} = (0, 0),\ q = 2$

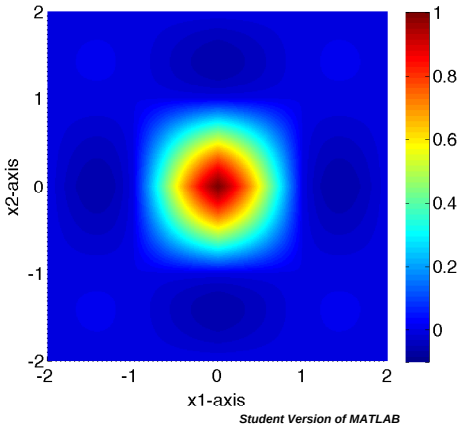

(b) $\mathbf{s} = (0, 0),\ q = 4$

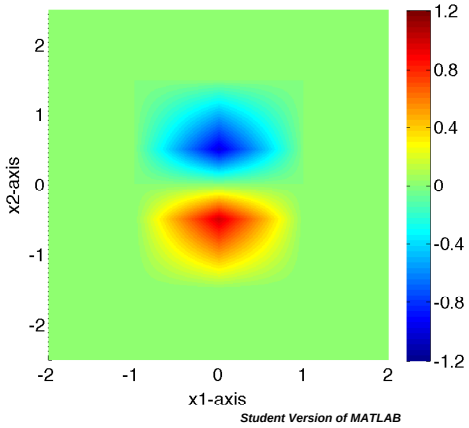

(c) $\mathbf{s} = (0, 1),\ q = 2.$

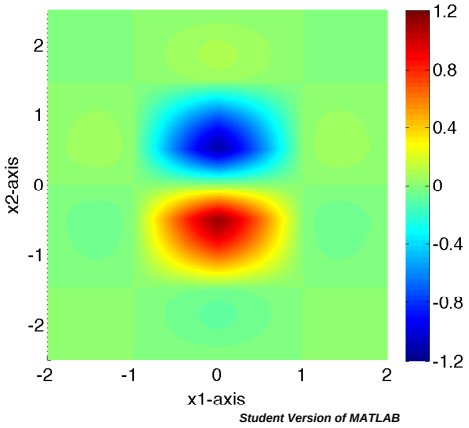

(d) $\mathbf{s} = (0, 1),\ q = 4.$

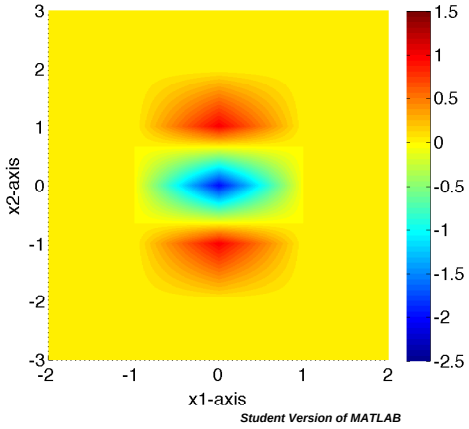

(e) $\mathbf{s} = (0, 2),\ q = 2.$

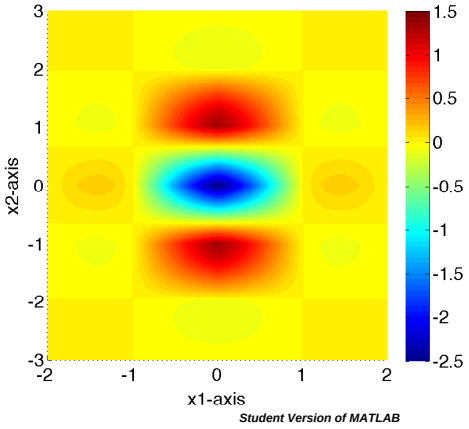

(f) $\mathbf{s} = (0, 2),\ q = 4.$

Figure 3.2 : Plots of η_H, 2-D approximations to $D^{\mathbf{s}}\delta$ with $h = 1$.

Chapter 4

Wave Modeling with Multipole Sources

4.1 Introduction

Recall multipole expansions for scalar, vector, and tensor sources, given by equations 2.6 and 2.7. For each i, j, I choose a multivariate grid function η_{ij}^h to replace each $D^{\mathbf{s}_{ij}}\delta(\mathbf{x} - \mathbf{x}^*)$ in equations 2.7. Clearly this choice depends on $\mathbf{x}^*$, which will be implicitly assumed. Given these choices, the *discrete multipole expansion*, in the scalar, vector, and tensor cases are:

$$\begin{aligned} f_{\mathbf{n}}^h(t) &= \sum_i w_i(t) b_{i,\mathbf{n}}^h, \\ \mathbf{f}_{\mathbf{n}}^h(t) &= \sum_i w_i(t) \mathbf{b}_{i,\mathbf{n}}^h \\ \mathbf{F}_{\mathbf{n}}^h(t) &= \sum_i w_i(t) \mathbf{B}_{i,\mathbf{n}}^h, \end{aligned} \tag{4.1}$$

with

$$\begin{aligned} b_{i,\mathbf{n}}^h &= \sum_j c_{ij} \eta_{ij,\mathbf{n}}^h \\ \mathbf{b}_{i,\mathbf{n}}^h &= \sum_j \mathbf{c}_{ij} \eta_{ij,\mathbf{n}}^h \\ \mathbf{B}_{i,\mathbf{n}}^h &= \sum_j \mathbf{C}_{ij} \eta_{ij,\mathbf{n}}^h \end{aligned} \tag{4.2}$$

Remark: Throughout the mathematical development, I will continue to regard time as continuous, and write $w_i(t)$ for the multipole coefficients. Of course, in any implementation time will be discretely sampled as well.

Discretization of multipole sources, that is equations 4.2, produces gridded approximations 4.1, where the formula may be viewed as defining a discrete version L^h of the MPS-to-RHS map (equation 2.11):

$$(L^h w)_{\mathbf{n}}(t) = \sum_i w_i(t) b^h_{i,\mathbf{n}}. \tag{4.3}$$

I call L^h the *discrete MPS-to-RHS* map. Its output (vector in range) may be used as the right-hand side in a finite difference approximation to acoustodynamics (equations 2.4) or elastodynamics (equations 2.5). The domain of this map is a discrete version of the MPS space described in the computational implementation section.

Consider the following abstract PDE problem with singular source term f; find u such that

$$\mathcal{P}u = f,$$

where $\mathcal{P}$ is some differential operator. I am of course interested in the case where the PDE above corresponds to the acoustic and elasticity equations with multipole source terms. Let f^h denote a discrete approximation to f over some uniform grid. Moreover, let u^h denote the finite difference solution with f^h source term, that is, u^h is the solution to discretized problem $\mathcal{P}^h u^h = f^h$ where $\mathcal{P}^h$ is the finite difference

discretization of differential operator $\mathcal{P}$. The choice of approximation f^h should of course help solve the original problem, that is $u^h \to u$ as $h \to 0$ where u is the continuum solution to equation 4.1 (i.e., consistency). Moreover, errors introduced by the source approximation should be controlled in a manner consistent with the choice of finite difference solver.

In chapter 3 I developed a systematic approach for constructing gridded functions that approximate derivatives of the delta function, and hence multipoles. In particular, grid functions η_{ij}^h in equation 4.2 are chosen so that they satisfy discrete moment conditions 3.2 with derivative multi-index $\mathbf{s}_{ij}$ and a given choice of approximation order q. The following question arises: How does our choice of source approximation impact the accuracy of the finite difference solution using said discrete source f^h as an approximation to the continuum solution for systems 2.4 or 2.5 with multipole source f?

This chapter delves into the topic of wave modeling (primarily via acoustics) with multipole sources. I conjecture that finite difference solutions will converge at optimal rates as suggested by the numerical scheme away from the source location if source approximation order is adequately chosen. Though I do not provide a proof for this conjecture at the moment, I give my current insight in section 4.2, primarily elaborating on properties of staggered-grid finite difference methods considered in this work, that is, energy conserving schemes for first order systems like acoustics. The subsequent section develops the computational framework for implementing the

multipole source representation discussed in the second chapter, the singular source approximation as the discrete MPS-to-RHS map, and joins the latter with finite difference solvers for wave propagation. The last section provides numerical results demonstrating the accuracy of my proposed multipole source approximations. Specifically, I show that finite difference solutions achieve optimal convergence rates away from the source when using source approximation of matching order with the spatial discretization of the finite difference scheme.

4.2 Singular Source Approximation and Energy Conservative FD Schemes

I am interested in finite difference schemes for the acoustic or elasticity equations given in first order form by systems 2.4 and 2.5 respectively. For simplicity I focus primarily on the 2-D acoustic system for the remainder of this section, though the ideas and theory discussed here have been applied to 3-D and the elasticity equations as well.

The finite difference methods considered in this thesis are the acoustic variant of the second-order in time and second- and fourth-order in space, commonly referred to as the 2-2 and 2-4 order schemes respectively, staggered grid methods proposed by Virieux (1986) and Levander (1988), explained below. Assume that the spatial and temporal domains of interest are discretized by a space-time grid with uniform grid size of $h > 0$ in space and $\Delta t > 0$ in time. Let $u = (p, v_1, v_2)$ denote the continuum

fields and $u^h = (p^h, v_1^h, v_2^h)$ their discretized counterparts, where

$$(p^h)_{ij}^n \approx p(ih, jh, n\Delta t),$$

$$(v_1^h)_{i+\frac{1}{2},j}^{n+\frac{1}{2}} \approx v_1((i+\tfrac{1}{2})h, jh, (n+\tfrac{1}{2})\Delta t)$$

$$(v_1^h)_{i,j+\frac{1}{2}}^{n+\frac{1}{2}} \approx v_2(ih, (j+\tfrac{1}{2})h, (n+\tfrac{1}{2})\Delta t).$$

Note that the velocity fields contain indexes shifted by 1/2 along one of the space coordinates and in time, that is staggered in time and space. Figure 4.1 illustrates the distribution of the discretized fields over staggered space-time grids. The grid related to integer indexes is referred to as the *primary grid* corresponding to solid grid lines in figure 4.1, while the shifted grids represented by dashed lines are known as *dual* or *staggered grids*. For a particular time index n, $(u^h)^n$ is defined as

$$(u^h)^n = ((p^h)^n, (v_1)^{n-\frac{1}{2}}, (v_2)^{n-\frac{1}{2}}).$$

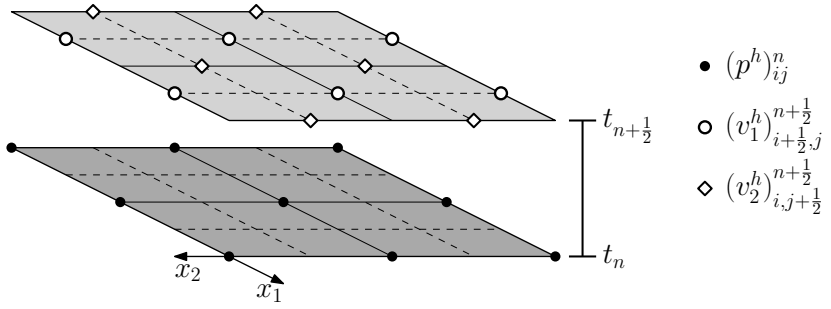

Figure 4.1 : Staggered space-time grid distribution of gridded functions p^h, v_1^h, v_2^h for the 2-2 and 2-4 staggered grid method.

The staggered-grid finite difference method for the acoustic equations 2.4 is given as follows:

$$
\begin{aligned}
(p^h)_{ij}^{n+1} &= (p^h)_{ij}^{n} - \Delta t \kappa_{ij} \left\{ D_{x_1}^h (v_1^h)_{ij}^{n+\frac{1}{2}} + D_{x_2}^h (v_2^h)_{ij}^{n+\frac{1}{2}} \right\} + \Delta t (f)_{ij}^{n+\frac{1}{2}} \\
(v_1^h)_{i+\frac{1}{2},j}^{n+\frac{1}{2}} &= (v_1^h)_{i+\frac{1}{2},j}^{n-\frac{1}{2}} - \Delta t \beta_{i+\frac{1}{2},j} D_{x_1}^h (p^h)_{i+\frac{1}{2},j}^{n} + \Delta t (f_1)_{i+\frac{1}{2},j}^{n} \\
(v_2^h)_{i,j+\frac{1}{2}}^{n+\frac{1}{2}} &= (v_2^h)_{i,j+\frac{1}{2}}^{n-\frac{1}{2}} - \Delta t \beta_{i,j+\frac{1}{2}} D_{x_2}^h (p^h)_{i,j+\frac{1}{2}}^{n} + \Delta t (f_2)_{i,j+\frac{1}{2}}^{n}
\end{aligned}
$$

where $D_{x_1}^h$ is the centered difference approximation of $\frac{\partial}{\partial x_1}$, defined by

$$
D_{x_1}^h g(x_1, x_2) = \frac{1}{h} \Big(g(x_1 + \tfrac{1}{2}h, x_2) - g(x_1 - \tfrac{1}{2}h, x_2) \Big)
$$

for the 2-2 scheme and

$$
D_{x_1}^h g(x_1, x_2) = \frac{1}{h} \Big(\tfrac{1}{24} g(x_1 + \tfrac{3}{2}h, x_2) - \tfrac{9}{8} g(x_1 + \tfrac{1}{2}h, x_2) + \tfrac{9}{8} g(x_1 - \tfrac{1}{2}h, x_2) - \tfrac{1}{24} g(x_1 - \tfrac{3}{2}h, x_2) \Big)
$$

for the 2-4 scheme. Similar for $D_{x_2}^h$.

Numerical schemes 4.5 are particularly special in that they conserve discrete energy E^n,

$$
\begin{aligned}
E^n(u^h) \;:=\; & \frac{1}{2} \Big\langle \tfrac{1}{\kappa} (p^h)^n, (p^h)^n \Big\rangle + \frac{1}{2} \Big\langle \tfrac{1}{\beta} (v_1^h)^{n-\frac{1}{2}}, (v_1^h)^{n-\frac{1}{2}} \Big\rangle + \frac{1}{2} \Big\langle \tfrac{1}{\beta} (v_2^h)^{n-\frac{1}{2}}, (v_2^h)^{n-\frac{1}{2}} \Big\rangle \\
& + \frac{1}{2} \Delta t \Big\langle D_{x_1}^h (v_1^h)^{n-\frac{1}{2}} + D_{x_2}^h (v_2^h)^{n-\frac{1}{2}}, (p^h)^n \Big\rangle
\end{aligned}
$$

where

$$\left\langle (p^h)^n, (p^h)^n \right\rangle = h^2 \sum_{i,j} (p^h)^n_{ij} (p^h)^n_{ij}$$

and similar discrete inner-products for terms involving grid functions on dual grids. In other words, if u^h is a solution to finite difference equations 4.5 with homogeneous source terms and boundary conditions, then $E^n(u^h) = E^{n+1}(u^h)$ for all n. It can be shown that the discrete energy in fact defines a norm that is equivalent to the discrete spatial norm $\|\cdot\|$ induced by the discrete inner-product, i.e., there exists $0 < C_* \leq C^*$ such that

$$C_* \|(u^h)^n\| \leq E^n(u^h) \leq C^* \|(u^h)^n\|. \tag{4.6}$$

Furthermore, the energy can be bounded by initial conditions and inhomogeneous source terms: there exists $K \geq 0$ and $\lambda > 1$ such that

$$E^n(u^h) \leq \lambda^n E^0(u^h) + Kh \sum_{m=0}^{n-1} \lambda^{n-m+1} \left(\|(f_1)^{m-\frac{1}{2}}\|^2 + \|(f_2)^{m-\frac{1}{2}}\|^2 + \|(f)^m\|^2 \right). \tag{4.7}$$

Convergence can thus be proven using consistency and stability of the numerical method, where stability follows from equations 4.6 and 4.7; see Gustafsson and Mossberg (2004), Gustafsson and Wahlund (2004b), and Gustafsson and Wahlund (2004a) for relevant analysis of staggered-grid finite difference schemes based on energy estimates.

Let u and u^* denote the continuum solutions to the acoustic equations with multipole source f and with its regularized source term f^h respectively. Moreover, let u^h

denote the finite difference solution with source f^h. Thus,

$$\|u - u^h\|_X \leq \|u - u^*\|_X + \|u^* - u^h\|_X,$$

where $\|u-u^*\|_X$ is the error associated with regularizing the multipole source term f and $\|u^*-u^h\|_X$ is finite difference error involving a regular source term f^h under some suitable norm $\|\cdot\|_X$. Convergence analysis can easily be applied to the finite difference error. The regularization error is a different story and is currently the missing piece. I note that none of the theory in current literature, including the papers cited in chapter 3, provides the relevant error analysis for my particular problem, that is staggered-grid finite difference methods applied to linear acoustics or elasticity with multipole sources. I conjecture that point-wise convergence at optimal rates given by the finite difference scheme can be achieved away from the source location when discretizing singular sources as prescribed by the moment conditions discussed in chapter 3. Though no actual proof is given at the moment, numerical results in this chapter corroborate this conjecture.

4.3 Computational Framework

This section describes an implementation of the multipole representation, equations 2.6 and 2.7, with

- natural input, namely the time-dependent multipole coefficients $\{w_i\}$,

- natural output, namely time series attached to points on a regular grid that can be fed as source functions to a finite-difference wave equation solver,
- a flexible object-oriented implementation that follows closely the structure of the underlying mathematics.

To achieve the second goal I use the approach developed in chapter 3 to systemically construct discrete approximations to multipole sources that preserve optimal convergence order of finite difference solutions to wave equations on regular grids, regardless of the actual location $\mathbf{x}^*$ (on- or off-grid).

The overarching software design principle of this project is to organize the computation in a fashion as parallel as possible with the underlying mathematics. The mathematical venue of the computations is vector calculus and linear algebra. However, the key concepts of vector calculus - vectors, linear operators, vector-valued functions, derivatives, and so on - have no immediate reflection in the basic types of any high-level programming language. The programmer of numerical algorithms such as those described here must define the missing types and provide them with the proper behavior. While straightforward programming with native arrays, in the fashion traditional to computational science, can express vector calculus algorithms, such expression does not encompass (for example) data stored on disk or in a network, and the additional code required to deal with such extensions inevitably intrudes into the expression of mathematical algorithms to which they are irrelevant.

Programming with abstract types - that is, types defined by their behavior rather than their implementation or data structure details - provides a way out of this dilemma, allowing expression of abstract algorithms that apply transparently, regardless of data structure and low-level computational details. Code centered around programmer-defined types has come to be called *object oriented*. While object-oriented design can be implemented in almost any language environment, some programming languages (C++, Python, Java,...) offer explicit support for type definition and use. I chose to program in C++, representing abstract numerical types as C++ classes. In particular, I have realized the multipole source construction explained in chapter 2.6 using the C++ packages *IWave* and *Rice Vector Library* (RVL); (Symes et al., 2011; Padula et al., 2009). The IWave package is a framework for finite difference solvers over uniform grids while the RVL package provides a system of classes for expression of gradient-based optimization algorithms over Hilbert spaces. IWave and RVL come together to form a modeling engine for seismic inversion and migration. Implementation of multipole sources as RVL objects enables straightforward composition with IWave solvers and inclusion in inversion algorithms powered by RVL optimization code. Any other wave equation solver wrapped in the appropriate RVL interfaces could be coupled to the multipole source objects in the same way.

RVL

The Rice Vector Library (RVL) (Padula et al., 2009) is an attempt to mimic the structure of vector calculus in a system of C++ classes, so that common linear algebra and optimization algorithms may be expressed in natural and portable form.

RVL provides the basic interfaces for defining abstract vector calculus types in C++ and coding of important numerical algorithms in terms of these types. Other packages offer a similar application programmer interface but tend to imprint the needs of particular application areas in the core design. Recent examples include Trilinos Rapid Optimization Library for simulation-driven optimization (Kouri et al., 2015) and Operator Discretization Library for biomedical tomography (Öktem, 2016). Amongst these, RVL alone is built on those interfaces, and only those interfaces, native to the mathematics underlying continuous optimization and linear algebra.

The class `RVL::Space` expresses the central abstraction of calculus in Hilbert space, namely the Hilbert space. It acts as an abstract factory for `RVL::Vector`s, realizing in code the mathematical commonplace "let x be a member of V". `RVL::LinearOp` subtypes implement matrix-vector and transpose (adjoint) matrix-vector product, without requiring explicit storage of a matrix. `RVL::Operator`s are nonlinear vector-valued functions, with derivatives and second derivatives and their transposes. Just as a linear operator is a special type of operator, `RVL::LinearOp` is a subclass of `RVL::Operator`. Operators act as vectors - they can be added and multiplied by scalars - but there is no natural inner product on the vector space of operators. Since

`RVL::Space` realizes the structure of Hilbert space, `RVL::LinearOp` cannot be regarded as a subclass of `RVL::Space`. However linear-operator valued functions are useful and occur naturally. So a separate `RVL::LinOpValOp` class is supplied to express such behavior, as an appropriate subclass of `RVL::Operator`. I give an example of its use below.

For much more detail, design considerations, and examples see Padula et al. (2009).

Out of core classes

I have built the framework described here on top two open source seismic data processing packages, *Seismic Unix* (SU, (Cohen and Stockwell, 2015)) and *Madagascar* (Fomel, 2009). Both packages offer extensive file-to-file utilities based on two different file data formats. The SU variant of SEGY tape format consists of SEGY traces without reel headers. I refer to this as SU file format and use it to represent time series data throughout the project. The Madagascar file format, *Regularly Sampled Function* (RSF) is ideal for rectangularly gridded data. Since I will couple the MPS representation to finite difference codes on regular grids, RSF format is natural to represent grids and spatial functions on them.

I have built `RVL::Space` classes around these file formats, with appropriate in-core data structures mirroring the information content of the file data. These will be described in detail below.

IWave

IWave is a wave equation simulator code, implementing several wave propagation models. The one used in my examples is staggered grid acoustodynamics (equations 4.5). Each of these models defines a map F^h from the pair, consisting of medium parameters m^h and source (right-hand side) parameters f^h, to data traces d^h:

$$F^h[m^h]f^h = d^h. \tag{4.8}$$

The notation is meant to suggest the linearity of F^h in the source parameter vector f^h, and to remind the reader that all of these objects are discrete approximations based on a grid of diameter h. F^h defines a linear operator (on f^h) valued function of m^h. RVL supplies the class `RVL::LinOpValOp` for abstracting the behavior of such things, and wraps the IWave simulation code in this interface. The domain is the Cartesian product of the mechanical parameter space, a product of `RVL:Space`'s encapsulating out-of-core RSF data, and an `MPS_Space` as described below. The range is an `RVL::Space` (or Cartesian product of same) based on SU trace data. The action of the operator is file-to-file, very much like most SU and Madagascar utilities.

Along with the modeling relation 4.8, IWave also provides access to derivatives and adjoints as is appropriate for assembling inversion code. See Fehler and Keliher (2011) for the use of an earlier version in QC of phase I of the SEAM project, Symes et al. (2011) discussion of the design and implementation of the IWave inversion

interface, and Symes (2014) for a detailed description of the overall code design.

MPS Implementation

The three major constructs of the multipole framework are MPS spaces, the MPS-to-RHS operator, and the composition of the latter with a wave equation simulator to create an MPS-to-data modeling operator. The framework is built out of RVL types, which are explicitly adapted to out-of-core data such as is stored in the SU and RSF data formats.

MPS Space

The subclass `MPS_Space` of `RVL::Space` implements the MPS space abstraction described in chapter 2. As MPS spaces are parametrized by multipole bases, `MPS_Space` is an abstract or purely virtual class with three purely virtual member functions:

- `get_MPS_basis()`, returning a list of multipole basis vectors in the form of a `std::vector<MPS_base>`;
- `get_type()` returns an identifying `std::string` for use in error messages and the like;
- `clone()`, a virtual copy constructor mandated by the base class `RVL::Space`.

An `MPS_base` stores a vector of derivative index vectors, for example [0,0,0] for no derivative (monopole), [1,0,0] for dipole in the first direction, [1,1,0] for a double

couple in the (1,2) coordinate plane, [0,0,2] for a second order multipole in the 3rd direction, etc. Examples of `get_MPS_basis()` for various MPS space types may be found in the directory `iwave/mps/lib/MPS_Space_Examples.cc`. These examples also show how to implement the virtual copy constructor `clone()` of the `RVL::Space` class, by calling operator `new` using the copy constructor of the class. Once `get_MPS_basis()`, `get_type()`, and `clone()` are defined in a subclass of `MPS_Space`, that subclass is fully defined and may be instantiated.

The main constructor of `MPS_Space` is inherited by every subspace and may be used in lieu of a subspace constructor. Its arguments are

- an `MPS_KEYS` struct, and
- a `PARARRAY`.

`PARARRAY` is an associative array class, part of the `iwave/base` package. It stores `key=value` pairs and offers a number of convenient manipulation routines. A `PARARRAY` can be read from the command line or from a file recording key-value pairs. The file format constraints are quite non-restrictive compared to other similar packages appearing in similar applications. For example, whitespace is inconsequential, and key-value pairs are extracted by finding two strings without white space, separated by an "=" sign surrounded by any amount of white space. Any other string pattern is treated as a comment, which makes files defining `PARARRAYS` easy to annotate.

`MPS_KEYS` is a kitchen-sink struct listing all key strings needed by any of the MPS classes to extract values from `PARARRAY`s. For `MPS_Space`, the two members of

MPS_KEYS that must be initialized are

- grid_file - the key used to identify an RSF-formatted gridded data file pair defining the simulation grid, usually the name of one of the spatial coefficient arrays such as bulk modulus or density, and
- MPS_file - key used to identify an SU file containing traces with the correct source geometry

Only the source geometry and time sampling info (SEGY keywords sx, sy, selev,ns, dt, delrt) are extracted from the MPS_file file data. The main purpose in passing the name of an SU file with these attributes, rather than the attributes themselves, is to provide a prototype file that can be simply copied to create new instances of RVL::Vector's in the MPS_Space. SU provides excellent file initialization utilities, and the MPS_file file is likely to play other roles beyond specifying geometry, such as being the source for multipole coefficient data, so this is a convenient way to transfer the admittedly small amount of information needed to initialized a space.

To illustrate these concepts with concrete, compilable code, I have created the MPS_howto example, consisting of an executable defined in the source directory iwave/mps/main. This example shows how all of the major constructs in my framework are built and used.

Construction of MPS_Space requires that an MPS_KEYS struct be initialized with at least the two items listed above. A fragment from MPS_howto.cc shows how this is done:

```
MPS_KEYS mks;

mks.MPS_file  = "MPS_file";

mks.grid_file = "bulkmod";

ExScal_MPS_Space mps_sp(mks,*pars);
```

`ExScal_MPS_Space` is a subclass of `MPS_Space`, defined in header file `MPS_howto.hh` in the MPS package `include` directory.

Having constructed an `MPS_Space` instance, it is simple to create an object corresponding to a vector in the space:

```
RVL::Vector<float> mps(mps_sp);

RVL::AssignFilename

  af_mps(RVL::valparse<string>(*pars,mks.MPS_file));

mps.eval(af_mps);
```

Line 1 of this fragment constructs `RVL::Vector` workspace `mps`, representing a vector in the space `mps_sp`. Note that a floating point representation of real numbers (in this case, `float`) parametrizes `RVL::Vector` via the C++ template mechanism. In fact, `MPS_Space` is a subclass of `RVL::Space<float>`. RVL accommodates other scalar fields, notably `double` and the `std::complex` specializations, but MPS is entirely a float (single precision real) package.

In line 3, `mps` is connected to file storage through use of function object `RVL::AssignFilename`, constructed in line 2. Evaluation (`eval(...)`) with this particular function object must be the first operation on the `RVL::Vector` after its creation, else RVL

will open a scratch file to hold the data array associated with the vector. Such scratch files are deleted upon return from the process in which they are created. For archival storage, the programmer must make explicit use of `RVL::AssignFilename`. In line 2, the `valparse` function extracts a string from the `PARARRAY` pointed to by `pars`, using the key string `mks.MPS_file`, and returns it for use as the archival filename, passed to the constructor of `RVL::AssignFilename`.

Lines 2 and 3 illustrate the encapsulation of data enforced throughout RVL: with few exceptions, the only interactions with the data underlying a vector - i/o, arithmetic, or otherwise - take place through evaluation of function objects such as `RVL::AssignFilename`. The white paper Padula et al. (2009) discusses at length the justification for this strict encapsulation.

MPS-to-RHS map

My framework realizes the discrete MPS-to-RHS map L^h (equation 4.3) as a subclass of `RVL::LinearOp`, an abstract base class encoding the behavior of a linear map or operator. Amongst other things, linear operators have domain and range (vector) spaces. Just so, two of `RVL::LinearOp`'s public member functions are `getDomain()` and `getRange()`, which return `const` references to the `RVL::Space`s representing domain and range respectively. Two other important functions are `applyOp` and `applyAdjOp`, implementing the matrix-vector product and transpose matrix-vector product respectively.

The class MPS_to_RHS implements the MPS-to-RHS map. The domain space of an instance is an MPS_Space, which is an argument to the constructor, along with MPS_KEYS and PARARRAY objects as was the case for MPS_Space:

```
mks.appx_ord  = "appx_ord";
mks.MPS_file  = "MPS_file";
mks.grid_file = "bulkmod";
mks.RHS_files.push_back("source_p");
MPS_to_RHS m2r(mks,*pars, mps_sp);
```

The keys bulkmod and source_p point to the names of files containing bulk modulus (a spatial field, therefore RSF format) and source traces for the pressure equation (first equation in system 2.4).

Another code fragment from MPS_howto.cc illustrates a typical usage of the RVL version of the MPS-to-RHS map:

```
RVL::Vector<float> rhs(m2r.getRange());
RVL::AssignFilename
  af_rhs(RVL::valparse<string>(*pars,mks.RHS_files[0]));
rhs.eval(af_rhs);
m2r.applyOp(mps,rhs);
```

Lines 1-3 show creation of a vector, this time in the range space of the MPS_to_RHS operator m2r, and link to archival file storage. In line 4, the MPS_to_RHS operator m2r

is applied to the multipole coefficient vector `mps`, created a few lines before, and the output written to `rhs`.

Composition of MPS and IWave

The range space of the discrete MPS-to-RHS operator is a space-time grid function, a discrete representation of a linear combination of delta functions. This is in principle exactly what is required as a right-hand side for the finite difference discretization of the wave equations 2.4 and 2.5.

As noted above, IWave implements the discrete forward modeling operator (equation 4.8) as an `TSOpt::IWaveLOVOp`, a subtype of `RVL::LinOpValOp`. This operator has a product space domain, consisting of pairs (acoustic parameter fields, source fields). To compute the data traces generated by a multipole represented by a multipole coefficient vector, the IWave operator must be chained or *composed* with the discrete MPS-to-RHS map (equation 4.3). As just noted, the latter operator is represented as a `RVL::LinearOp` in my framework.

RVL provides a number of classes for operator composition. These are of the type sometimes known as "decorator" or "wrapper" classes: they combine instances of various types to obtain the behavior of yet another type. In this instance, I use an `RVL::LinCompLOVOp`, which implements the composition

$$(m^h, w) \mapsto F^h[m^h, L^h w]. \tag{4.9}$$

The code fragment from MPS_howto.cc illustrates instantiation of a TSOpt::IWaveLOVOp and its composition with the RVL::LinearOp subtype MPS_to_RHS:

```
TSOpt::IWaveLOVOp iwop(m2r.get_pars(),stream);
RVL::LinCompLOVOp<float> IWOP(m2r,iwop);
```

At this point in the code, the MPS_to_RHS instance m2r has already been built. Its internal PARARRAY object contains all parameters needed by TSOpt::IWaveLOVOp as well. In particular, the file used by MPS_to_RHS is listed under the key words used to generate the linear part of the domain for TSOpt::IWaveLOVOp, so that the domain/range sanity checks built into the RVL::LinCompLOVOp are satisfied. RVL::LinCompLOVOp builds a functional RVL:LinOpValOp out of the two arguments to its constructor, implementing equation 4.9.

With the resulting composition, it is possible to compute the data directly from the MPS coefficient vector and the acoustic or elastic model parameter fields (density, bulk modulus,...). Since the operator classes built this way implement derivatives up to order two and their adjoints, it is possible to couple the results to RVL optimization code and so construct inversion applications. I defer any discussion of inversion to chapter 5, and examine the accuracy of the discrete multipole source approximation whose implementation I have now sketched.

4.4 Numerical Convergence Rate Tests

I use the code described in the last section to verify my conjectures regarding the accuracy of moment-consistent approximations to multipole sources reported in chapter 3. In particular, my numerical experiments explore the semi-discrete error of finite difference solutions given approximations to multipole sources, that is time discretization errors are minimized by taking sufficiently small time steps. I use IWave implementations of the 2-2 and 2-4 staggered grid finite difference schemes for the acoustic system 2.4. In these experiments, I consider only scalar (pressure) sources and pressure trace data; similar results are obtained with other choices. Boundary conditions are of PML type, as described by Hu et al. (2007), to simulate an unbounded domain.

Multipole sources considered in these numerical tests are of a scalar type spanned by a single basis function, of the form

$$f(\mathbf{x},t) = w_1(t)b_1(\mathbf{x}), \quad \text{where} \quad b_1(\mathbf{x}) = D^{\mathbf{s}}\delta(\mathbf{x}-\mathbf{x}^*)$$

for a given multi-index $\mathbf{s}$ and source location $\mathbf{x}^*$. The discretization of b_1 is chosen as to achieve a target order of convergence for the difference schemes, in most cases the nominal spatial order (2 for the 2-2 scheme, 4 for the 2-4 scheme). Again, the time step is fixed small enough that the time discretization error plays essentially no role in the global error - it reflects truncation error of the spatial derivative approximation only. MPS coefficient $w_1(t)$ for the simulated data is chosen to be a Ricker wavelet

with peak frequency of $5Hz$, see figure 4.2.

Convergence rate $R(\mathbf{x}_r)$ at a given receiver location $\mathbf{x}_r$ is approximated via Richardson extrapolation,

$$R(\mathbf{x}_r) = \log_2 \left(\frac{\|p_{4h}(\mathbf{x}_r, \cdot) - p_{2h}(\mathbf{x}_r, \cdot)\|}{\|p_{2h}(\mathbf{x}_r, \cdot) - p_h(\mathbf{x}_r, \cdot)\|} \right)$$

where p_h, p_{2h}, p_{4h} denote the computed pressure field via finite difference using a grid size $h, 2h, 4h$ respectively. The norm $\|\cdot\|$ is chosen to be either $\|\cdot\|_2$ or $\|\cdot\|_\infty$ defined by

$$\|p(\mathbf{x}_r, \cdot)\|_2 := \sqrt{\Delta t \sum_k |p(\mathbf{x}_r, t_k)|^2},$$

$$\|p(\mathbf{x}_r, \cdot)\|_\infty := \max_k |p(\mathbf{x}_r, t_k)|.$$

In the 2-D tests, coordinates are oriented such that the first component refers to depth and the second component to the horizontal axis. Similarly for 3-D, with the third coordinate pertaining to the remaining perpendicular direction. Figures 4.3 and 4.4 illustrate the physical domain and source-receiver geometry for convergence rate tests in 2-D and 3-D respectively. The following are some other specifications that apply to all tests carried out here:

- total recording time is $T = 1.5s$;
- spatial grid sizes $4h = 40m$, $2h = 20m$, $h = 10m$;
- simulation time step $\Delta t = 0.5ms$.

Note that the source location is chosen as to not coincide with a grid point for any of the computational uniform-grids. Moreover, the coarsest grid cell size is $40m$, which implies at least 15 grid *points per wavelength* (gpw) at peak frequency of $5Hz$ and 5 gpw at $15Hz$ (see figure 4.2b) in all numerical experiments, minimizing the effects of grid dispersion on approximated convergence rates.

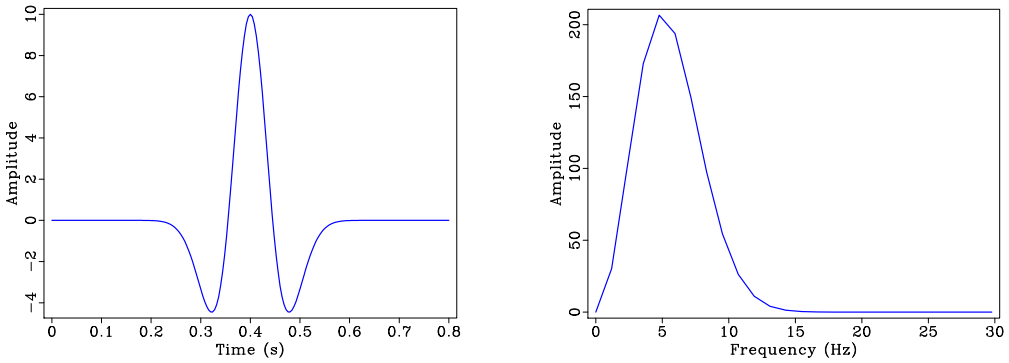

(a) Time trace. (b) Frequency spectrum.

Figure 4.2 : $5Hz$ peak frequency Ricker wavelet.

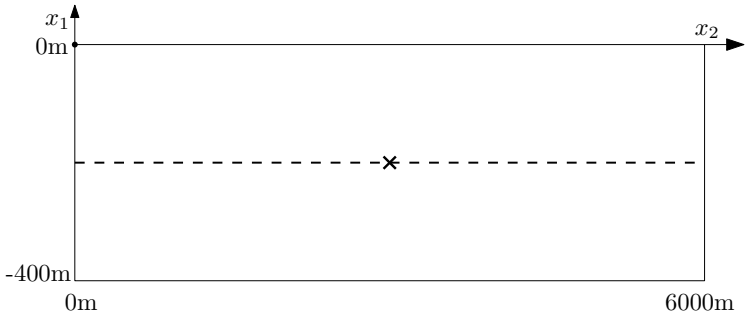

Figure 4.3 : Physical domain and source-receiver geometry specifications for 2-D convergence rate tests; constant density ($1g/cm^3$) and velocity ($3km/s$) medium, receiver positions $\mathbf{x}_{i_r} = (-200m, 0m : 40m : 6000m)$, source position $\mathbf{x}^* = (-203m, 3003m)$. Receivers and source depicted by a dashed line and a cross, respectively.

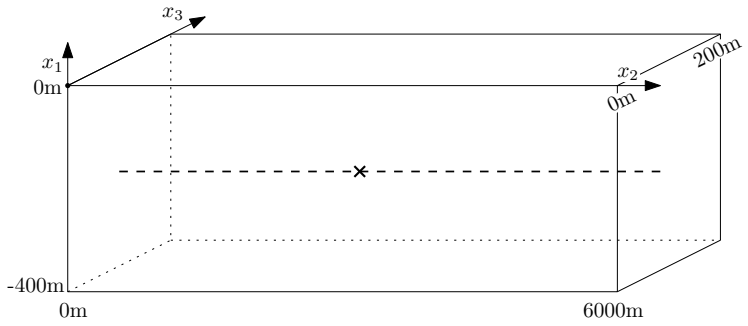

Figure 4.4 : Physical domain and source-receiver geometry specifications for 3-D convergence rate tests; constant density ($1g/cm^3$) and velocity ($3km/s$) medium, receiver positions $\mathbf{x}_{i_r} = (-200m, 0m : 40m : 6000m, 100m)$, source position $\mathbf{x}^* = (-203m, 3003m, 103m)$. Receivers and source depicted by a dashed line and a cross, respectively.

2-D Results

Figure 4.5 contains plots of the measured pressure field for different multipole sources used in the convergence rate experiments, namely $\mathbf{s} = (0,0), (0,1), (0,2)$. In particular, these plots are generated using the 2-4 finite difference scheme, a fourth-order source approximation, and spatial discretization of $h = 10m$. Different multipole sources exhibit polarity reversals (or lack of) as expected and an overall decrease in amplitude with increasing multipole order.

Convergence rate results are shown in figures 4.6 and 4.7 for the 2-2 and 2-4 schemes respectively, again using a matching source approximation order, plotting rates at varying receiver locations. Overall, optimal second- and fourth-order rates, when appropriate, are achieved at locations away from the support of the source approximation. The onset distance of optimal order convergence is roughly $h(q + |\mathbf{s}|)$ for the coarsest h used in the convergence study ($h = 40m$).

Figure 4.8 demonstates the negative effects of using the wrong multipole approximation order, namely second-order source approximations when using the 2-4 finite difference scheme. The theory makes no prediction in this case; apparently the convergence rate can be lower than would be the case with a difference scheme of lower order, even at a substantial distance from the source. For example figures 4.8a and 4.8c exhibit rates lower than two up to $1km$ away from source location.

3-D Results

Pressure field time traces are plotted in figure 4.9 for varying multipoles in 3-D, with $\mathbf{s} = (0,0,0), (0,1,0), (0,2,0)$. Figures 4.10 and 4.11 show convergence rate results analogous to the 2-D case, that is optimal rates are attained away from the source location. Also, the use of second-order source approximation in combination with the 2-4 finite difference scheme results in erratic convergence rates away from the source; see figure 4.12.

One clear pattern does arise from using lower order source approximations, evident in both 3-D and 2-D tests: errors associated with the source approximation seem to decay as the wave propagates away from the source location, at a faster rate than spatial discretization errors due to the finite difference operator. This claim is substantiated by an overall trend of increasing convergence rates with source-receiver distances in all cases.

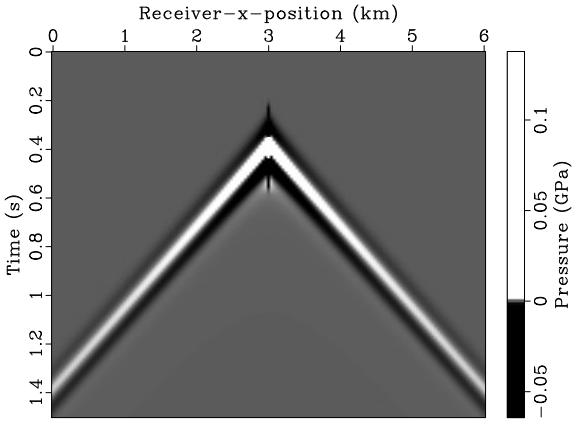

(a) $\mathbf{s} = (0, 0)$ case

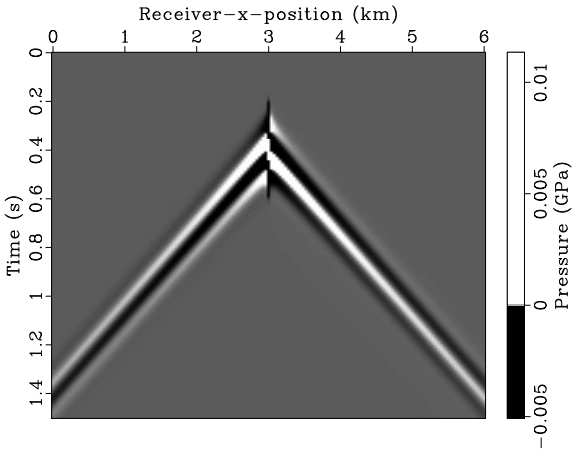

(b) $\mathbf{s} = (0, 1)$ case

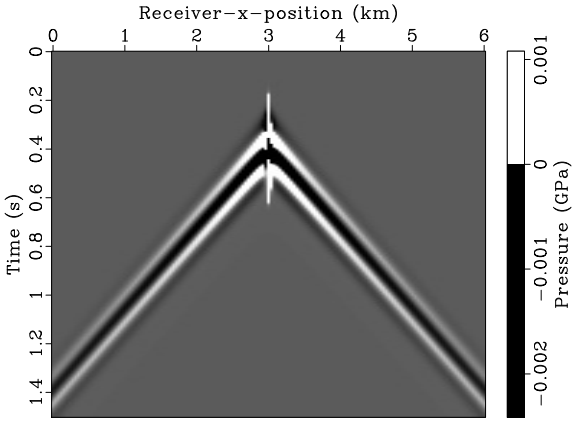

(c) $\mathbf{s} = (0, 2)$ case

Figure 4.5 : Pressure field traces (2-D acoustics) using 2-4 finite difference scheme (with $h = 10m$ and $\Delta t = 0.5ms$) and fourth-order source approximation for scalar multipole of type $f(\mathbf{x}, t) = w_1(t) D^{\mathbf{s}} \delta(\mathbf{x} - \mathbf{x}^*)$.

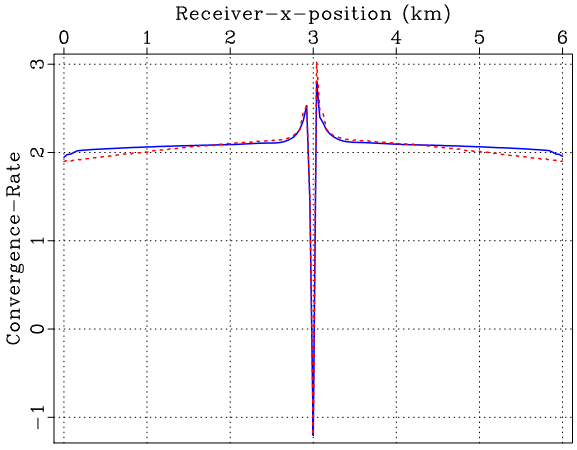

(a) $\mathbf{s} = (0, 0)$ case

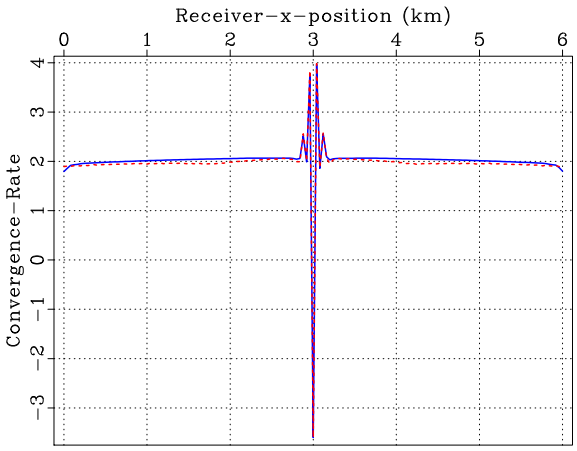

(b) $\mathbf{s} = (0, 1)$ case

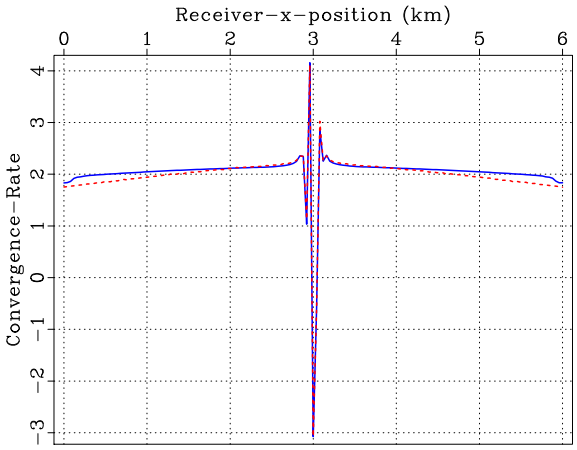

(c) $\mathbf{s} = (0, 2)$ case

Figure 4.6 : Approximate convergence rates of finite difference solutions to 2-D acoustics (pressure data only) using 2-2 scheme and second-order source approximation for scalar multipole of type $f(\mathbf{x}, t) = w_1(t) D^{\mathbf{s}} \delta(\mathbf{x} - \mathbf{x}^*)$. Rates computed using L^2 (solid blue) and L^∞ ($--$ red) norms.

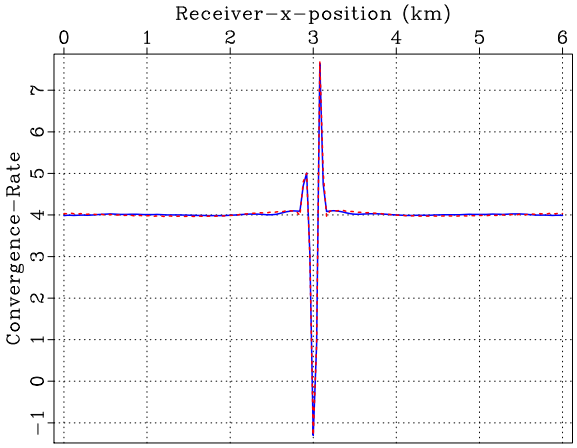

(a) $\mathbf{s} = (0, 0)$ case

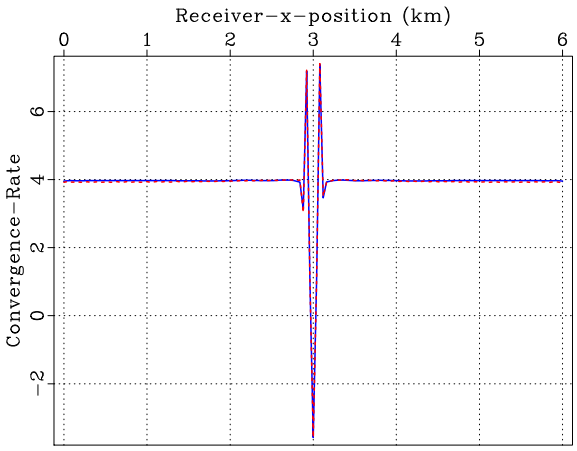

(b) $\mathbf{s} = (0, 1)$ case

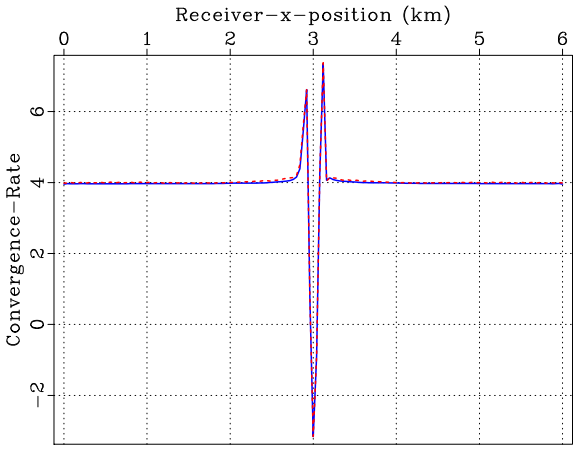

(c) $\mathbf{s} = (0, 2)$ case

Figure 4.7 : Approximate convergence rates of finite difference solutions to 2-D acoustics (pressure data only) using 2-4 scheme and fourth-order source approximation for scalar multipole of type $f(\mathbf{x}, t) = w_1(t)D^{\mathbf{s}}\delta(\mathbf{x} - \mathbf{x}^*)$. Rates computed using L^2 (solid blue) and L^∞ ($--$ red) norms.

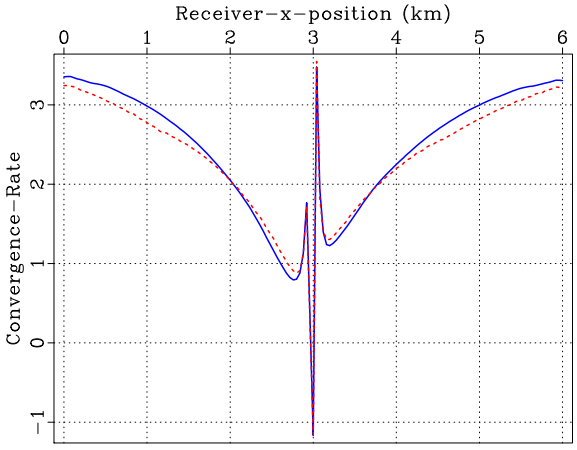

(a) $\mathbf{s} = (0, 0)$ case

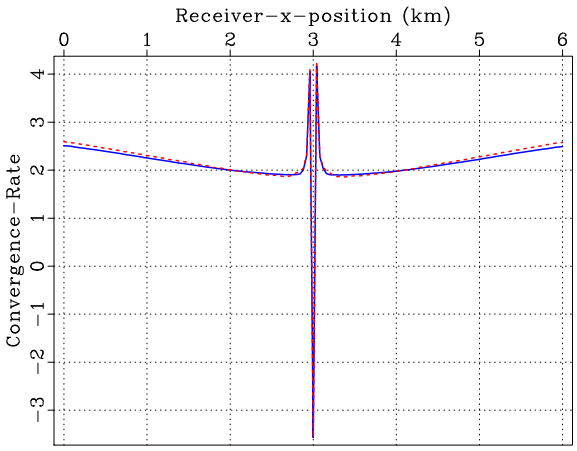

(b) $\mathbf{s} = (0, 1)$ case

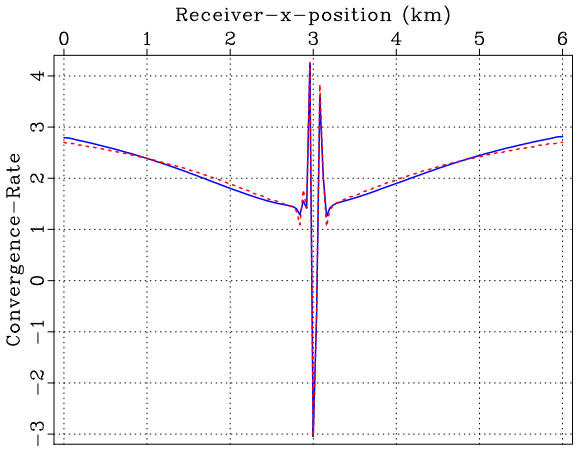

(c) $\mathbf{s} = (0, 2)$ case

Figure 4.8 : Approximate convergence rates of finite difference solutions to 2-D acoustics (pressure data only) using 2-4 scheme and second-order source approximation for scalar multipole of type $f(\mathbf{x}, t) = w_1(t) D^{\mathbf{s}} \delta(\mathbf{x} - \mathbf{x}^*)$. Rates computed using L^2 (solid blue) and L^∞ ($--$ red) norms.

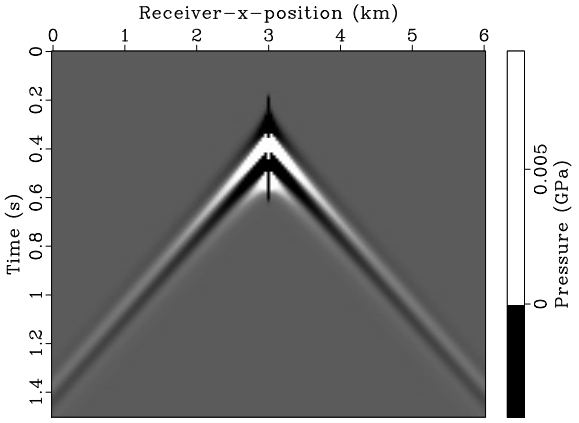

(a) $\mathbf{s} = (0, 0, 0)$ case

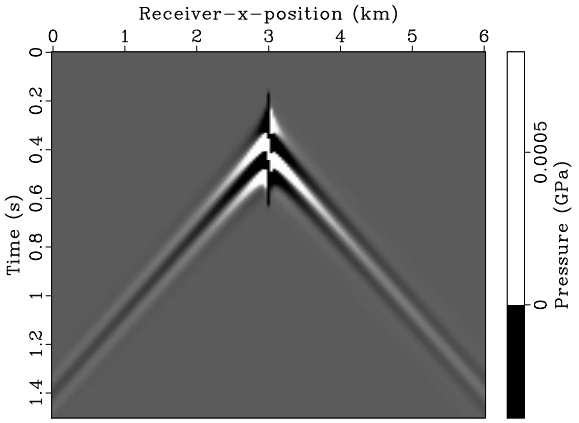

(b) $\mathbf{s} = (0, 1, 0)$ case

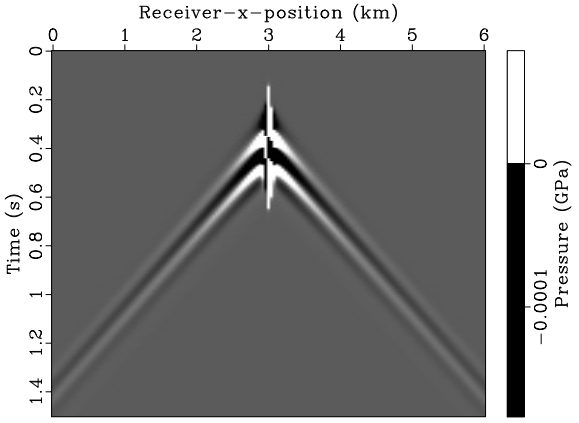

(c) $\mathbf{s} = (0, 2, 0)$ case

Figure 4.9 : Pressure field traces (3-D acoustics) using 2-4 finite difference scheme (with $h = 10m$ and $\Delta t = 0.5ms$) and fourth-order source approximation for scalar multipole of type $f(\mathbf{x}, t) = w_1(t) D^{\mathbf{s}} \delta(\mathbf{x} - \mathbf{x}^*)$.

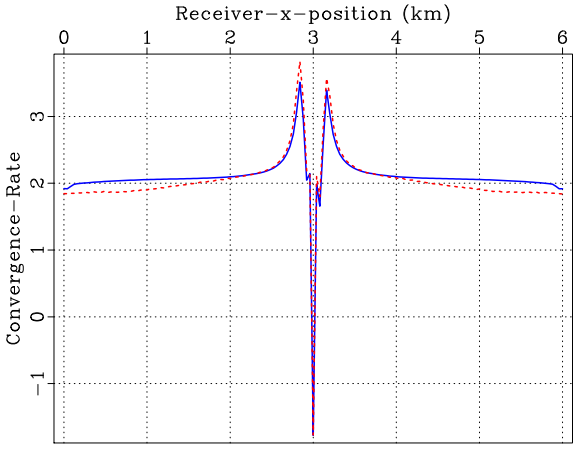

(a) $\mathbf{s} = (0, 0, 0)$ case

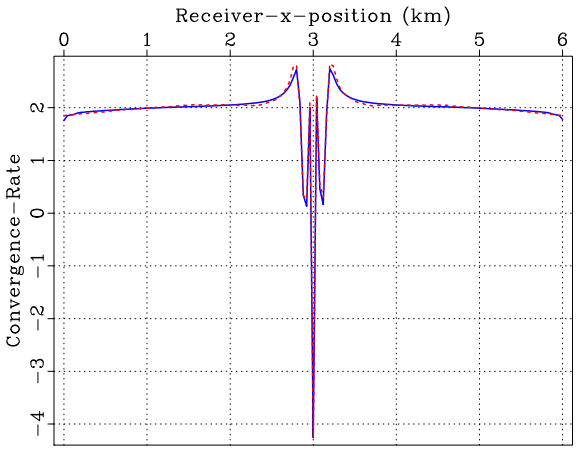

(b) $\mathbf{s} = (0, 1, 0)$ case

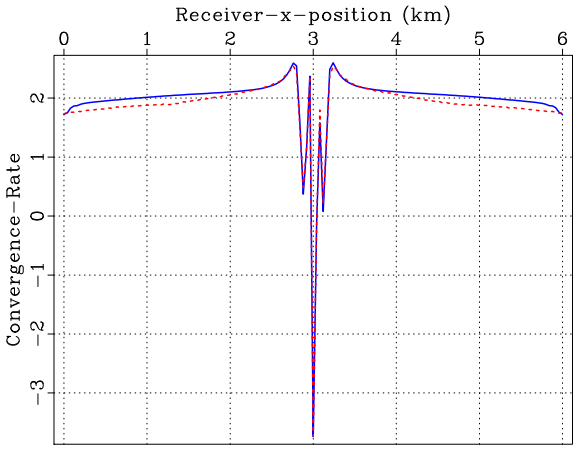

(c) $\mathbf{s} = (0, 2, 0)$ case

Figure 4.10 : Approximate convergence rates of finite difference solutions to 3-D acoustics (pressure data only) using 2-2 scheme and second-order source approximation for scalar multipole of type $f(\mathbf{x}, t) = w_1(t)D^{\mathbf{s}}\delta(\mathbf{x} - \mathbf{x}^*)$. Rates computed using L^2 (solid blue) and L^∞ ($--$ red) norms.

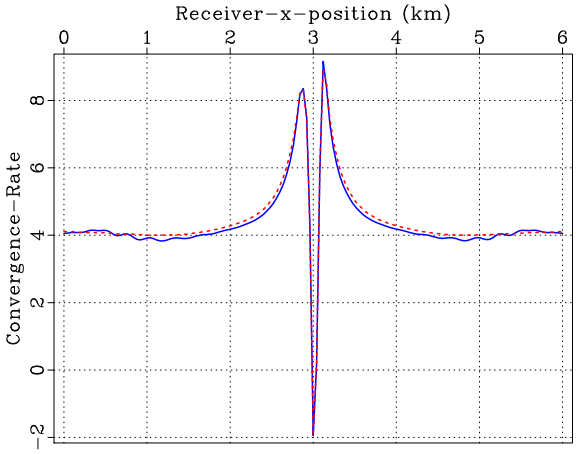

(a) $\mathbf{s} = (0, 0, 0)$ case

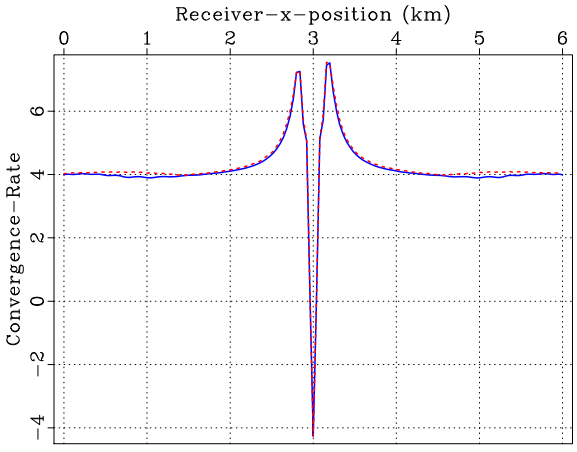

(b) $\mathbf{s} = (0, 1, 0)$ case

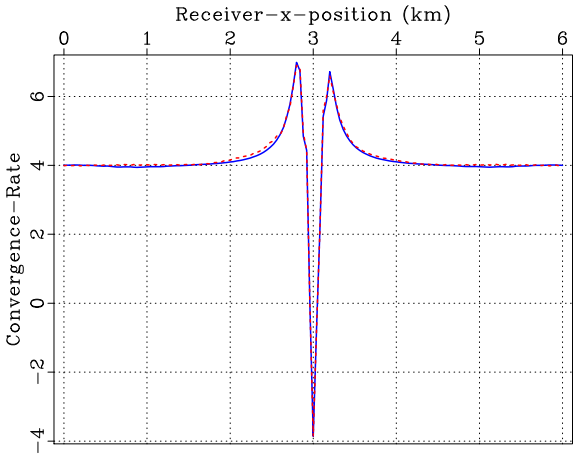

(c) $\mathbf{s} = (0, 2, 0)$ case

Figure 4.11 : Approximate convergence rates of finite difference solutions to 3-D acoustics (pressure data only) using 2-4 scheme and fourth-order source approximation for scalar multipole of type $f(\mathbf{x}, t) = w_1(t)D^{\mathbf{s}}\delta(\mathbf{x} - \mathbf{x}^*)$. Rates computed using L^2 (solid blue) and L^∞ ($--$ red) norms.

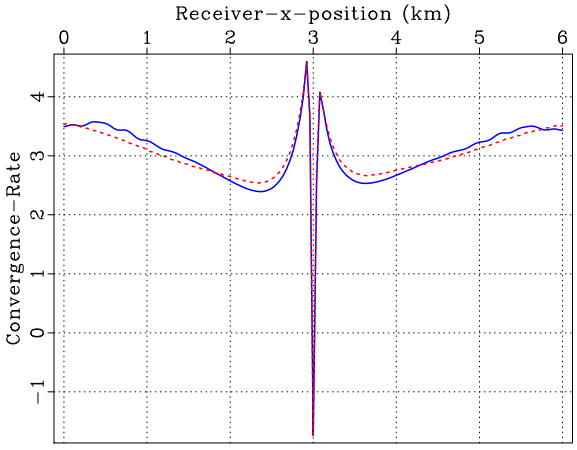

(a) $\mathbf{s} = (0, 0, 0)$ case

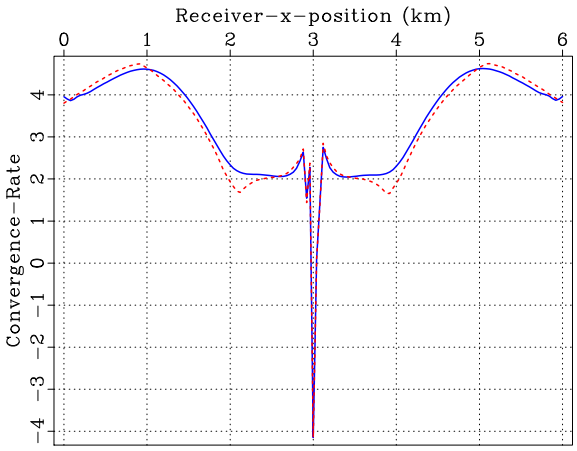

(b) $\mathbf{s} = (0, 1, 0)$ case

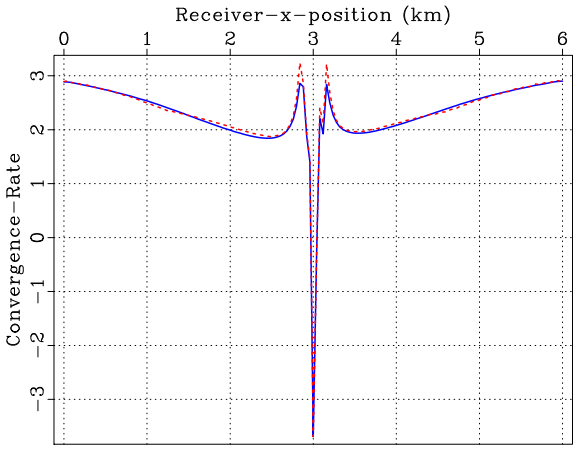

(c) $\mathbf{s} = (0, 2, 0)$ case

Figure 4.12 : Approximate convergence rates of finite difference solutions to 3-D acoustics (pressure data only) using 2-4 scheme and second-order source approximation for scalar multipole of type $f(\mathbf{x}, t) = w_1(t)D^{\mathbf{s}}\delta(\mathbf{x} - \mathbf{x}^*)$. Rates computed using L^2 (solid blue) and L^∞ ($--$ red) norms.

Discussion

Numerical results presented here validate the effectiveness of the moment condition 3.4 for controlling the propagation of finite difference truncation error for multipole sources.

Spatial convergence rates of second and fourth order finite difference methods are preserved when the moment conditions are satisfied. Moreover, the observed region of optimal order convergence is also roughly as predicted. For example the results from figure 4.7c where $D^{\mathbf{s}}\delta(\mathbf{x}-\mathbf{x}^*)$ with $|\mathbf{s}| = 2$ is replaced by a fourth order approximation in 2-D; the source stencil had a diameter of about $q + |\mathbf{s}| = 6$ traces, equivalent to 6 grid points in the x_2-direction for the coarsest $(40m)$ mesh.

As mentioned in the introduction of this chapter, current literature fails to provide analysis directly applicable to the solution of acoustodynamics (equations 2.4) or elastodynamics (equations 2.5) with multipole sources. The most complete account, as far as I am aware, of the analysis of approximations to PDEs with singular sources is given by Hosseini et al. (2016) in the context of regularizations of the delta distribution. Hosseini et al. developed a unified framework for analyzing approximation errors that can be readily applied to any numerical scheme. Their work in particular addressed two fundamental questions: (i) What form of convergence should be used to examine $f^h \to f$? That is, how does our source approximations converge to multipoles as distributions? (ii) What form of convergence should be used to examine $u^h \to u$, convergence of numerical solution u^h with source approximation f^h to

true solution u with source f? Authors showed that convergence of $f^h \to f$ in the distribution sense (weak-* topology), and in some weighted Sobolev norm, can be achieved at a desired rate if a set of *continuous moment conditions* are satisfied by the approximation f^h, analogous to the discrete moment conditions discussed here. Furthermore, they discussed answers to question (ii) and the interplay of approximation f^h with the convergence of $u^h \to u$ for prototypical elliptic and hyperbolic PDEs.

Numerical results presented here help motivate the use of approximations to multipoles developed in chapter 3. Moreover, I believe it is possible to provide a formal error analysis of my conjecture as discussed in section 4.2. This would entail analyzing the interplay of approximations f^h with the convergence of $u^h \to u$ for the particular choice of PDEs and numerical schemes considered here.

The RVL-based structure of my MPS framework does not really get a solid workout in this study. Inspection of the code and scripts shows that the framework is a convenient environment for implementing the numerical examples presented in the last section. However the capabilities of this mode of code organization emerge much more clearly in inversion applications. For example, it will be shown in the next chapter that a choice of norm in an MPS space, that reflects the effect of the spatial delta derivatives on temporal frequency, can dramatically accelerate the convergence of source recovery by Krylov subspace iteration. For this it was only necessary to pass the `RVL::LinOpValOp` representing the MPS-to-data trace map, and an

`RVL:LinearOp` representing the Gram operator of the norm, to an RVL implementation of the preconditioned conjugate gradient method, used completely without alteration. It will also be possible to incorporate the MPS based operator into the RVL implementation of variable projection method (Rickett, 2013) for joint source-medium inversion without any change either to the MPS code or to the RVL variable projection algorithm.

Conclusion

In this paper I have presented a computational framework for representing multipole sources as linear combinations of multipole bases as discussed in chapter 2. In particular, I implemented the singular source approximation developed in chapter 3 as a linear map from MPS-to-RHS source terms. Mathematical constructs of the MPS space and the MPS-to-RHS map were realized using RVL and pipelined into finite difference solvers via IWave. Numerical results validate the correctness of my implementation by reproducing conjectures related to the singular source approximation, namely achieving optimal convergence rates when using a proper source approximation.

Chapter 5

Multipole Source Inversion

5.1 Introduction

In this chapter I focus on the source estimation subproblem, that is recovering source time-dependencies via *full waveform inversion (FWI)* under the assumption that medium parameters are known. Inversion of multipole sources, in particular, pose challenges stemming from ill-conditioning of the source-to-data map. In the context of seismic moment tensors (related to multipoles in elasticity), most attempts at regularization have aimed to improve condition number of the source-to-data map by optimizing data coverage, as well as constraining or oversimplifying the source representation; see Eaton and Forouhideh (2010) and Song and Toksöz (2011) for examples of moment tensor inversions from microseismic data.

Work by Koch (1991) applies a Tikhonov regularization approach, essentially introducing a damping term in the underlying linear least squares problem. Their numerical results indeed demonstrate the benefits of this method, especially in cases where data acquisition geometry results in known ill-conditioning. Furthermore, Koch illustrated robustness of their results against errors in time lag of source parameters, medium parameters, and extended sources (non-point sources). The dampening pa-

rameter in the methodology described above is chosen in a trial by error manner given information about the singular value decomposition of the source-to-data map which is impractical for larger problems (e.g., exploration seismology).

The approach I develop in this chapter seeks to better condition the multipole source inversion problem from a more fundamental angle: redefine the domain space of the source-to-data map to yield a better bounded operator, thus improving the condition number associated with solving the normal equations that result from a least squares formulation. Specifically, I propose a preconditioner for the normal equations related to a redefined domain inner-product weighted by fractional derivative/integral operators.

In the following sections, I formally state the source-to-data map (and its adjoint) formulated as a multichannel convolution, define the multipole source inversion problem via FWI, and derive my proposed preconditioners. The numerical results section demonstrates the effectiveness of my preconditioners in accelerating convergence of the *conjugate gradient* (CG) algorithm applied to some synthetic examples. The preconditioning approach I present here, along with numerical experiments, is formulated for acoustics (system 2.4) with pressure source terms (scalar multipoles) and pressure data only. Similar analysis and results can easily extended to other types of data and sources. Moreover, an analogous preconditioning strategy for the elasticity case is possible and is the subject of future research.

5.2 Multipole Source Estimation via FWI

The previous chapter introduced the discrete model-to-data map (equation 4.8) in the context of IWave and my multipole source framework. I use similar notation here to denote the *forward map* irrespective of discretization, that is a mapping from model (medium and source) parameters to data. Note that the model-to-data map in equation 4.8 is with respect to right-hand side sources. Employing the source presentation sketched in chapter 2, I define the forward map here over MPS coefficients which can be derived by operator composition of MPS-to-RHS map with the right-hand side source -to- data map as suggested by equation 4.9.

The forward map $F : \mathfrak{M} \times \mathfrak{W} \to \mathfrak{D}$ is defined as a mapping from medium parameter space $\mathfrak{M}$ and MPS space $\mathfrak{W}$ to data space $\mathfrak{D}$. Thus,

$$F[m, w] = d,$$

with medium parameter vector $m = (\kappa, \beta)$ in particular for the acoustic equations in first order form, and MPS coefficient vector $w \in \mathfrak{W}$. For the cases considered here the data vector will consist of pressure data sampled at receiver points $\{\mathbf{x}_{i_r}\}_{i_r=0}^{N_r}$ over time interval $[0, T]$. I define natural L^2 inner-products for MPS and data spaces as follows,

$$\langle w^{(1)}, w^{(2)} \rangle_{\mathfrak{W}} := \sum_i \int_0^T dt \; w_i^{(1)}(t) \; w_i^{(2)}(t), \tag{5.1}$$

$$\langle d^{(1)}, d^{(2)} \rangle_{\mathfrak{D}} := \sum_{i_r=0}^{N_r} \int_0^T dt\; p^{(1)}(\mathbf{x}_{i_r}, t)\; p^{(2)}(\mathbf{x}_{i_r}, t). \tag{5.2}$$

Consider the forward map F with given model parameter vector m and MPS coefficient vector w corresponding to an MPS space that spans scalar multipoles of the form $f(\mathbf{x}, t) = \sum_i w_i(t) b_i(\mathbf{x})$ for some specified multipole basis and given source location. Let $G_i(\mathbf{x}, t)$ denote the pressure field from acoustic system 2.4 with impulsive source $\delta(t) b_i(\mathbf{x})$. Then it follows that $F[m, w]$ can be written as a *multichannel convolution* with the G_i Green's functions,

$$F[m, w] = \left\{ p(\mathbf{x}_{i_r}, t) = \sum_i \int d\tau\; G_i(\mathbf{x}_{i_r}, t - \tau)\; w_i(\tau) : i_r = 0, 1, ..., N_r \right\}.$$

Note that Green's functions are implicitly dependent on medium parameters and source location. For a given medium parameter vector m, the forward map is denoted as a linear operator from MPS space -to- data space by $F[m] : \mathfrak{W} \to \mathfrak{D}$, i.e.,

$$F[m]w = d.$$

Moreover, with inner-products for data space and MPS space as defined above, it can be shown that the adjoint of the linear map $F[m]$, denoted by $F[m]^T : \mathfrak{D} \to \mathfrak{W}$, coincides with *multichannel cross-correlation* with Green's functions,

$$F[m]^T d = w \quad \text{with} \quad w_i(t) = \sum_{i_r=0}^{N_r} \int d\tau\; G_i(\mathbf{x}_{i_r}, \tau - t) p(\mathbf{x}_{i_r}, \tau).$$

The multipole source estimation FWI problem consists of finding w^* that minimizes the error between observed data d_{obs} and predicted data in a least squares sense:

$$w^* = \underset{w \in \mathfrak{W}}{\operatorname{argmin}} \|F[m]w - d_{obs}\|_{\mathfrak{D}}^2, \tag{5.3}$$

where $\|\cdot\|_{\mathfrak{D}}$ is the norm induced by the data space inner product. Solution to equation 5.3 is given by the solution to the normal equations,

$$F[m]^T F[m]w = F[m]^T d_{obs}. \tag{5.4}$$

Adjoint computations, that is applications of $F[m]^T$, can be formulated as solving a PDE problem as is typically done for the adjoint state method when computing gradients of PDE constrained optimization problems. However, given the special form of the forward map from MPS coefficients -to- data it follows that computations of the form $F^T[m]d$ can be carried out by something cheaper than a PDE solve. As I have mentioned above, the forward map is equivalent to multi-channel convolution while the adjoint corresponds to multichannel cross-correlation, with an appropriate set of Green's functions. Thus, for a given medium parameter vector m, the forward and adjoint action of $F[m]$ can be computed at a one time cost of N PDE solves (assuming there are N Green's functions to compute) and an additional cost of a multichannel convolution/cross-correlation for each application of the operator. This strategy for computing matrix-vector multiplication with $F[m]$ and $F[m]^T$ will prove

vital in keeping the computational cost of the source inversion problem reasonable in particular when using iterative solvers as done in this chapter and for joint inversions in 3-D.

5.3 Preconditioners

The approach developed here seeks to better condition the multipole surce inversion problem by redefining the domain space $\mathfrak{W}$ to yield a better bounded linear operator $F[m]$, thus improving the condition number associated with solving the normal equations 5.4. MPS space $\mathfrak{W}$ is redefined by replacing its native inner-product $\langle \cdot, \cdot \rangle_{\mathfrak{W}}$ by a weighted one denoted by $\langle \cdot, \cdot \rangle_{\mathfrak{W}'}$,

$$\langle w^{(1)}, w^{(2)} \rangle_{\mathfrak{W}'} := \langle Qw^{(1)}, Qw^{(2)} \rangle_{\mathfrak{W}} = \langle w^{(1)}, Q^T Q w^{(2)} \rangle_{\mathfrak{W}}.$$

Weight operator Q consists of a diagonal operator with respect to MPS coefficients,

$$Qw = \mathrm{diag}(Q_1 w_1, Q_2 w_2, ...),$$

for some linear operators $\{Q_i\}$. Note that the adjoint of $F[m]$ with respect to the weighted inner-product $\langle \cdot, \cdot \rangle_{\mathfrak{W}'}$ can be expressed in terms of $F[m]^T$, namely

$$F[m]^T \rightarrow (Q^T Q)^{-1} F[m]^T.$$

Thus the least squares solution in the weighted inner-product is given by

$$MF[m]^T F[m]w = MF[m]^T d_{obs}, \tag{5.5}$$

where the original normal equations have been effectively preconditioned by operator $M = (Q^T Q)^{-1}$.

Based on the discussion of analytical solutions for the acoustic wave equation with multipole sources, see appendix B, I choose $\{Q_i\}$ to be fractional time derivative/integral operator scaled by wave speed $c = \sqrt{\beta\kappa}$,

$$Q_i = \frac{1}{c^{|b_i|}} \left(\frac{d}{dt}\right)^{a_0+|b_i|}, \tag{5.6}$$

with $|b_i| \geq 0$ denoting the derivative order related to MPS basis term b_i, that is the maximum number of spatial derivatives in the MPS basis. The scalar a_0 is dependent on the spatial dimension and choice of PDE system and is allowed to take fractional values. For the acoustic system 2.4 in 1-D, 2-D, and 3-D, $a_0 = 0, 1/2, 1$ respectively. As an example, consider the scalar MPS space of order one in 2-D spanned by the MPS basis

$$b_1(\mathbf{x}) = \delta(\mathbf{x} - \mathbf{x}^*), \quad b_2(\mathbf{x}) = \frac{\partial}{\partial x_1}\delta(\mathbf{x} - \mathbf{x}^*), \quad b_3(\mathbf{x}) = \frac{\partial}{\partial x_2}\delta(\mathbf{x} - \mathbf{x}^*),$$

for the first order acoustic equations ($a_0 = 1/2$). Then,

$$|b_1| = 0, \quad |b_2| = |b_3| = 1,$$

and moreover,

$$Q_1 = \left(\frac{d}{dt}\right)^{1/2}, \quad Q_2 = Q_3 = \frac{1}{c}\left(\frac{d}{dt}\right)^{3/2}.$$

Similarly, for the scalar MPS space of order one in 3-D spanned by MPS basis given in equation 2.8,

$$|b_1| = 0, \quad |b_2| = 1, \quad |b_3| = 1, \quad |b_4| = 1,$$

hence

$$Q_1 = \left(\frac{d}{dt}\right)^{1}, \quad Q_2 = Q_3 = Q_4 = \frac{1}{c}\left(\frac{d}{dt}\right)^{2}.$$

Note that this is slightly different from what would be expected given equations B.4, B.6, and B.5. Recall that analytical solutions compiled in table B.1 are derived for the acoustic wave equation, that is the second order formulation. Moreover, scalar multipole sources from the first order system can be related to source terms of the second order system by an extra time derivative.

Preconditioner $M = (Q^T Q)^{-1}$ will required adjoints and inverses of potentially fractional derivative or integral operators. Assuming the MPS coefficients (and its derivatives) are causal, fractional integrals will coincide with the inverse of fractional derivatives. The numerical approach and implementation of fractional derivative/integral operators considered here is briefly discussed in appendix C.

5.4 Numerical Experiments

In this section, I present some source inversion results illustrating the better-conditioning of normal equations (equation 5.4) when using my proposed preconditioning strategy. In particular, I solve the normal equations iteratively via a standard *conjugate gradient for normal equations* (CGNE) algorithm, with preconditioner $M = (Q^T Q)^{-1}$ as suggested in the previous section. This is to be contrasted with previous work on moment tensor inversion in which direct solvers are preferred given the manageable size of the underlying linear system. Direct solvers are indeed the tools to use when the problem is posed in the frequency domain or when simplifying assumptions on the source lead to tractable linear systems. However, problems related to exploration seismology, as oppose to earthquake seismology, are quite large due to the number of receivers typical in these applications, thus motivating the use of iterative solvers.

The multipole source (representation and inversion) framework has been implemented as part of IWave and RVL as discussed in chapter 4. Results in this chapter pertain to the acoustic system in first-order form (equation 2.4) with scalar multipole sources with a specified basis. The underlying PDE solver used here is again the 2-4 staggered grid finite difference scheme. As alluded to earlier, the forward/adjoint action of the linear operator $F[m]$ is implemented as a multichannel convolution/cross-correlation of MPS coefficients with appropriate Green's functions, thus avoiding further PDE solves during the CGNE algorithm.

The following are stopping criteria specifications for CGNE used throughout source inversions:

- sufficient reduction in residual,

$$\|F[m]w - d_{\text{obs}}\|_{\mathfrak{D}} \leq 10^{-4} \times \|d_{\text{obs}}\|_{\mathfrak{D}}$$

- sufficient reduction in gradient (normal residual),

$$\|F[m]^T F[m]w - F[m]^T d_{\text{obs}}\|_{\mathfrak{W}} \leq 10^{-4} \times \|F[m]^T d_{\text{obs}}\|_{\mathfrak{W}}$$

- or maximum number of iterations = 150.

Single Multipole in Homogeneous Medium

The first set of numerical experiments I present involve estimating single scalar multipole terms of the form

$$f(\mathbf{x}, t) = w_1(t) b_1(\mathbf{x}), \quad \text{where} \quad b_1(\mathbf{x}) = D^{\mathbf{s}} \delta(\mathbf{x} - \mathbf{x}^*)$$

for multi-index $\mathbf{s} = (0,0), (0,1)$ in 2-D and $\mathbf{s} = (0,0,0), (0,1,0)$ in 3-D. MPS coefficient w_1 is chosen to be a $10Hz$ peak frequency Ricker wavelet as shown in figure 5.1a. The acoustic medium is homogeneous and simulated to be "unbounded" with the use of PMLs. Figures 5.2a and 5.2b elaborate on source-receiver geometry used

throughout these tests. Other test specifications include:

- total recording time $T = 1.0s$;
- spatial grid sizes $h = 20m$;
- simulation time step $\Delta t = 2ms$

For given the Ricker wavelet, a grid size of $20m$ results in 15 *grid points per wavelength* (gpw) at peak frequency and 5 gpw at $30Hz$; I refer to figure 5.1d regarding the aforementioned frequency considerations.

Observed data, in the form of pressure field time traces, is plotted in figure 5.3 for 2-D and 3-D and the various choices of multi-index $\mathbf{s}$. MPS coefficient w_1 is estimated using CGNE with and without preconditioner $M = (Q^T Q)^{-1}$ as suggested by equation 5.6. In particular,

$$Q_1 = \left(\frac{d}{dt}\right)^{1/2+|\mathbf{s}|}, \quad \text{in 2-D ,}$$

$$Q_1 = \left(\frac{d}{dt}\right)^{1+|\mathbf{s}|}, \quad \text{in 3-D .}$$

Estimated w_1 is plotted along with the true solution in figure 5.4. Inversions with and without preconditioning give accurate results for the most part, with the exception of the 3-D test case with $\mathbf{s} = (0, 1, 0)$ where estimated MPS coefficient without preconditioning exhibits visible errors. Figure 5.5 plots the log of the norm of the residual and gradient (or normal residual), with respect to the L^2-norms defined on

the data and MPS spaces respectively, versus CGNE iterate. In all cases, a dramatic acceleration in convergence is observed when applying my preconditioner, even in cases where the non-preconditioned CGNE iterates did not converge (i.e., achieve sufficient reduction of residual or gradient) after 150 iterations.

Results are summarized in table 5.1, containing the reduction in data residual

$$\frac{\|F[m]w - d_{\text{obs}}\|_{\mathfrak{D}}}{\|d_{\text{obs}}\|_{\mathfrak{D}}},$$

reduction in gradient (or normal residual)

$$\frac{\|F[m]^T F[m]w - F[m]^T d_{\text{obs}}\|_{\mathfrak{W}}}{\|F[m]^T d_{\text{obs}}\|_{\mathfrak{W}}}$$

and reduction in errors between true and estimated MPS coefficients in the L^2- and weighted L^2-norms, that is $\|\cdot\|_{\mathfrak{W}}$ and $\|\cdot\|_{\mathfrak{W}'}$ respectively, namely

$$\frac{\|w - w_{\text{true}}\|_{\mathfrak{W}}}{\|w_{\text{true}}\|_{\mathfrak{W}}} \quad \text{and} \quad \frac{\|w - w_{\text{true}}\|_{\mathfrak{W}'}}{\|w_{\text{true}}\|_{\mathfrak{W}'}}.$$

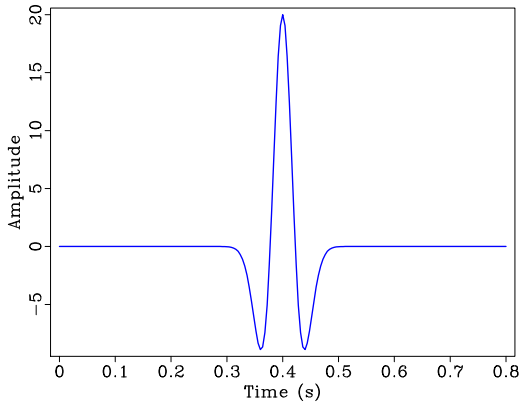

(a) Time trace of Ricker wavelet.

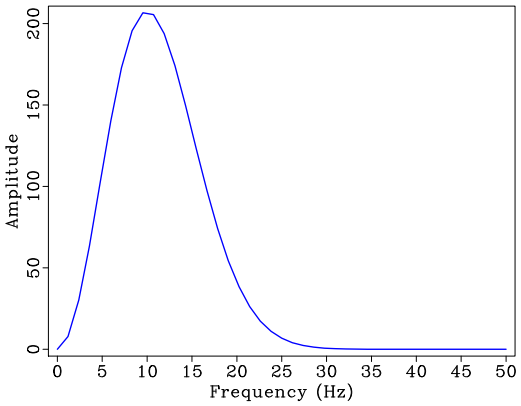

(b) Frequency spectrum of Ricker wavelet.

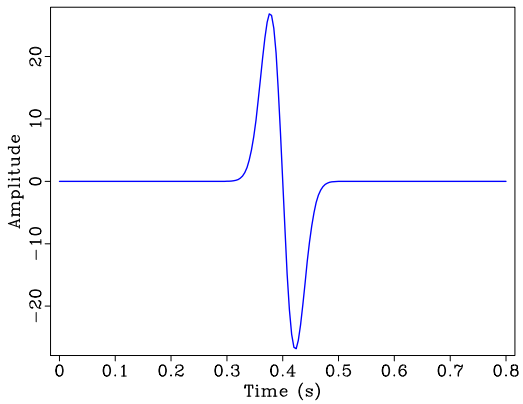

(c) Time trace of Gaussian derivative wavelet.

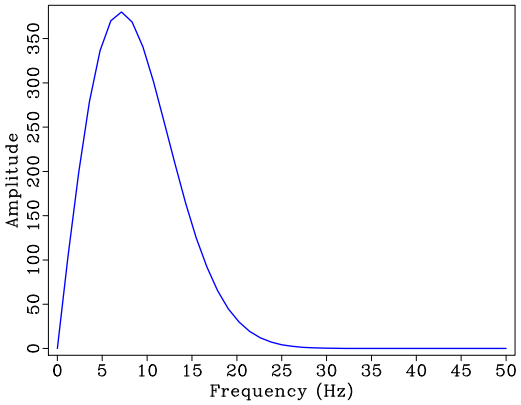

(d) Frequency spectrum of Gaussian derivative wavelet.

Figure 5.1 : Time trace and frequency spectrum of $10Hz$ peak frequency Ricker and derivative of Gaussian wavelet.

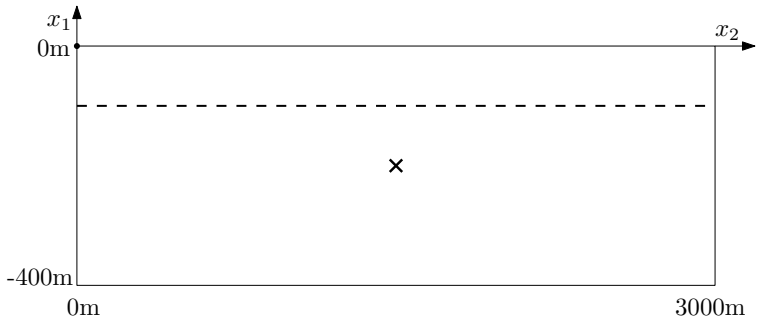

(a) 2-D homogeneous model case with receiver positions $\mathbf{x}_{i_r} = (-100m, 0m : 20m : 3000m)$ and source position $\mathbf{x}^* = (-203m, 1503m)$.

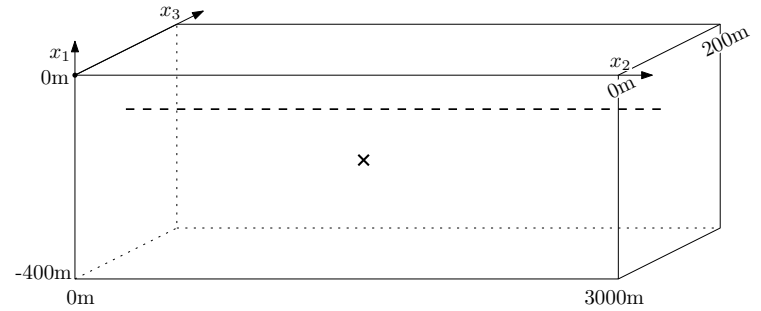

(b) 3-D homogeneous model case with receiver positions $\mathbf{x}_{i_r} = (-100m, 0m : 20m : 3000m, 100m)$ and source position $\mathbf{x}^* = (-203m, 1503m, 103m)$.

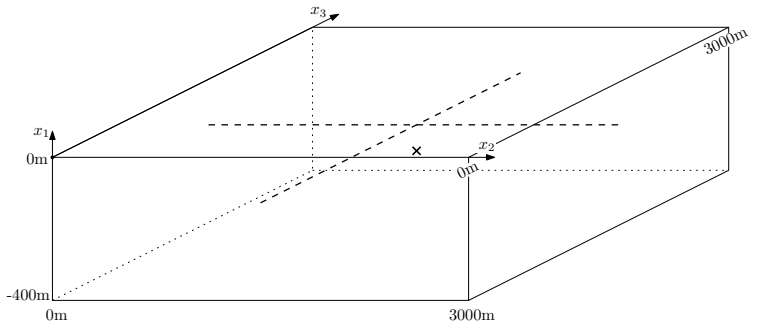

(c) 3-D homogeneous model case with first line of receivers $\mathbf{x}_{i_r} = (-100m, 0m : 20m : 3000m, 1500m)$, second line of receivers $\mathbf{x}_{i_r} = (-100m, 1500m, 0m : 20m : 3000m)$, and source position $\mathbf{x}^* = (-203m, 1503m, 1503m)$.

Figure 5.2 : Medium and source-receiver geometry specifications for 2-D and 3-D source inversion test with homogeneous medium parameters, constant density ($1kg/m^3$) and velocity ($3km/s$). Receivers and source depicted by dashed lines and a crosses respectively.

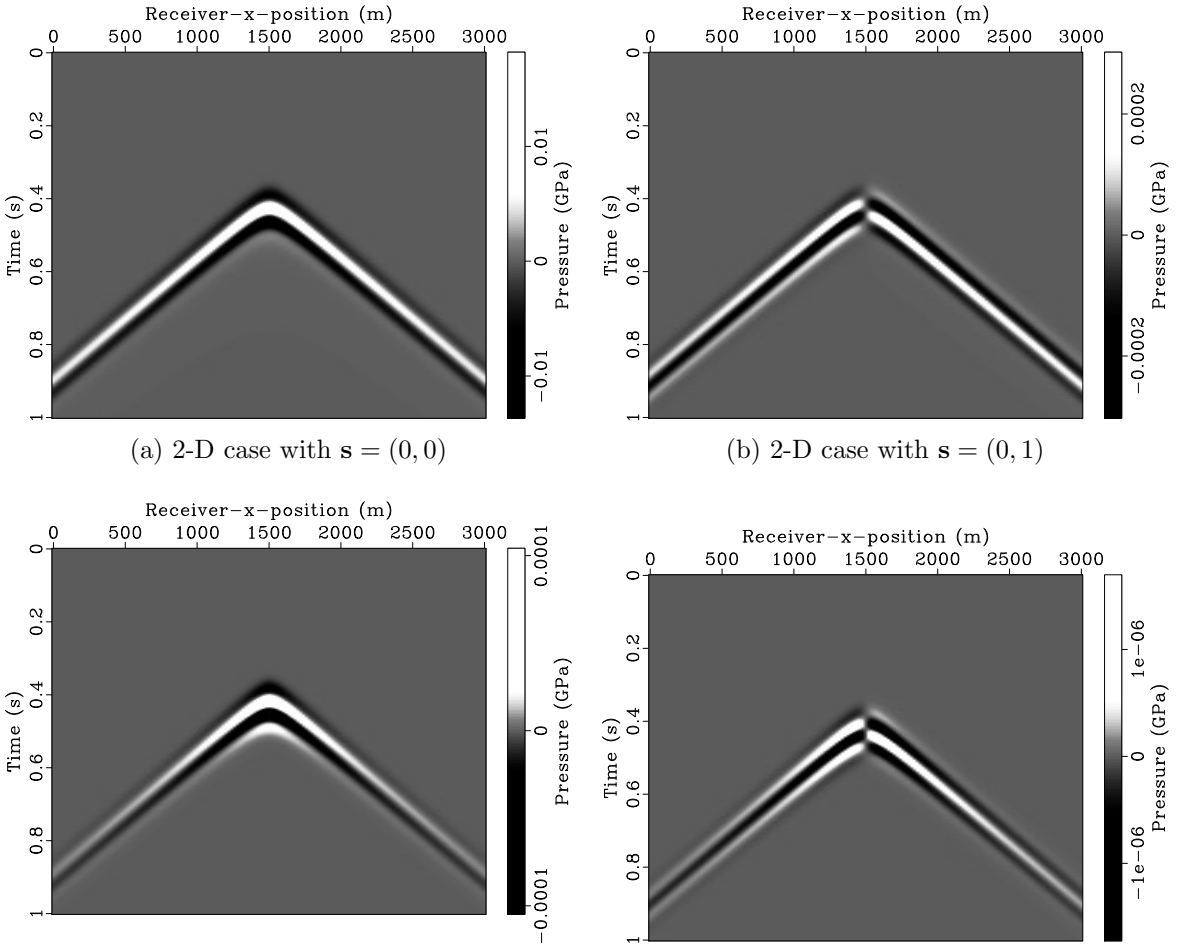

(a) 2-D case with $\mathbf{s} = (0, 0)$

(b) 2-D case with $\mathbf{s} = (0, 1)$

(c) 3-D case with $\mathbf{s} = (0, 0, 0)$

(d) 3-D case with $\mathbf{s} = (0, 1, 0)$

Figure 5.3 : Pressure time traces used as "observed data" in source inversions of the type $f(\mathbf{x}, t) = w_1(t)D^{\mathbf{s}}\delta(\mathbf{x} - \mathbf{x}^*)$ in 2-D and 3-D. Homogeneous unbounded model test case.

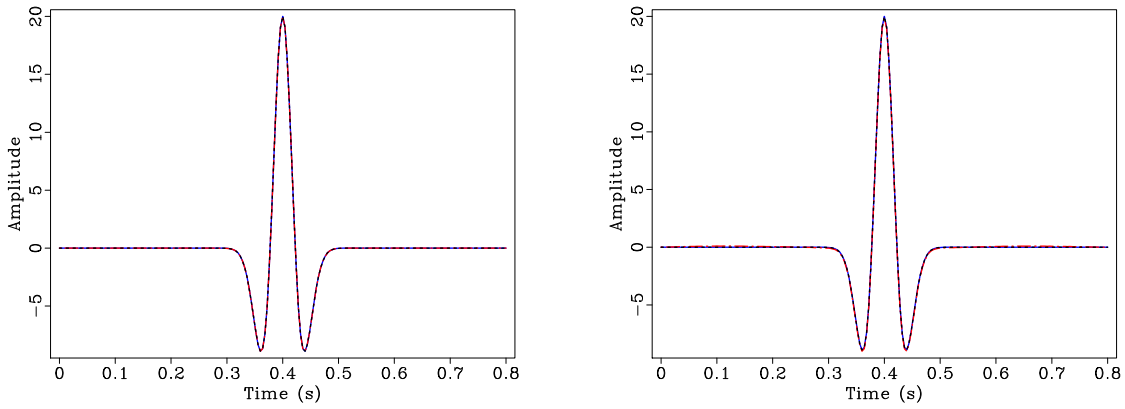

(a) 2-D case with $\mathbf{s} = (0, 0)$

(b) 2-D case with $\mathbf{s} = (0, 1)$

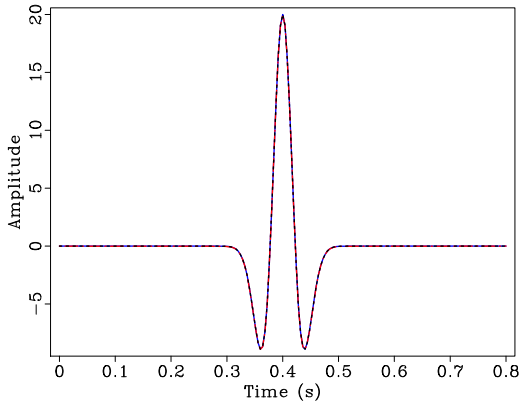

(c) 3-D case with $\mathbf{s} = (0, 0, 0)$

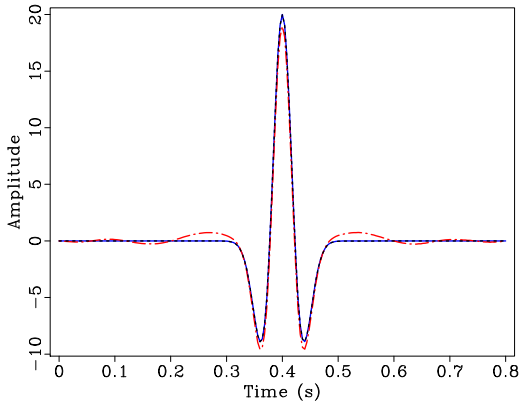

(d) 3-D case with $\mathbf{s} = (0, 1, 0)$

Figure 5.4 : Estimated MPS coefficient w_1 for scalar multipoles of type $f(\mathbf{x}, t) = w_1(t)D^{\mathbf{s}}\delta(\mathbf{x} - \mathbf{x}^*)$ in 2-D and 3-D. True solution (solid blue) and estimated solution via CGNE with ($--$ black) and without ($-\cdot-$ red) preconditioning.

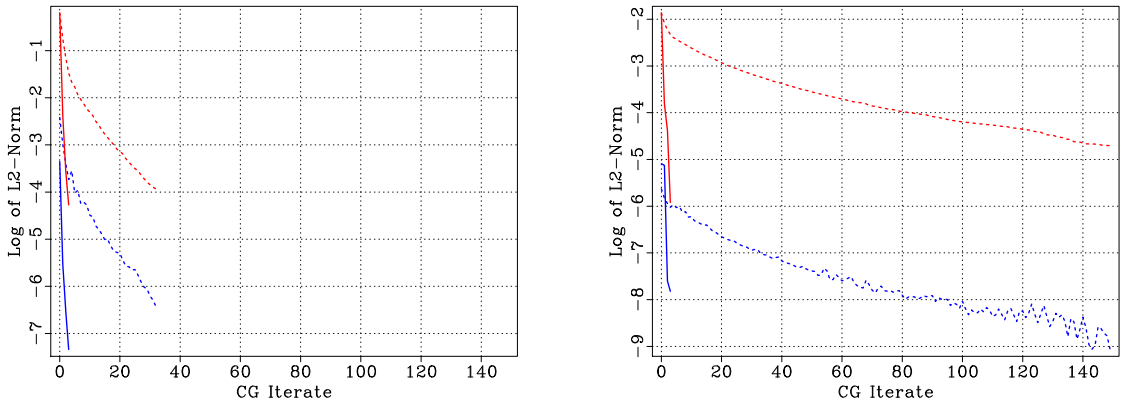

(a) 2-D case with $\mathbf{s} = (0, 0)$

(b) 2-D case with $\mathbf{s} = (0, 1)$

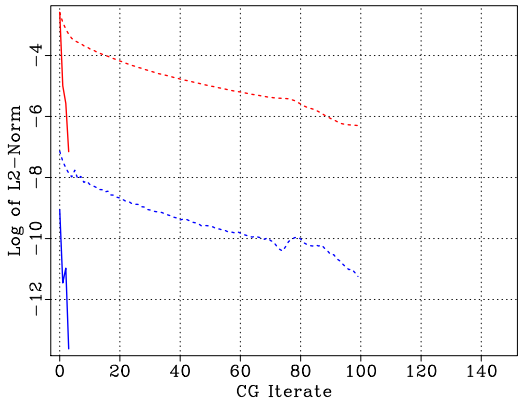

(c) 3-D case with $\mathbf{s} = (0, 0, 0)$

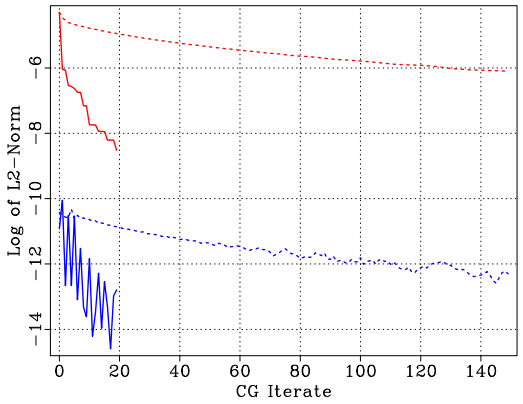

(d) 3-D case with $\mathbf{s} = (0, 1, 0)$

Figure 5.5 : CGNE convergence plots for source estimation of scalar multipoles of type $f(\mathbf{x}, t) = w_1(t)D^{\mathbf{s}}\delta(\mathbf{x} - \mathbf{x}^*)$ in 2-D and 3-D test cases. Log of L^2-norms (in data and MPS space resp.) of residuals (red/top) and gradients (blue/bottom) plotted for CGNE iterates with (solid) and without $(--)$ preconditioning.

Mixed MPS in Homogeneous Medium

The next set of numerical experiments involve estimating scalar multipole terms of the form

$$f(\mathbf{x},t) = w_1(t)b_1(\mathbf{x}) + w_2(t)b_2(\mathbf{x}) + w_3(t)b_3(\mathbf{x}),$$

with

$$b_1(\mathbf{x}) = \delta(\mathbf{x}-\mathbf{x}^*), \quad b_2(\mathbf{x}) = \frac{\partial}{\partial x_1}\delta(\mathbf{x}-\mathbf{x}^*), \quad b_3(\mathbf{x}) = \frac{\partial}{\partial x_2}\delta(\mathbf{x}-\mathbf{x}^*), \tag{5.7}$$

in 2-D, and in 3-D,

$$f(\mathbf{x},t) = w_1(t)b_1(\mathbf{x}) + w_2(t)b_2(\mathbf{x}) + w_3(t)b_3(\mathbf{x}) + w_4(t)b_4(\mathbf{x}),$$

with

$$\begin{aligned} b_1(\mathbf{x}) &= \delta(\mathbf{x}-\mathbf{x}^*), & b_2(\mathbf{x}) &= \frac{\partial}{\partial x_1}\delta(\mathbf{x}-\mathbf{x}^*), \\ b_3(\mathbf{x}) &= \frac{\partial}{\partial x_2}\delta(\mathbf{x}-\mathbf{x}^*), & b_4(\mathbf{x}) &= \frac{\partial}{\partial x_3}\delta(\mathbf{x}-\mathbf{x}^*). \end{aligned} \tag{5.8}$$

The true MPS coefficients w_1, w_4 are set to zero and w_1, w_2 are given by a Ricker and derivative of Gaussian wavelet at peak frequency of $10Hz$ respectively; see figure 5.1. Experimental setup and simulation parameters are identical to the previous set of tests. Observed data is plotted in figure 5.6 for 2-D and 3-D.

MPS coefficients are estimated using CGNE with and without preconditioning, where

$$Q_1 = \left(\frac{d}{dt}\right)^{1/2},\ Q_2 = Q_3 = \left(\frac{d}{dt}\right)^{3/2}, \quad \text{in 2-D ,}$$

$$Q_1 = \left(\frac{d}{dt}\right)^{1},\ Q_2 = Q_3 = Q_4 = \left(\frac{d}{dt}\right)^{2}, \quad \text{in 3-D .}$$

For 2-D results with preconditioning, convergence is achieved under 40 iterations producing accurate source inversions; see figures 5.8 and 5.11a. The non-preconditioned results demonstrates CGNE iterates heading in the right direction, though at an unreasonably slow rate. The 3-D case shows analogous results to some extent, mainly the inability of CGNE iterates without preconditioning to achieve a reasonable estimations in under 150 iterations. Figure 5.9 shows that inversion with preconditioning is pretty successful in retrieving the correct MPS coefficients w_1, w_2, and w_3, despite not having met the sufficient residual or gradient reduction stopping criteria. Larger errors in w_4, notwithstanding a data residual reduction of the order 10^{-4}, can be attributed to the fact that receivers are positioned in a line close to the plane where the multipole associated with w_4, that is $\frac{\partial}{\partial x_3}\delta(\mathbf{x} - \mathbf{x}^*)$, produces no response, also known as a *nodal plane*. Given the choice of source location, the nodal plane considered here consists of the x_1-x_2-plane centered at $x_3 = 103m$.

Better inversion results are obtained by improving the data coverage. Figure 5.10 plots the estimated MPS coefficients for 3-D mixed first order multipole as done in the previous example but with data collected by two lines of receivers that are mutually

perpendicular, as illustrated in figure 5.2c. Observed data is plotted in figure 5.7. Estimated sources with preconditioning result in a significant drop in residual though CGNE had to run the full 150 iterations. However, given that the data now includes a line of receivers that captures the anisotropy in the y-direction, the estimated wavelet w_4 is an order of magnitude more accurate.

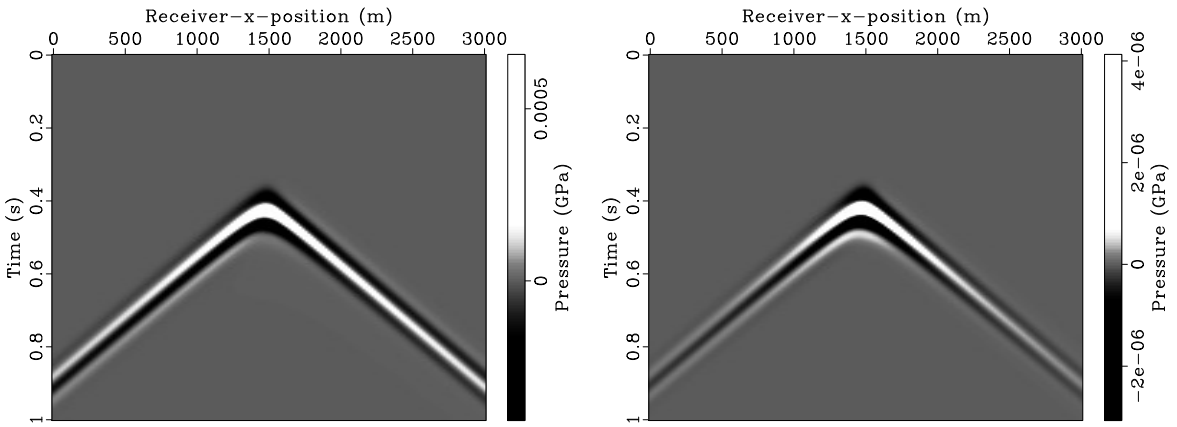

(a) 2-D case (b) 3-D case

Figure 5.6 : Pressure time traces used as "observed data" in source inversions for mixed first-order multipole in 2-D and 3-D. Homogeneous unbounded model test case.

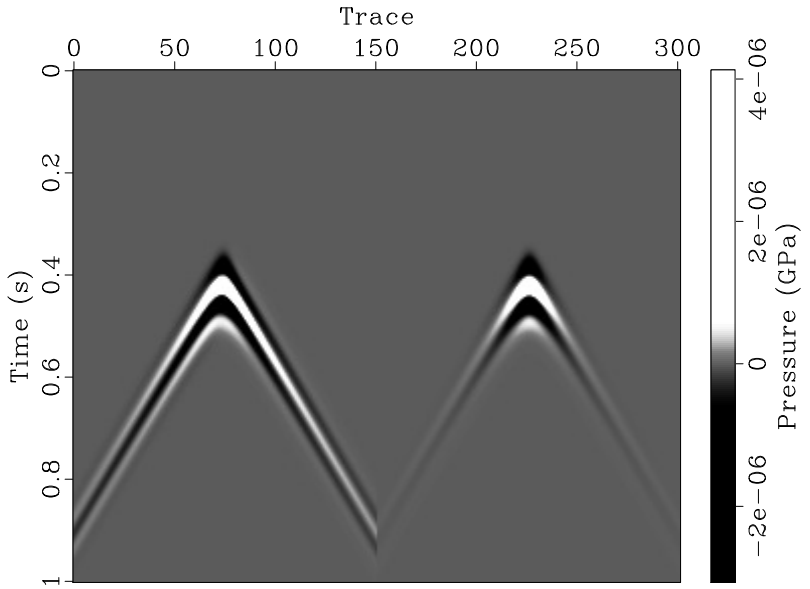

Figure 5.7 : Pressure time traces used as "observed data" in source inversions for mixed first-order multipole in 3-D with better data coverage. Homogeneous unbounded model test case.

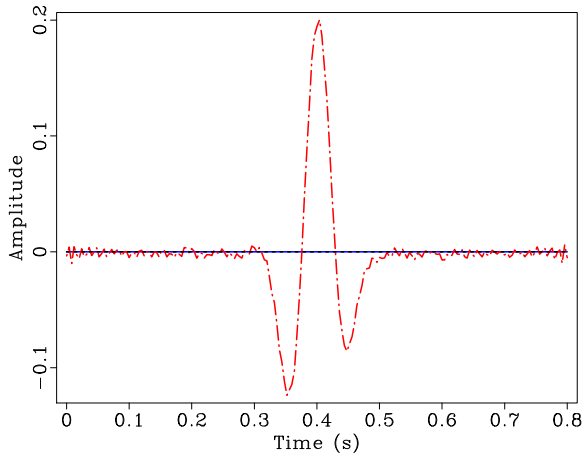

(a) 2-D case, MPS coefficient w_1

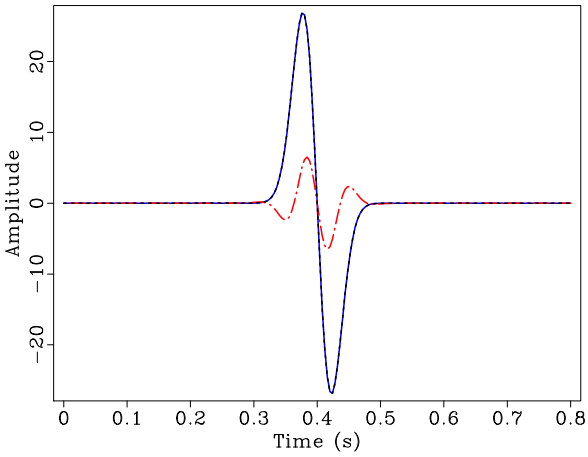

(b) 2-D case, MPS coefficient w_2

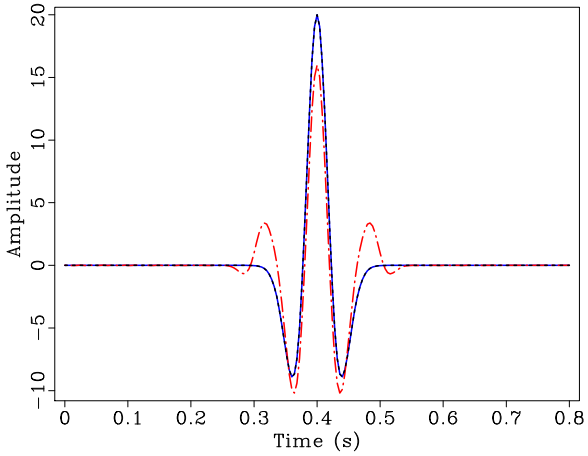

(c) 2-D case, MPS coefficient w_3

Figure 5.8 : Estimated MPS coefficients for scalar mixed first-order multipole in 2-D. True solution (solid blue) and estimated solution via CGNE with ($--$ black) and without ($- \cdot -$ red) preconditioning.

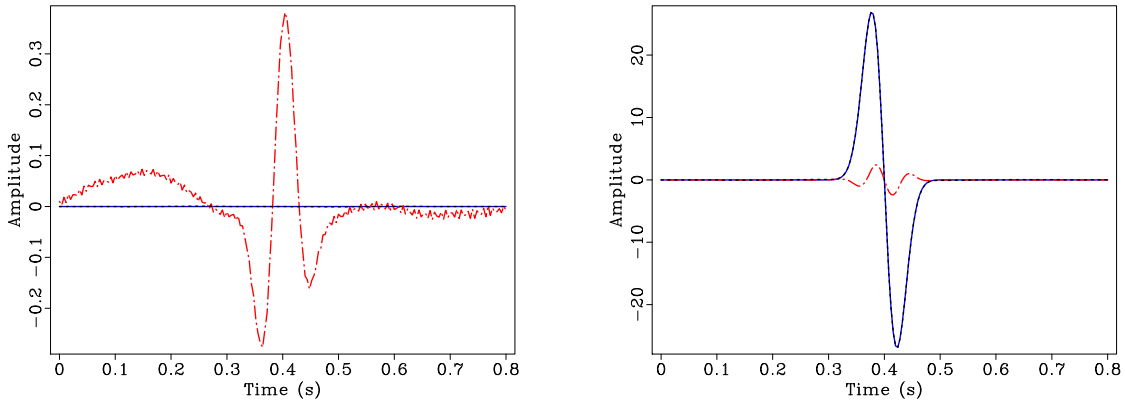

(a) 3-D case, MPS coefficient w_1

(b) 3-D case, MPS coefficient w_2

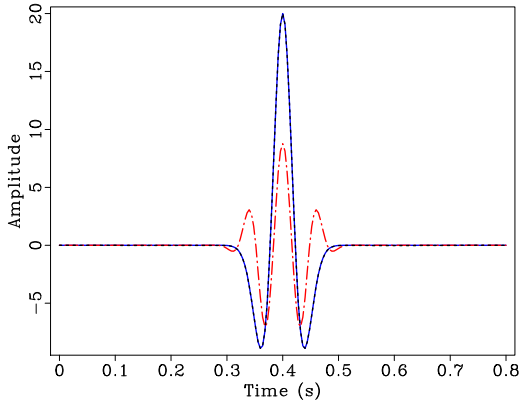

(c) 3-D case, MPS coefficient w_3

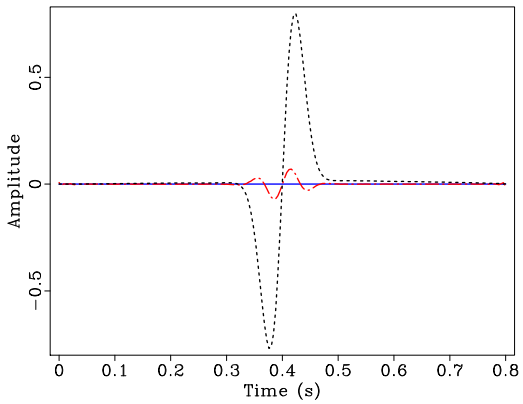

(d) 3-D case, MPS coefficient w_4

Figure 5.9 : Estimated MPS coefficients for scalar mixed first-order multipole in 3-D. True solution (solid blue) and estimated solution via CGNE with ($--$ black) and without ($- \cdot -$ red) preconditioning.

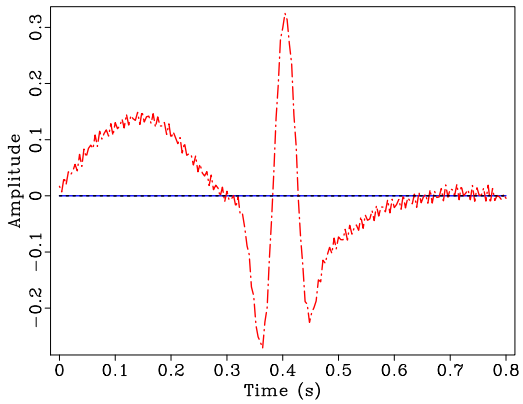

(a) 3-D case, MPS coefficient w_1

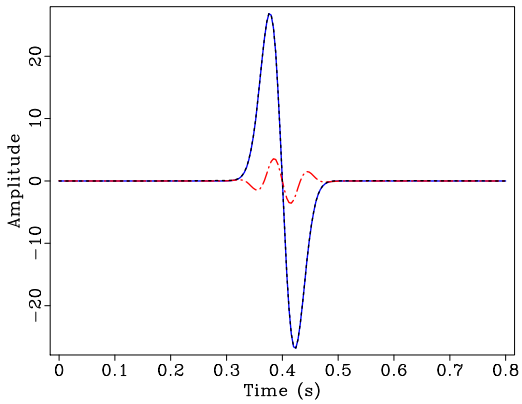

(b) 3-D case, MPS coefficient w_2

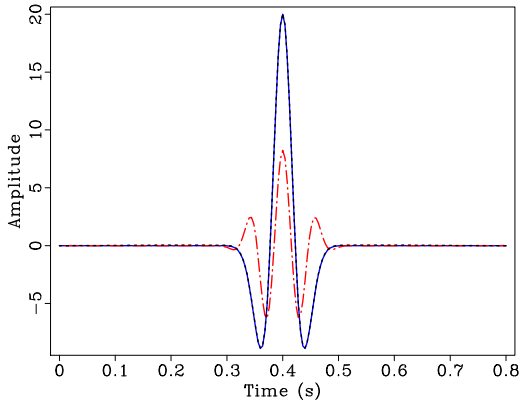

(c) 3-D case, MPS coefficient w_3

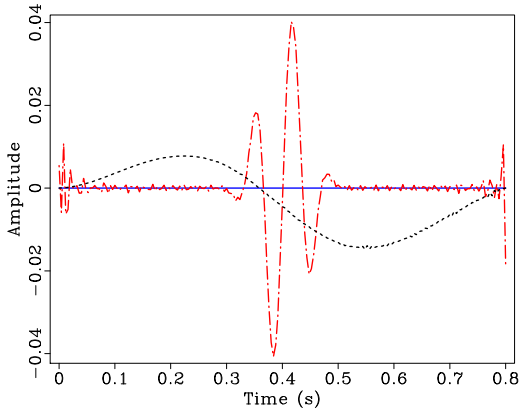

(d) 3-D case, MPS coefficient w_4

Figure 5.10 : Estimated MPS coefficients for scalar mixed first-order multipole in 3-D with better data coverage. True solution (solid blue) and estimated solution via CGNE with ($--$ black) and without ($-\cdot-$ red) preconditioning.

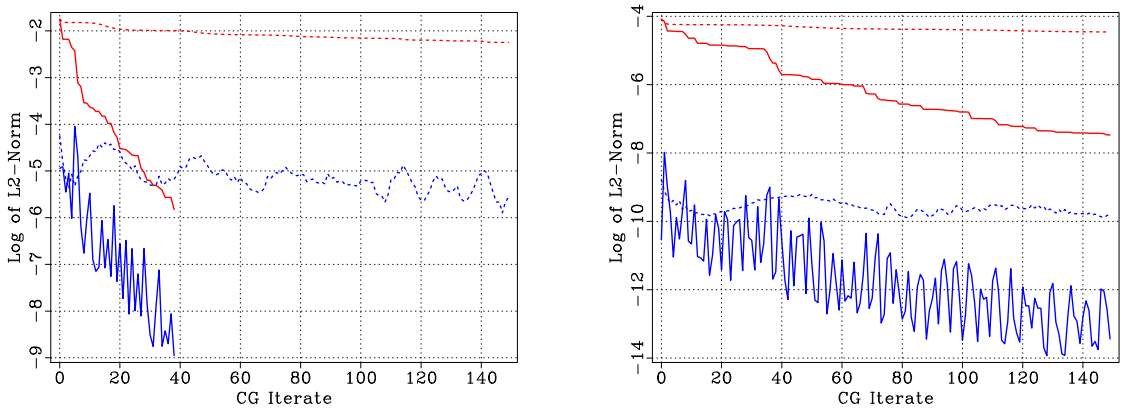

(a) 2-D case (b) 3-D case

Figure 5.11 : CGNE convergence plots for source estimation of scalar mixed first-order multipoles in 2-D and 3-D. Log of L^2-norms (data and MPS space resp.) of residuals (red/top) and gradients (blue/bottom) plotted for CGNE iterates with (solid) and without (−−) preconditioning.

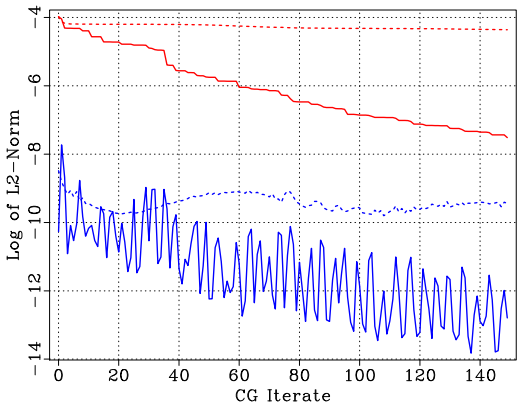

Figure 5.12 : CGNE convergence plots for source estimation of scalar mixed first-order multipole in 3-D with better data coverage. Log of L^2-norms (data and MPS space resp.) of residuals (red/top) and gradients (blue/bottom) plotted for CGNE iterates with (solid) and without (−−) preconditioning.

Mixed MPS in Heterogeneous Medium

This final source inversion test seeks to estimate the mixed multipole source from the previous subsection in a 2-D heterogenous medium under a more standard source-receiver configuration used in marine reflection seismology. Figure 5.13 plots the acoustic medium parameters for the 2-D dome model considered in this test, along with source-receiver geometry. The first layer in the dome model corresponds to a water layer with a speed of sound of $1.5km/s$. PML layers are added at all boundaries of the domain except at depth $z = 0m$, simulating the ocean-air interface by applying free-surface boundary conditions. Other test specifications include:

- total recording time $T = 2.5s$;
- spatial grid size $h = 10m$;
- simulation time step $\Delta t = 1ms$.

Observed data is plotted in figure 5.14 illustrating elaborate data waveforms typical of reflection seismology. Estimated MPS coefficients are given in figure 5.16 along with CGNE convergence plots in figure 5.15 for results with and without preconditioning. The preconditioned inversion manages to reduce the residual between observed and predicted data by roughly three orders of magnitude, albeit taking the full 150 iterations. Furthermore, though the estimated MPS coefficients contain significant errors they bare a good resemblance to the true source.

Clearly multipole source estimation under a more realistic setup such as what is used in marine reflection seismology results in a harder inversion problem which can be to some degree attributed to the how much of the anisotropy of the source is captured by the data given source-receiver geometry. In particular receivers are placed at or near the same depth as the source resulting in data content fundamentally different from the previous inversions. On top of that, the direct waveform of the source is further intermixed with reflections from the free-surface (ocean-to-air interface) and reflections from subsurface features at later times. Inversion results can be improved with multi-shot data, that is shifting (or towing) the source and receivers along the x_2-direction and inverting for the MPS coefficients. If the source is assumed to be reproducible (same MPS coefficients for different source locations) then one could use multi-shot data to obtain a better source inversion. The key idea here is that subsurface features will provide different data as the source and receivers are towed, hence in essence multi-shot data will improve data coverage and ultimately inversion results.

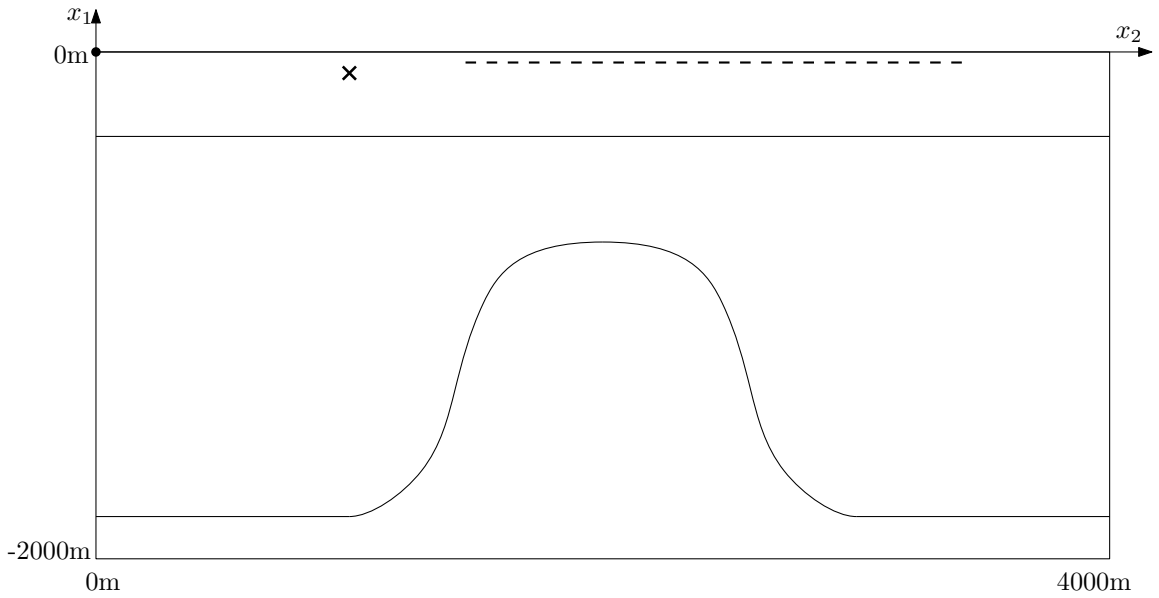

(a) Source-receiver geometry. Receivers and source depicted by a dashed line and a cross, respectively. Receiver $\mathbf{x}_{i_r} = (-40m, 1400m : 20m : 3400m)$ and source position $\mathbf{x}^* = (-103m, 1003m)$.

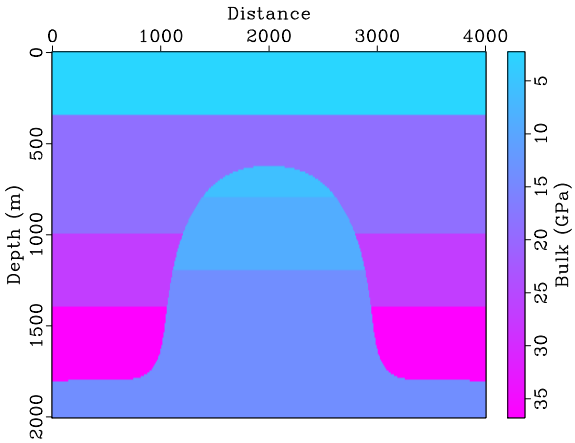

(b) Bulk modulus

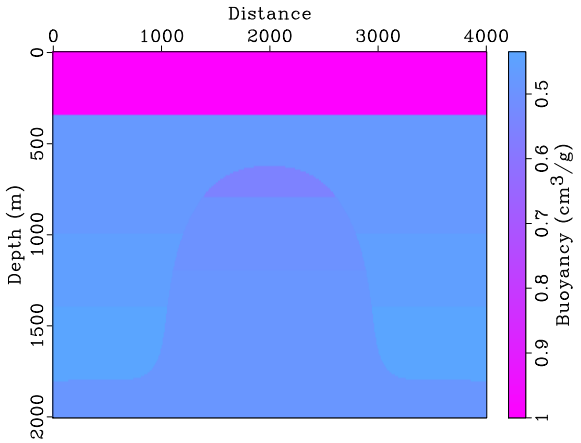

(c) Buoyancy

Figure 5.13 : Dome model and source-receiver geometry specifications for 2-D mixed multipole source inversion with reflection setup.

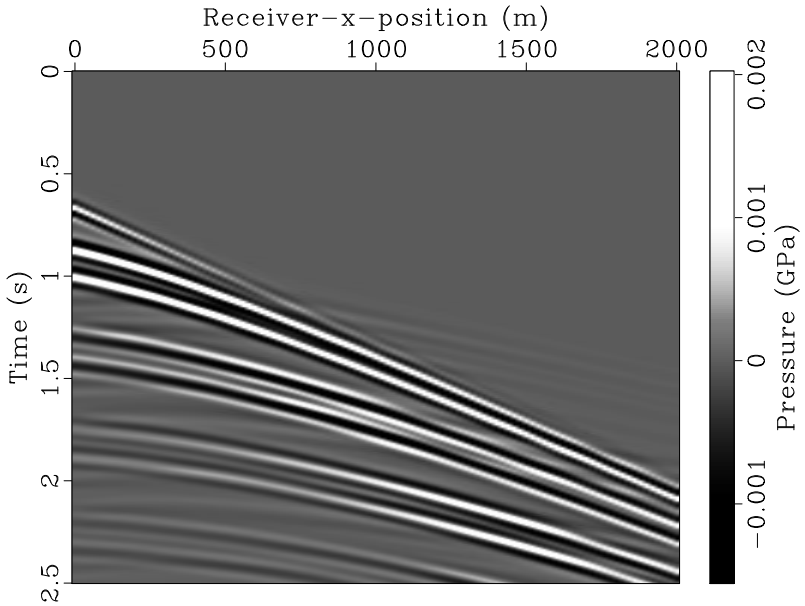

Figure 5.14 : Pressure time traces used as "observed data" in source estimation for scalar mixed first order multipole in 2-D with dome model and reflection source-receiver setup.

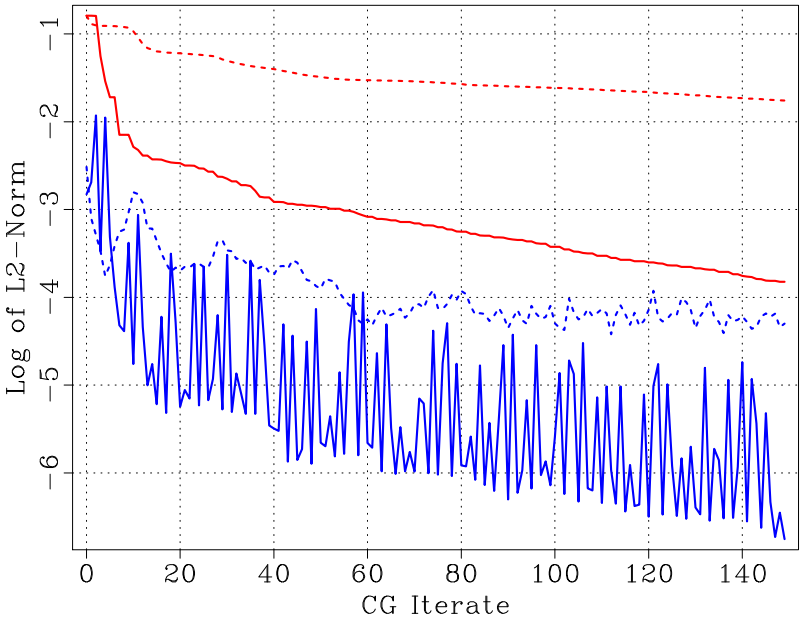

Figure 5.15 : CGNE convergence plots or scalar mixed first-order multipole in 2-D with dome model and reflection source-receiver setup. Log of L^2-norms (data and MPS space resp.) of residuals (red/top) and gradients (blue/bottom) plotted for CGNE iterates with (solid) and without (−−) preconditioning.

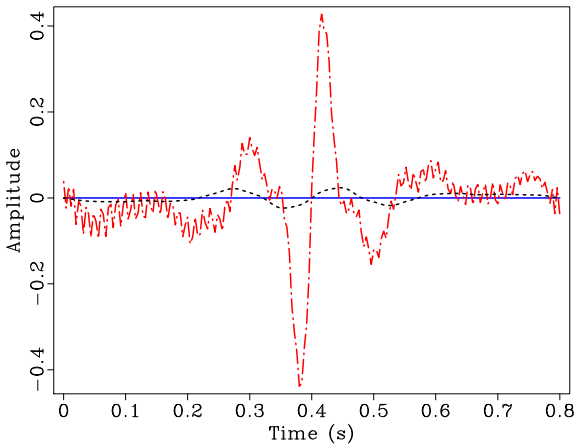

(a) MPS coefficient w_1

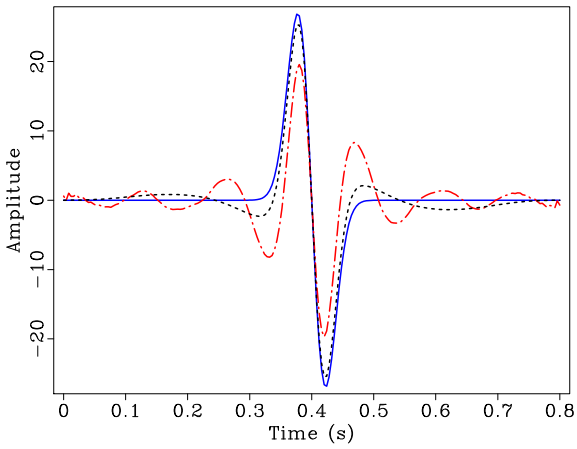

(b) MPS coefficient w_2

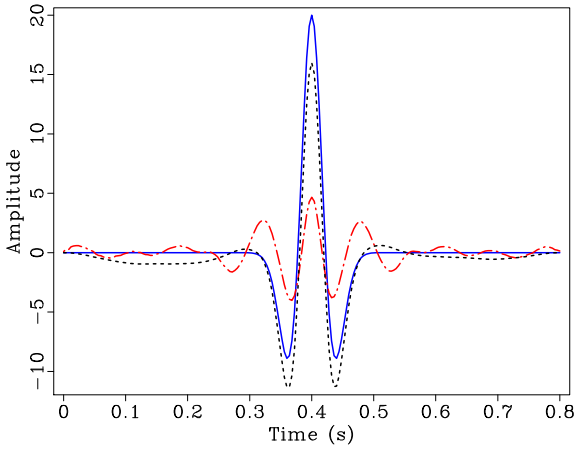

(c) MPS coefficient w_3

Figure 5.16 : Estimated MPS coefficients for scalar mixed first order multipole in 2-D with dome model and reflection source-receiver setup. True solution (solid blue) and estimated solution via CGNE with ($--$ black) and without ($-\cdot-$ red) preconditioning.

model	source		data residual redn.	gradient redn.	src error redn. in $\|\cdot\|_{\mathfrak{W}}$	src error redn. in $\|\cdot\|_{\mathfrak{W}'}$	# iter.
2-D hom.	$\mathbf{s} = (0, 0)$		1.84×10^{-4}	9.63×10^{-5}	9.77×10^{-4}	2.67×10^{-4}	33
		w/ PC	8.53×10^{-5}	1.03×10^{-4}	1.73×10^{-4}	8.22×10^{-5}	4
3-D hom.	$\mathbf{s} = (0, 0, 0)$		1.95×10^{-4}	7.92×10^{-5}	3.00×10^{-3}	2.82×10^{-3}	100
		w/ PC	2.72×10^{-5}	2.73×10^{-5}	2.59×10^{-5}	2.71×10^{-5}	4
2-D hom.	$\mathbf{s} = (0, 1)$		1.46×10^{-3}	2.71×10^{-4}	1.93×10^{-2}	1.39×10^{-2}	150
		w/ PC	8.83×10^{-5}	1.85×10^{-3}	1.11×10^{-3}	8.12×10^{-5}	4
3-D hom.	$\mathbf{s} = (0, 1, 0)$		1.56×10^{-2}	1.05×10^{-2}	1.13×10^{-1}	3.42×10^{-2}	150
		w/ PC	6.01×10^{-5}	1.34×10^{-2}	1.75×10^{-3}	7.57×10^{-5}	20

Table 5.1 : Summary of results for single scalar MPS inversions with and without preconditioning, containing data residual reduction, gradient reduction, and errors in MPS coefficients with respect to $\|\cdot\|_{\mathfrak{W}}$ and $\|\cdot\|_{\mathfrak{W}'}$ norms.

model	source		data residual redn.	gradient redn.	src error redn. in $\|\cdot\|_{\mathfrak{W}}$	src error redn. in $\|\cdot\|_{\mathfrak{W}'}$	# iter.
2-D hom.	$\|\mathbf{s}\| \leq 1$		3.17×10^{-1}	9.34×10^{-2}	7.82×10^{-1}	6.31×10^{-1}	150
		w/ PC	8.42×10^{-5}	9.70×10^{-5}	5.91×10^{-4}	1.43×10^{-4}	39
3-D hom.	$\|\mathbf{s}\| \leq 1$		4.21×10^{-1}	1.03×10^{-1}	9.11×10^{-1}	8.99×10^{-1}	150
		w/ PC	4.12×10^{-4}	1.39×10^{-3}	2.60×10^{-2}	2.24×10^{-2}	150
3-D hom. +	$\|\mathbf{s}\| \leq 1$		4.14×10^{-1}	9.95×10^{-2}	9.05×10^{-1}	9.15×10^{-1}	150
		w/ PC	2.90×10^{-4}	9.06×10^{-4}	6.48×10^{-3}	1.64×10^{-3}	150
2-D dome	$\|\mathbf{s}\| \leq 1$		1.08×10^{-1}	1.38×10^{-2}	6.57×10^{-1}	8.71×10^{-1}	150
		w/ PC	9.32×10^{-4}	8.32×10^{-4}	2.21×10^{-1}	6.76×10^{-2}	150

Table 5.2 : Summary of results for mixed scalar multipole source inversions with and without preconditioning, containing data residual reduction, gradient reduction, and errors in MPS coefficients with respect to $\|\cdot\|_{\mathfrak{W}}$ and $\|\cdot\|_{\mathfrak{W}'}$ norms. 3-D hom.+ refers to 3-D test case with optimal/improved data coverage.

Discussion

For all source inversions considered in this chapter, a dramatic acceleration in convergence of CGNE iterates is observed when applying my preconditioner. Moreover, accurate inversions are achieved when CGNE iterates satisfy the sufficient residual or gradient reduction stopping criterion; see tables 5.1 and 5.2 for a summary of results. Even in cases where CGNE ran for the full 150 iterations, the preconditioned results gave more accurate inversions in terms of both smaller data residuals and errors in estimated MPS coefficients.

It is not too surprising to observe that the source estimation problem becomes increasingly difficult as the complexity of the source representation increases, further motivating the need of preconditioners. In particular, for the mixed first order multipole case (i.e., sources of the form 5.7 or 5.8) the non-preconditioned results yielded unsatisfactory data residual reductions of the order $O(10^{-1})$ and relative errors in the estimated MPS coefficients of the order $O(10^{-1})$. This is to be contrasted with their preconditioned counterparts where data residual reductions of $O(10^{-4})$ are obtained and relative errors of estimated MPS coefficients ranged from $O(10^{-1})$ to $O(10^{-4})$.

Another important aspect related to the well-posedness and better conditioning of source inversion is data content and its relation to the source radiation field and subsequently the determinability of MPS coefficients. It was observed for the 3-D mixed multipole case that a line of receivers placed near a nodal plane related to MPS coefficient w_4 resulted in the under-determination of said MPS coefficient.

Introducing a second line of receivers, perpendicular to the first, improved the amount of information available to better determine w_4 thus producing a more accurate source estimate (a reduction in relative error by $O(10^{-1})$) though this was mainly observed for the preconditioned results.

The role of data coverage in the conditioning of the source inversion problem will play an increasingly important role as the complexity of the source radiation pattern increases with number of terms included in its multipole representation. Preconditioners developed here are not meant to address all aspects of the difficulties associated with multipole source inversion, in particular, ill-conditioning related to poor data coverage. Other regularization techniques, such as Tikhonov regularization (Koch, 1991), should be incorporated in conjunction with my preconditioning strategy and should be further studied under cases where data acquisition geometry results in known ill-conditioning.

Conclusion

In this chapter, I have developed a strategy for better-conditioning the multipole source inversion problem via FWI, or equivalently solving the normal equation 5.4 for MPS coefficients. Given the size of problems related to exploration seismology, iterative solvers, namely CGNE, are used in this work. My preconditioning approach for accelerating CGNE (or in general Krylov subspace methods) is based on effectively redefining L^2-inner product of the domain (MPS) space to yield a better bounded

forward map $F[m]$. In particular, my preconditioners consist of fractional derivative/integral operators whose order is chosen semi-heuristically based on the analytical solutions of the acoustic wave equation in unbounded media with multipole source terms; see appendix B.

Numerical experiments conducted here demonstrate dramatic accelerations of CGNE iterates and accuracy of estimated sources with preconditioning. Moreover, regularization techniques such as optimized data coverage and Tikhonov regularization can and should be applied conjunctly to further improve source inversions.

Chapter 6

Airgun Array Sources

The main goal of this thesis is to provide a framework for accurate source representation and inversion of (potentially anisotropic) seismic sources as a means for aiding the seismic inversion problem, that is estimating medium parameters via FWI. As a step towards this goal, I utilize the multipole source inversion platform I have developed to study in this chapter the accuracy of source representation via multipoles of realistic seismic sources, in particular *airgun arrays* used in marine seismic surveying.

6.1 Background

Airguns are the most common type of sources used in marine seismic surveying primarily due to their reproducibility in comparison to other modalities, such as waterguns and underwater explosives. Highly compressed air is released by the airgun resulting in an air cavity, or bubble, that expands to achieve a balance between the surrounding hydrostatic pressure and the bubble's internal pressure. The bubble's expansion decelerates once the pressure equilibrium is reached but continues to expand to the point of zero acceleration at which the hydrostatic pressure is now greater than the internal bubble pressure. The bubble then contracts and the process of expansion and contraction repeats resulting in the *oscillating bubble* phenomenon. Figure 6.1 il-

lustrates the process explained above. Acoustic waves, to be later converted to elastic waves once they interact with the earth, are produced from the sudden acceleration and deceleration of the oscillating bubble generated by airguns.

The *source signature* of an airgun, or array of airguns, refers to the recorded pressure field by a hydrophone located directly below the source. The source signature is defined as the hypothetical output pressure measured $1m$ from a theoretical point-source. For example, suppose one records pressure time-trace $p(t)$ at a distance r below the airgun. Assuming geometrical spreading effects only, the source signature is given by simply scaling measured $p(t)$,

$$\text{signature}(t) = 4\pi c^2 r p(t) \tag{6.1}$$

where c is the velocity of the medium. Units of measurement for reporting source signatures are typically given in bar-m, defined as the measured pressure in bars ($= 10^5$Pa) at distance $1m$ from theoretical point-source. Figure 6.2a depicts a typical

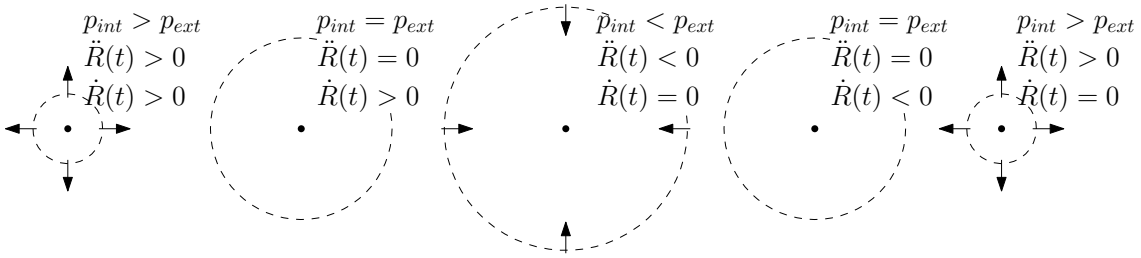

Figure 6.1 : Diagram of oscillating bubble phenomenon, p_{int} and p_{ext} denoting interior and exterior pressures with respect to the bubble, and $R(t)$ is the radius of the bubble as a function of time.

source signature for a single airgun; the primary wave and its ghost (reflection from free surface) are accounted for in the first spike and dip, and bubble oscillations are observed in later arrival times.

An illustration of a typical amplitude spectrum of the source signature is shown in figure 6.2b; note the dips in amplitude, referred to as *ghost notches* which are caused by the ghost pulse and thus depend on source depth. In fact, the first ghost notch at frequency $\omega_0 \neq 0$ is predicted by the following formula,

$$\omega_0 = \frac{c}{2D}$$

where D is the source depth (Caldwell and Dragoset, 2000). Clearly, decreasing source depth D will yield a larger ω_0 and hence a broader bandwidth for which to work with. Conversely, the closer the airgun is to the surface the more the produced pressure output is affected by rough tides and turbulence negatively affecting the energy transmitted into the earth. In practice source depths are chosen to be between 10m – 2m, resulting in a usable frequency around 50Hz – 250Hz respectively. The amplitude spectra of source signatures are reported in decibels relative to a reference pressure and at times normalized by frequency. For example, the amplitude units given in figure 6.2b are dB re 1μPa/Hz which denotes a decibel level relative to 1μPa normalized by frequency.

The ideal seismic source can be characterized as having a strong initial peak and a short duration, i.e., and impulsive source. Bubble oscillations impede the airgun

from producing a waveform with small support. Consequently, arrays of airguns of multiple sizes (airgun size affects periodicity of oscillation) are used to generate pulses that are aligned with the direct wave but interfere destructively at later times. The end result is a source signature with a stronger primary pulse and damped bubble oscillations. Figure 6.3 shows a cartoon of a typical source signature for an array of airguns. Practitioners refer to the amplitude difference between primary wave and it ghost as the peak-to-peak (P-P) amplitude. Similarly, the bubble-to-bubble (B-B) amplitude refers to the amplitude difference between the first bubble oscillation and its ghost as shown in figure 6.3. A good source signature is characterized by a large P-P amplitude and a small peak-to-bubble ratio (PBR), that is small $\frac{P-P}{B-B}$.

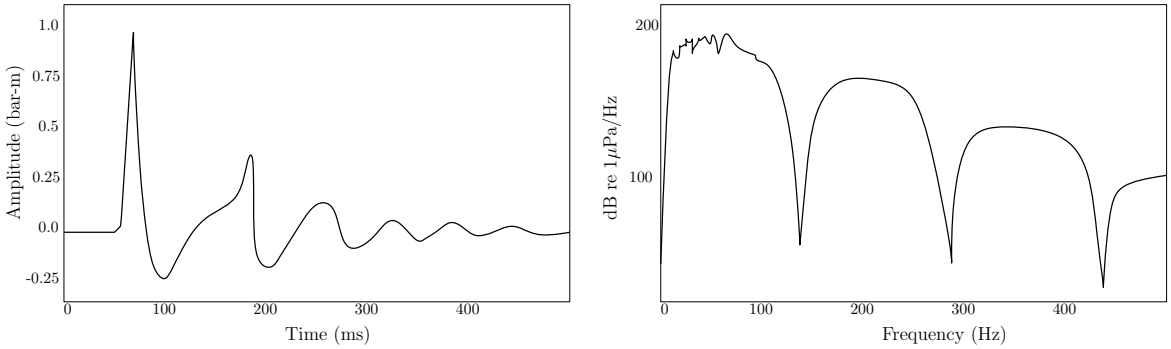

(a) Single airgun signature.

(b) Amplitude spectrum of airgun signature.

Figure 6.2 : Illustrative source signature for single in time domain and its amplitude spectrum.

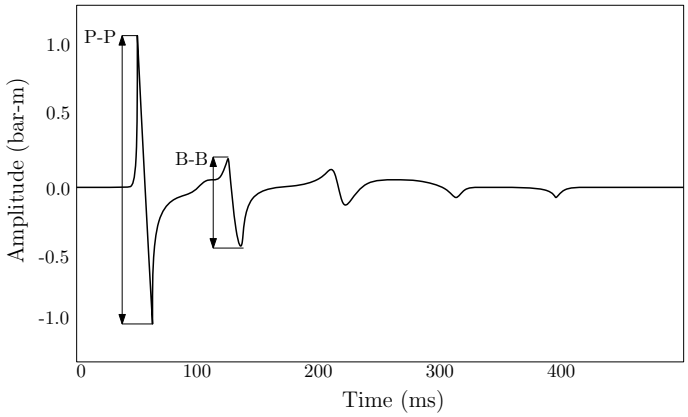

Figure 6.3 : Illustrative source signature of an airgun array.

6.2 Modeling

The pressure field generated from a collapsing and expanding spherical cavity was first studied by Rayleigh (1917). Kirkwood and Bethe (1942) included compressibility effects in their study of shockwave formations from underwater explosions. Gilmore (1952) furthered the theory of bubble oscillations by taking into account viscosity in the medium. The following is the Gilmore equation for the acceleration of the particle velocity at the bubble wall based on approximations made by Kirkwood and Bethe (1942):

$$\ddot{R}R\left(1-\frac{\dot{R}}{c}\right)=\left(1+\frac{\dot{R}}{c}\right)H+\frac{R}{c}\left(1-\frac{\dot{R}}{c}\right)\dot{H}-\frac{3}{2}\dot{R}^2\left(1-\frac{\dot{R}}{3c}\right) \tag{6.2}$$

where R is the radius of the bubble, $\dot{R}$ is the bubble wall velocity, c is speed of sound in the disturbed fluid, and H is the specific enthalpy at the bubble wall. Many other works have contributed to the complexity of the bubble oscillating model,

making use of different approximations related to relevant continuum mechanics and thermal dynamics theory. Ziolkowski (1970) was one of the first to apply modeling theory, in particular, equation 6.2, to simulate source signatures of single airguns using experimental data to determine modeling parameters related to viscosity.

When modeling non-interacting airgun arrays, that is the case where source-to-source separation is large enough, simple superposition of source signatures from individual airguns effectively accounts for the overall array source signature. Safar (1976) suggests a separation greater than ten times the equilibrium bubble radius is sufficient for neglecting source-to-source interactions in their analysis of bubble oscillation dampening for the design of airgun arrays. At smaller source spacings complexities in source-to-source interactions arise from the effects of pressure fields of neighboring bubbles. Giles and Johnston (1973) hypothesized an apparent hydrostatic pressure observed for each airgun as a result of the acoustic pressures produced by other airguns in an array. Ziolkowski et al. (1982) also applied the notion of apparent hydrostatic pressure but concludes that the total acoustic pressure of the array can be reproduced by the superposition of "notional" airguns modeled as point-sources. In other words, the acoustic pressure produced from an array of airguns can be effectively simulated by the superposition of independent point-sources modified to account for the airgun-to-airgun interactions. Barker and Landrø (2013) model the effects of bubble coalescing for small source separation by dropping the spherical assumption of point-sources to better approximate the observed damping of primary pulse.

6.3 Preliminary Inversions

The goal of the numerical tests presented here is to quantify how accurately can an airgun array be modeled as a multipole source concentrated at the center of the array. To this end, I invert for MPS coefficients assuming the source is a multipole of order zero,

$$f(\mathbf{x},t) = w_1(t)\delta(\mathbf{x}-\mathbf{x}^*),$$

or a multipole of order at most one,

$$f(\mathbf{x},t) = w_1(t)\delta(\mathbf{x}-\mathbf{x}^*)+w_2(t)\frac{\partial}{\partial x_1}\delta(\mathbf{x}-\mathbf{x}^*)+w_3(t)\frac{\partial}{\partial x_2}\delta(\mathbf{x}-\mathbf{x}^*)+w_4(t)\frac{\partial}{\partial x_3}\delta(\mathbf{x}-\mathbf{x}^*), \tag{6.3}$$

and compare their data misfit.

I follow the strategy by Ziolkowski et al. (1982) and model the output pressure of an airgun array as the superposition of notional point-sources. Given an array configuration, along with airgun parameters, the signature for each point-source is computed using the modeling code AGORA, an open source Matlab-based code developed by Sertleka and Ainslieb (2015) that utilizes the notional airgun principle, multi-physics modeling of the oscillating bubble phenomena (i.e., Gilmore's equation), and other mass and heat transport considerations (MacGillivray, 2006). Airgun array configuration (figure 6.4a) and airgun parameters (table 6.1) were taken from the example included in the AGORA user guide. Notional source signatures are plotted for each airgun in figure 6.5.

The 2-4 staggered-grid finite difference scheme is used to compute observed data, shown in figure 6.7a, solving the acoustic equations in a water layer (i.e., $c = 1.5km/s$ and $\rho = 1.024g/cm^3$) with PML on all boundaries to simulate an infinite domain and right-hand source corresponding to the airgun array by treating each airgun as a point-source. Notional source signatures as computed by AGORA required some preprocessing in order to obtain the appropriate wavelets to be fed into IWave as sources traces. In particular, I had to apply a scaling factor of $10^{-9} \times c^2 \times 4\pi$ and a time-integration to account for the fact that the notional source signatures are in units of $Pa \cdot m$ and are related to equation 2.2, that is, the solution to the isotropic point radiator problem for acoustics in 3-D. A low pass filter with cutoff frequency at $60Hz$ is also applied to the source wavelets. Figure 6.6 plots the processed notional airgun signatures.

Source-receiver geometry is illustrated in figure 6.4, where the airgun array is placed at depth $-200m$ centered about the origin in the $x - y$ plane. Receivers are located at the surface boundaries of the physical domain, i.e., grids ($\Delta x = 40m$) over the six faces of the cube enclosing the source in order to capture as much information about the radiation pattern. Each contiguous group of 121 traces in the data corresponds to a grid of receivers at a particular face of the domain cube. The first two groups of 121 traces correspond to receivers on the $z = -400m$ and $z = 0m$ faces, third and fourth groups to faces with $x = -200m$ and $x = 200m$, and the last two groups with faces on $y = -200m$ and $y = 200m$ respectively.

MPS coefficients are estimated using the inversion strategy utilized in the previous section. In particular, sufficient reduction conditions in residual and gradient are set to 0.001 and a maximum number of 150 iterations of CGNE with preconditioning is applied for all inversion results presented in this section.

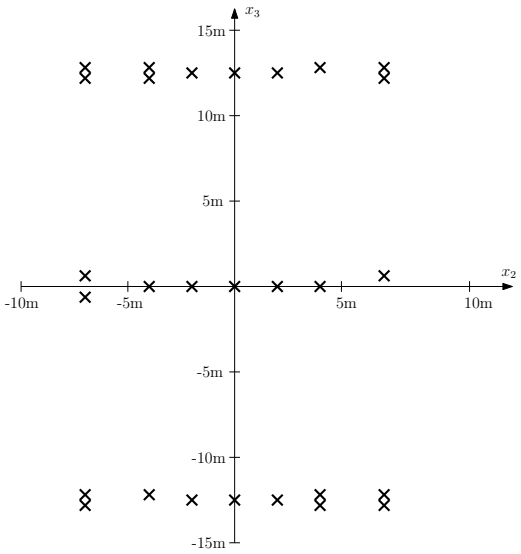

(a) Airgun array configuration, with airguns marked by crosses. Array located at depth $x_1 = -200m$.

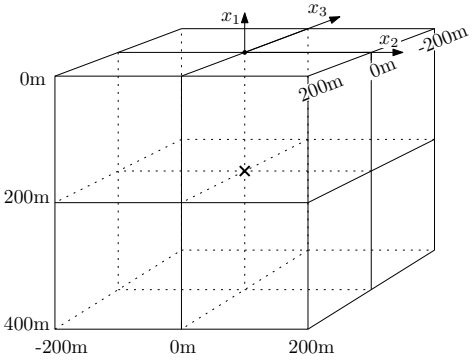

(b) Estimated multipole sources are located at $\mathbf{x}^* = (-200m, 0m, 0m)$. Receivers are positioned at each face of the cube surrounding the source, with $40m$ separation.

Figure 6.4 : Configuration of airgun array and source-receiver geometry for numerical tests.

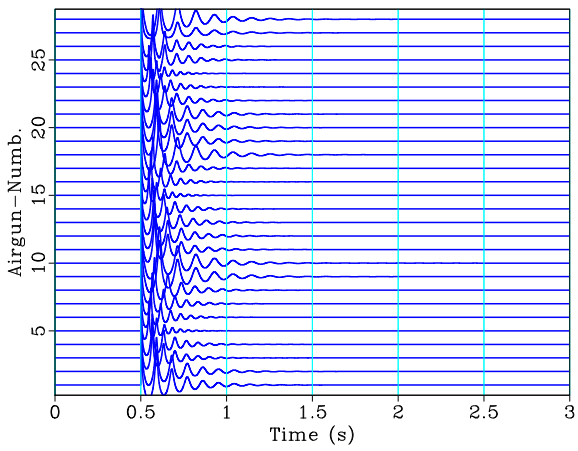

(a) Notional source signatures for all airguns in array.

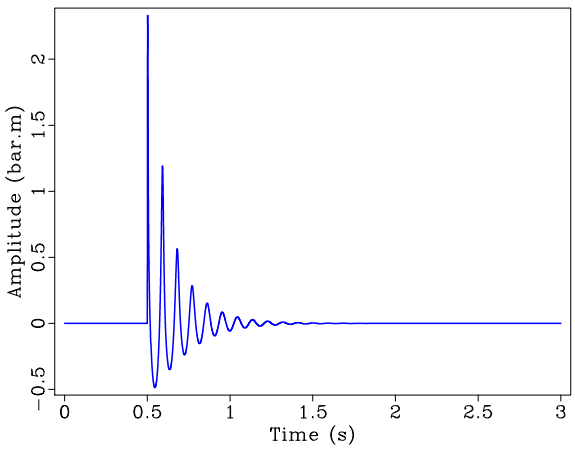

(b) Notional source signature for airgun #1.

Figure 6.5 : Notional airgun signatures computed from AGORA.

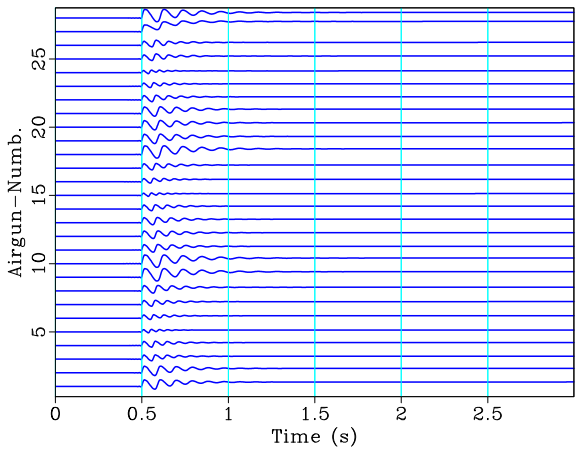

(a) Wavelets for all airguns in array.

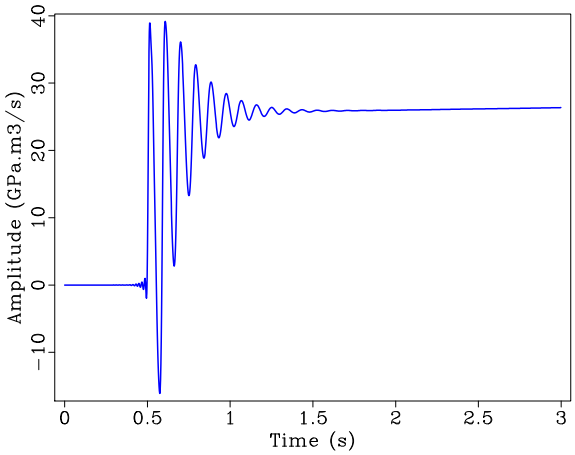

(b) Wavelet for airgun #1.

Figure 6.6 : Processed notional airgun signatures into point-source wavelets.

Airgun #	location [m]	volume [in.^{3}]	firing pressure [psi]
1	(-200,-7,12.9)	150	2000
2	(-200,-7,12.1)	150	2000
3	(-200,-4,12.9)	60	2000
4	(-200,-4,12.1)	60	2000
5	(-200,-2,12.5)	20	2000
6	(-200,0,12.5)	40	2000
7	(-200,2,12.5)	60	2000
8	(-200,4,12.9)	100	2000
9	(-200,7,12.9)	250	2000
10	(-200,7,12.1)	250	2000
11	(-200,-7,0.4)	100	2000
12	(-200,-7,-0.4)	100	2000
13	(-200,-4,0)	90	2000
14	(-200,-2,0)	60	2000
15	(-200,0,0)	20	2000
16	(-200,2,0)	40	2000
17	(-200,4,0)	70	2000
18	(-200,7,0.4)	250	2000
19	(-200,-7,-12.1)	150	2000
20	(-200,-7,-12.9)	150	2000
21	(-200,-4,-12.1)	150	2000
22	(-200,-2,-12.5)	70	2000
23	(-200,0,-12.5)	40	2000
24	(-200,2,-12.5)	20	2000
25	(-200,4,-12.1)	70	2000
26	(-200,4,-12.9)	70	2000
27	(-200,7,-12.1)	250	2000
28	(-200,7,-12.9)	250	2000

Table 6.1 : Airgun array parameters for numerical tests.

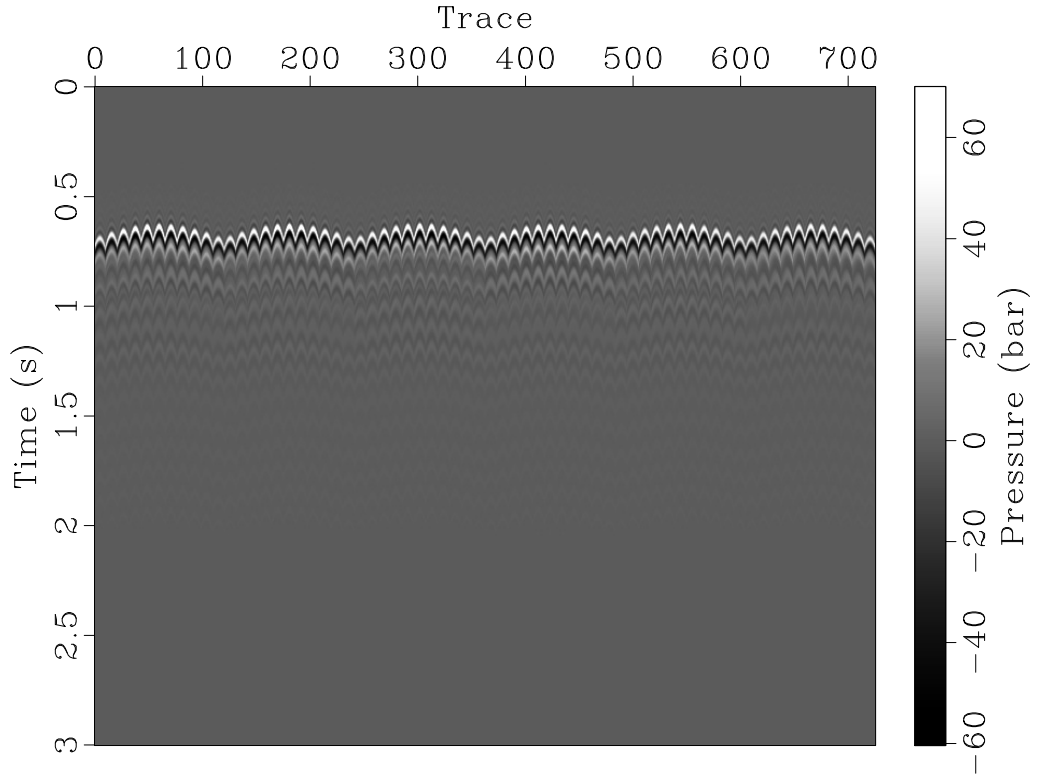

(a) Plot of all traces (clip=70).

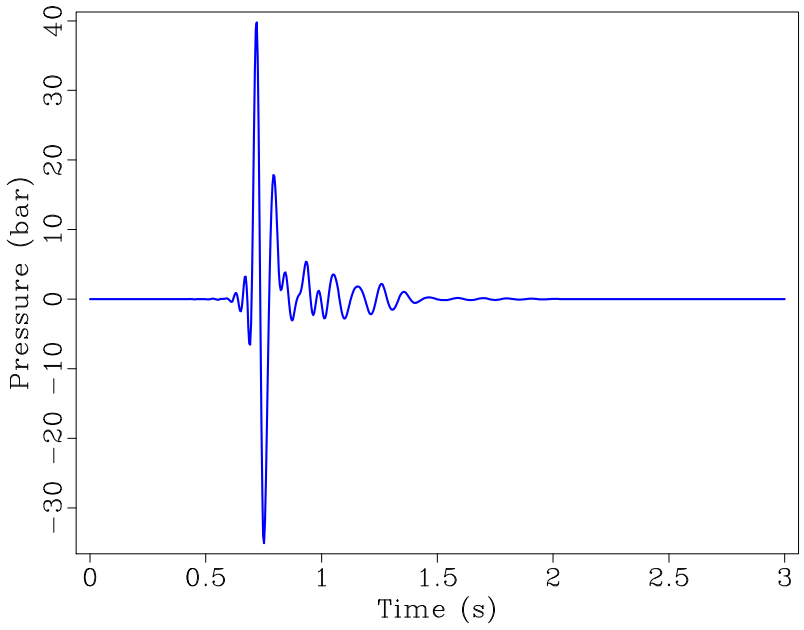

(b) Plot of first trace.

Figure 6.7 : Low pass filtered (cutoff at $30Hz$) observed data from airgun array, simulated by solving acoustic equations in first order form with $c = 1.5km/s$, $\rho = 1.024g/cm^3$, using 2-4 staggered grid finite difference with $\Delta x = 5m$ and $\Delta t = 1ms$.

Estimated MPS coefficients are shown in figures 6.10a and 6.11 for the multipole sources of order zero and one respectively. I have also included "source signatures" for each of the MPS coefficients as a means to better interpret the inversion results, see figures 6.10b and 6.12. The notion of "source signatures" I use here in the context of multipoles is as an extension of equation 6.1 for the isotropic point-radiator case. For example, the signature of w_1 is given by the measured pressure output of source $f(\mathbf{x}, t) = w_1(t)\delta(\mathbf{x} - \mathbf{x}^*)$ at one meter away from the source location, that is

$$\text{signature}[w_1](t) := \frac{w_1'(t)}{4\pi c^2}. \tag{6.4}$$

Note that I have scaled the derivative of w_1 by $(4\pi c^2)^{-1}$ and essentially ignored the displacement vector $\mathbf{x} - \mathbf{x}^*$ in the equation above. Again, the time derivative in equation 6.4 is related to the fact that I am dealing with the acoustic equations in first order form. A similar definition for MPS coefficients w_2, w_3 and w_4 follows from analytical solutions to the wave equation in 3-D with multipole sources. Namely,

$$\text{signature}[w_i](t) := \frac{w_i''(t)}{4\pi c^3}, \quad \text{for } i = 2, 3, 4. \tag{6.5}$$

Equations 6.4 and 6.5 above can be interpreted as roughly the far-field pressure output (modulus a sign and a time-shift) at one meter away from multipole source $f(\mathbf{x}, t) = w_i(t)b_i(\mathbf{x})$ with corresponding multipole base as given in equation 6.3 for $i = 2, 3, 4$.

Data residuals in figure 6.8 show that better data fit can be achieved if the source is modeled with a multipole of order one in comparison with using only an isotropic multipole term (i.e., $b_1 = \delta(\mathbf{x} - \mathbf{x}^*)$). The zeroth- and first-order multipole representations achieve a relative data misfit of roughly 16% and 6.49% respectively in the L^2-norm. Figure 6.9 plots a single trace of the observed data and predicted data acquired corresponding to the two estimated multipole sources. Incorporating dipole terms in the multipole representation clearly accounts for the complexity of the source, particularly in the time window between the initial impulse and the residual bubble oscillations.

Estimated MPS coefficients for both the zeroth and first order multipole representations recover a source that is dominated by an isotropic component, responsible in a sense for 84% of the observed data. Inversion results for the first order case reveal the presence of dipole terms $\frac{\partial \delta}{\partial x_2}$ and $\frac{\partial \delta}{\partial x_3}$ and, interestingly enough, also the absence of term $\frac{\partial \delta}{\partial x_1}$ (dipole in the depth direction) that helps account for an extra 10% of the data. These results are consistent with the asymmetry of the airgun array in both the x- and y-axis thus resulting in anisotropy captured by inversion of the first order multipole source model.

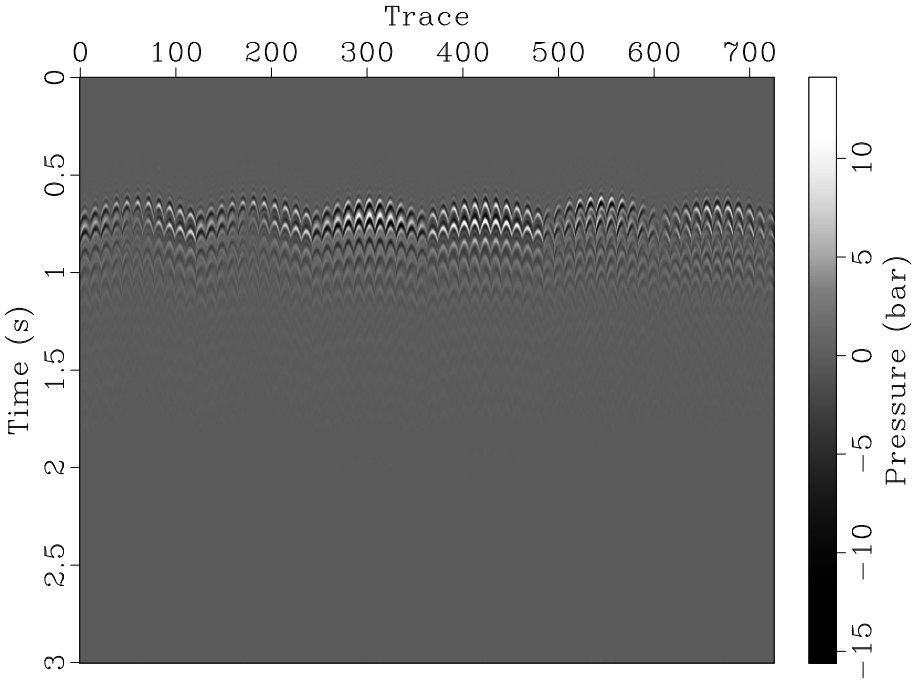

(a) Data residual using estimated isotropic point-source (clip=15).

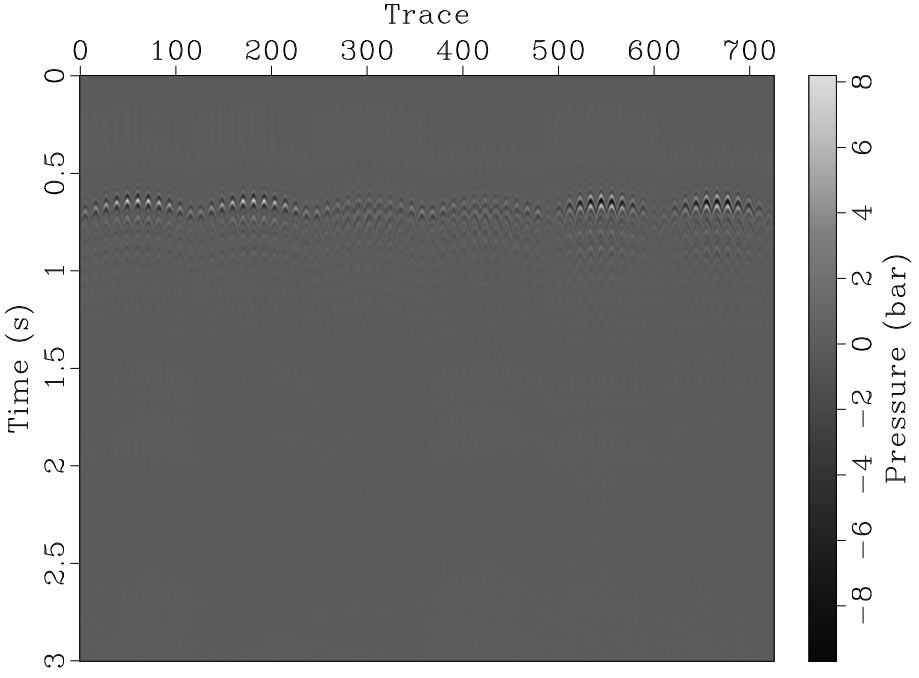

(b) Data residual using estimated multipole source of order at most one (clip=15).

Figure 6.8 : Data residual from recomputed time-traces with estimated multipole sources.

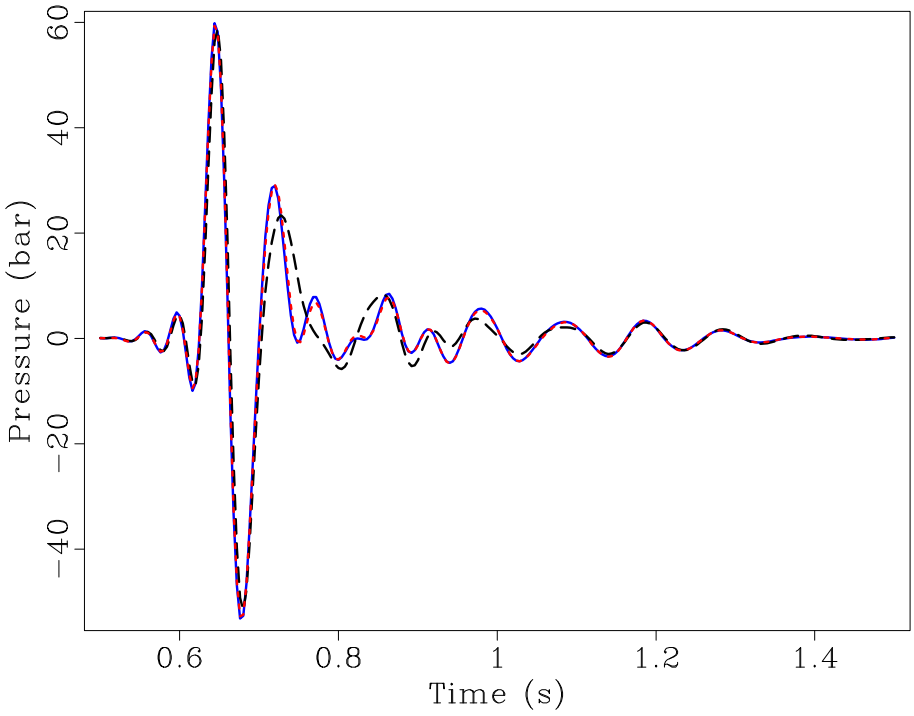

Figure 6.9 : Comparison of observed data (solid-blue) at trace number 300 with recomputed data using estimated multipoles of order zero (dashed-black) and order one (dotted-red).

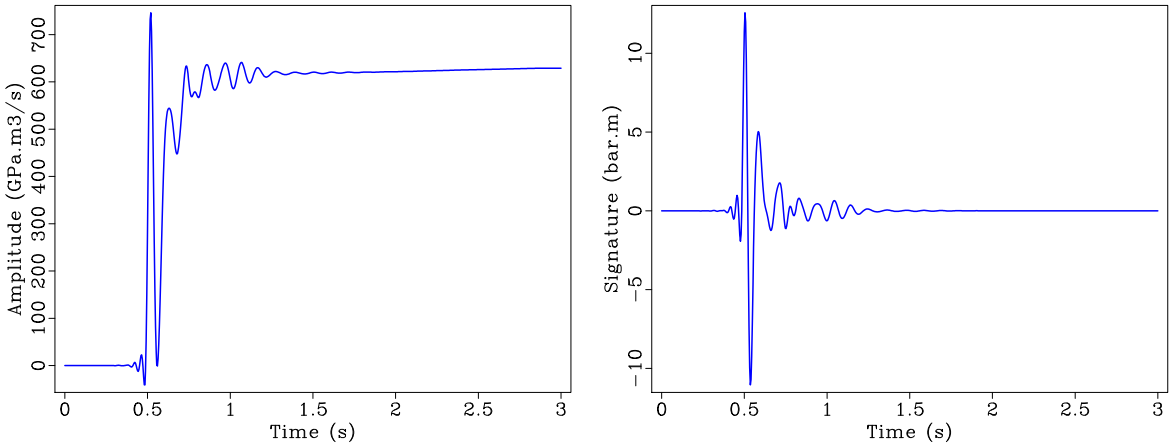

(a) Plot of w_1.

(b) Signature of w_1.

Figure 6.10 : Estimated MPS coefficient w_1 for isotropic point-source case and its signature.

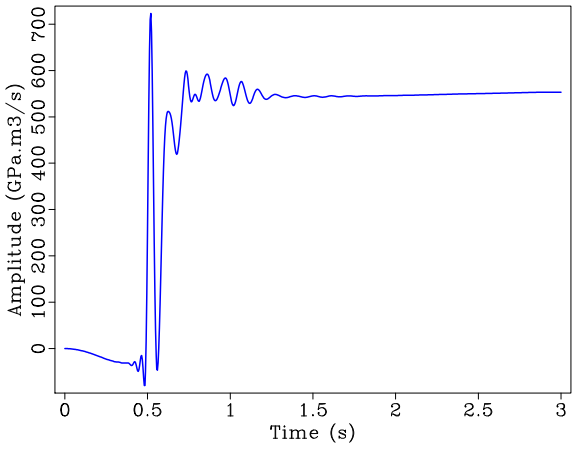

(a) MPS coefficient w_1

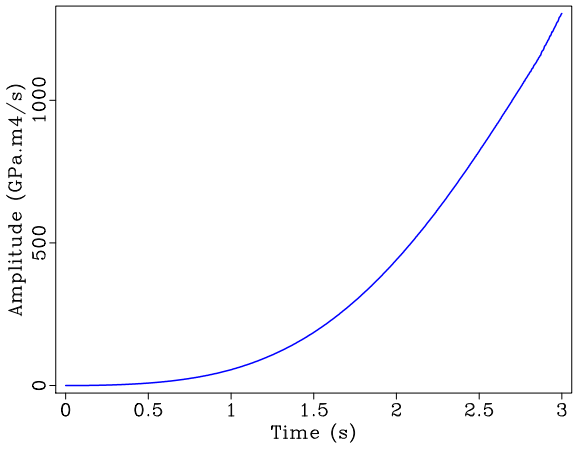

(b) MPS coefficient w_2

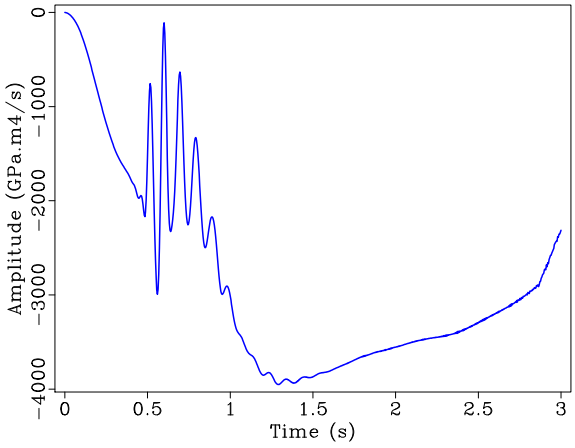

(c) MPS coefficient w_3

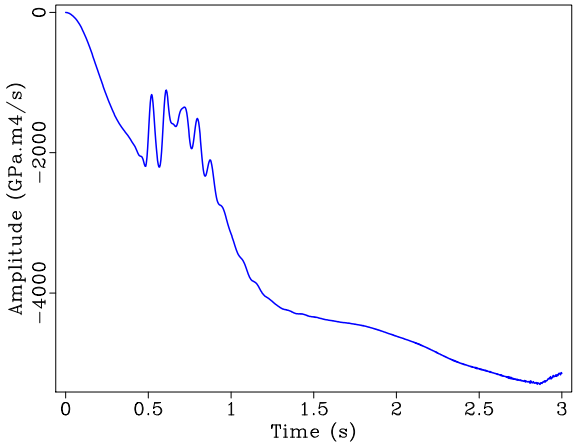

(d) MPS coefficient w_4

Figure 6.11 : Estimated MPS coefficients for multipole source of order at most one.

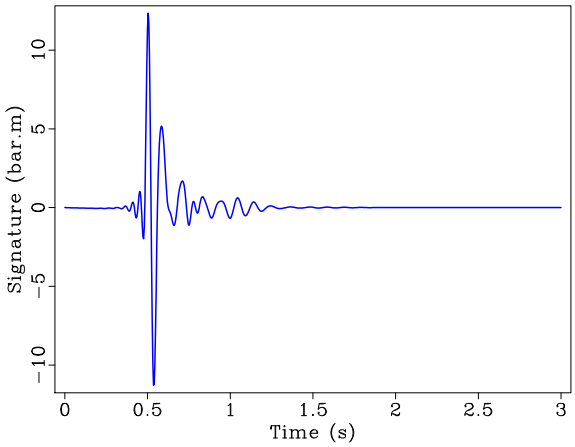

(a) Signature of w_1

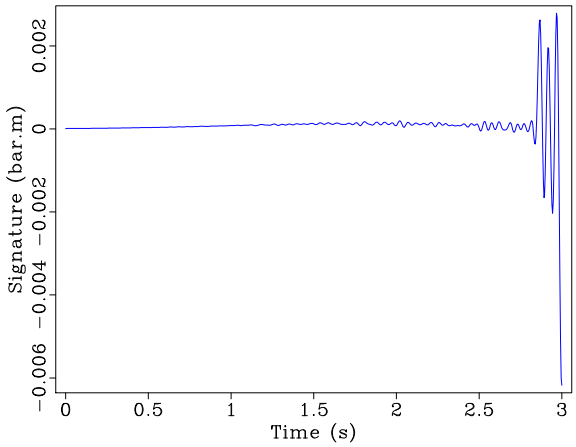

(b) Signature of w_2

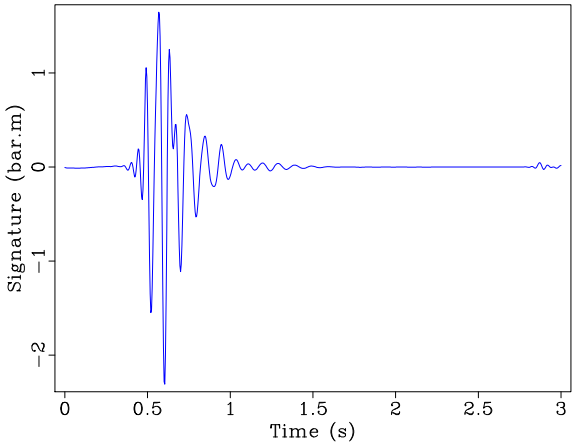

(c) Signature of w_3

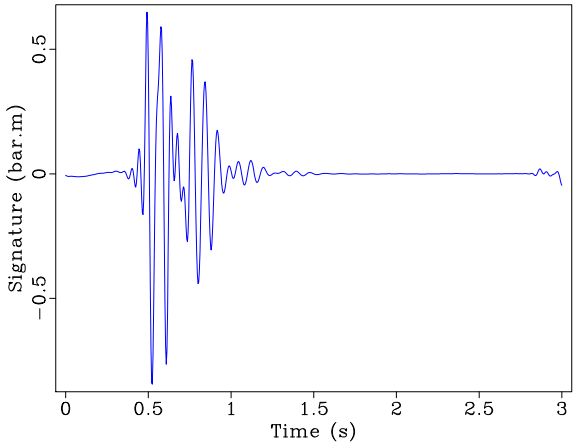

(d) Signature of w_4

Figure 6.12 : Signature of estimated MPS coefficients for multipole source of order at most one.

Discussion

Point support is an idealization: active source regions may be small or comparable to a wavelength in spatial extent. Santosa and Symes (2000) showed that multipole approximation (equation 2.3) of acoustic sources vanishing outside a small region of space exhibits a threshold effect, in that the error in the resulting acoustic fields drops abruptly as the length of the series (N in the expression 2.3) is increased past a critical value. This threshold in the number of terms necessary for an accurate approximation depends on the size of the active region and a measure of energy output relative to energy input (related to the degree of anisotropy). The analysis in (Santosa and Symes, 2000) pertains to acoustics, however, similar results are expected to hold for linear elastodynamics. Indeed, earthquake seismology has long used multipole source approximations in elastic media to describe earthquake mechanisms.

Results presented in this chapter are a first step towards determining the order of multipole necessary for a given degree of source anisotropy. In particular, I analyze the directivity of airgun arrays and the effectiveness of multipole source modeling to account for such anisotropy. A fair amount of the radiation pattern encoded in observed data can be explained by an isotropic point source, and even more if dipole terms are included. The next step would be to carry out similar source inversions with higher-order multipole terms to see if data residuals can be further minimized. Inversion of multipoles of higher order is however complicated by the fact that the map from source-to-data may have a nontrivial null space. As a matter of example,

consider the acoustic wave operator acting on $w(t)\delta(\mathbf{x})$, that is

$$\left(\frac{\partial^2}{\partial t^2} - c^2\nabla^2\right) w(t)\delta(\mathbf{x}) = w''(t)\delta(\mathbf{x}) - c^2 w(t)\nabla^2\delta(\mathbf{x}).$$

In other words, multipole source given by the right hand side term in the equation above produces a source radiation pattern that is mathematically idealized to a point, namely $w(t)\delta(\mathbf{x})$. Thus, outside of a finite region, this multipole source will not produce any waves, i.e., $w''(t)\delta(\mathbf{x}) - c^2 w(t)\nabla^2\delta(\mathbf{x})$ is in the null space of the forward map related to multipoles of second-order or higher. Regularization techniques for dealing with forward maps with nontrivial null spaces will be vital for multipole source inversions of higher order and should be further studied.

Another natural question to ask is: how much source anisotropy is really necessary to fit field data well? Minkoff and Symes (1997) marine reflection data for multipole source parameters together with a layered viscoelastic model, resulted in fitting 25% more of the data than was possible with any isotropic source and allowed 90% data fit to the target portion of the data. Moreover, recovered p-wave and s-wave impedance parameters matched closely the expected seismic-lithologic signature of the gas sand only when viscoelastic model and anisotropic source parameters were simultaneously estimated. The order of multipole required to achieve this degree of data fit and well log tie was $N = 6$. Obviously, the necessary order depends on many factors and varies from survey to survey.

Conclusion

This chapter presents an application of my multipole source framework on realistic seismic sources, in particular, airgun arrays. Pressure waves generated from an airgun array is modeled as a superposition of notional point-sources whose source signatures are computed via airgun modeling software AGORA, taking into consideration source-to-source interactions and the physics involved in the oscillating bubble problem. Applying the inversion strategy highlighted in the previous chapter, namely the use of preconditioners for multipole source inversions, multipole sources of zeroth- and first-order are estimated by minimizing the L^2-norm of the data misfit. Results demonstrate that roughly 84% of the data can be accounted for by an isotropic point source, while an extra 10% of data can be explained if dipole terms in the directions parallel to the plane defined by the array of airguns are included.

Chapter 7

Conclusions

The ultimate goal of seismic inversion is to obtain geophysical information about the subsurface of the earth given seismic data. Whether man-made or naturally occurring, characteristics of the seismic source are inextricably linked to the data used in the inversion process, thus a joint source-medium parameter inversion approach is considered. Crucial to the success of a joint inversion is the accuracy to which seismic sources are modeled and consequently estimated. My thesis work addresses both the forward and inverse problem of the source estimation subproblem, in particular, modeling general anisotropy of seismic sources via a truncated series of multipoles.

I present a unified mathematical and computational framework for the representation and estimation of sources via multipoles in chapters 2 and 4 respectively, where seismic waves are modeled by the acoustic and elasticity systems given by equations 2.4 and 2.5. Fundamental to my multipole framework is the notion of MPS spaces, the natural vector space structure that comes from expressing sources as linear combinations of base multipoles parametrized by MPS coefficients. I develop a flexible object-oriented implementation that encodes the MPS space concept and furthermore follows closely the underlying mathematics.

Representing seismic sources as multipoles results in having to solve PDEs with singular source terms posing fundamental difficulties for the primary numerical method used in this work, finite differences. I address these issues in chapter 3 where I construct gridded approximations to multipoles based on moment matching conditions, an extension of work by Waldén (1999), Tornberg and Engquist (2004), and Hosseini et al. (2016). My contributions consist in extending these approximations to derivatives of the delta function in higher dimensions and in connecting the discrete and continuous moment conditions. The latter implies that discrete moment conditions, in fact, generate sequences of approximations to a desired singular distribution that converge in the weak-$*$ topology. My implementation of the multipole framework systemically constructs discrete approximations to multipole sources, essentially yielding time series attached to points on a regular grid that can be fed as source functions to a finite-difference wave equation solver; this is abstractly carried out by the MPS-to-RHS linear operator.

Numerical results in chapter 4 help validate my conjecture on convergence of finite difference solutions to acoustic and elasticity equations considered here with multipole sources approximated via moment conditions. Namely, optimal convergence rates, when using a proper source approximation, are achieved away from the source location. Proving this conjecture, along with further error analysis of finite difference solutions near the source region especially for source approximations of the wrong approximation order, is the subject of future work.

In chapter 5 I study the multipole source inversion subproblem via FWI (i.e., a linear least squares problem) and the difficulties that stem from ill-conditioning of the source-to-data map. I develop a preconditioner for accelerating Krylov subspace iterative methods based on effectively redefining L^2-inner product of the MPS space to yield a better bounded forward map. My preconditioners consist of fractional derivative/integral operators whose order is chosen semi-heuristically based on the analytical solutions of the acoustic wave equation in unbounded media with multipole source terms. Results demonstrate dramatic accelerations in convergence of CG iterates and accurate source inversions for all synthetic test cases when preconditioning. I note that my preconditioning strategy is not meant to address all of the difficulties associated with multipole source inversion, but however will prove to be fundamental accelerating the source inversion subproblem for the joint source-medium inversion case. Furthermore, other regularization techniques should be investigated in conjunction with the preconditioners presented here for a comprehensive approach.

The work presented in this dissertation lays the groundwork for joint source-medium inversion via FWI. Given the separable structure of the corresponding forward map, the joint source-medium inversion problem lends itself to reducible nonlinear programming methods such as variable projection or variations thereof. In particular, my implementation of the multipole framework is compatible with the RVL implementation of variable projection method and thus can be incorporate into a joint source-medium inversion algorithm without any change either to my code or

to the RVL variable projection algorithm.

I emphasize throughout this thesis the importance of an accurate source model in the recovery of medium parameters. However, I have not dealt with several important issues, for example, the number of multipole terms required to represent a source with a given degree of anisotropy and the degree of anisotropy required for a successful inversion of field data. The first point is addressed to some degree specifically for the airgun array source; results from chapter 6 motivate the use of the multipoles of order one in capturing characteristics of an airgun array. The number of terms in the multipole expansion needed to accurately represent a given source is of course problem dependent and not known a priori in general. A future direction would be to develop an inversion algorithm that does not require an assumption on the structure of the source but instead determines the necessary multipole terms required to fit the data as the inversion progresses. An *Occam's inversion* strategy, also referred to as minimum structure inversion (Constable et al., 1987; Aster et al., 2005), could potentially be applied to develop such an algorithm. Lastly, the degree of anisotropy (i.e., number of multipole terms) required for a successful inversion of field data will depend on many factors and will vary from survey to survey. Related to this matter will be the interplay between source and medium anisotropy. In other words, how does source anisotropy affect the recovery of medium parameters? Will source anisotropy regularize the joint inversion problem or lead to source-medium ambiguities?

Appendix A

Multipole Sources and Seismic Moment Tensors

Consider the elasticity equations in second-order form over some volume $V \subset \mathbb{R}^3$ with exterior surface ∂V,

$$\begin{aligned} \frac{\partial^2}{\partial t^2} u_i(\mathbf{x},t) - \beta(\mathbf{x}) \frac{\partial}{\partial x_j} \left(c_{ijmn}(\mathbf{x}) \frac{\partial}{\partial x_m} u_n(\mathbf{x},t) \right) = f_i(\mathbf{x},\mathbf{t}), \quad & \mathbf{x} \in V \setminus \partial V, \\ \mathbf{u}(\mathbf{x},t) = \mathbf{0}, \quad & \mathbf{x} \in \partial V, \\ \mathbf{u}(\mathbf{x},t) = \mathbf{0}, \quad & \forall t << 0, \end{aligned} \tag{A.1}$$

denoting the i^{th}-component of the displacement field by u_i. Using Green's functions we can write solution to equation A.1 as a convolution in time and space with source term f_i, that is

$$u_i(\mathbf{x},t) = \int_V d\mathbf{x}' \; f_n(\mathbf{x}',t) * G_{in}(\mathbf{x}-\mathbf{x}',t) \tag{A.2}$$

with '$*$' denoting convolution in time and where G_{in} is the solution to equation A.1 with an impulsive point-source,

$$\begin{aligned} \frac{\partial^2}{\partial t^2} G_{in}(\mathbf{x},t) - \beta(\mathbf{x}) \frac{\partial}{\partial x_j} \left(c_{ijk\ell}(\mathbf{x}) \frac{\partial}{\partial x_\ell} G_{kn}(\mathbf{x},t) \right) = \delta_{in}\delta(\mathbf{x})\delta(t), \quad & \forall \mathbf{x}, \in V \setminus \partial V, \\ G_{in}(\mathbf{x},t) = 0, \quad & \forall \mathbf{x} \in \partial V. \\ G_{in}(\mathbf{x},t) = 0, \quad & \forall t << 0. \end{aligned} \tag{A.3}$$

Now suppose the region of interest V has an internal surface Σ, with ν denoting the positive orientation of Σ, see figure A.1. Slip between the internal surfaces Σ^+ and Σ^- (modeling earthquake sources as a slip in a fault) results in a discontinuity in the displacement field and continuity of traction across Σ. Assuming no external forces (i.e., $f_i \equiv 0$ in equation A.1) one can derive the following expression for the displacement field u_i in terms of the jump discontinuity across Σ (see Aki and Richards (2002) for a detailed derivation):

$$u_n(\mathbf{x}, t) = -\int_\Sigma d\xi \; \nu_j(\xi) c_{ijpq}(\xi) [\![u_i(\xi, t)]\!] * \frac{\partial}{\partial x_q} G_{np}(\mathbf{x} - \xi, t), \tag{A.4}$$

where I denote the jump discontinuity across the internal surface by $[\![\cdot]\!]$. It should be mentioned that the displacement field given in equation A.2 satisfies the elasticity equations in the interior of the domain V excluding Σ, while the Green's function is assumed to satisfy equation A.3 as is, in the interior of V including Σ.

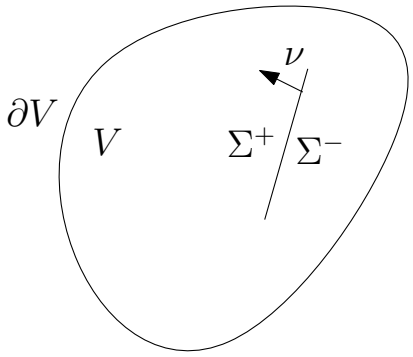

Figure A.1 : Body V with surface ∂V and internal surface Σ oriented by ν.

Equation A.4 can be restated in the form of equation A.2 with an effective body force $\tilde{f}_p$,

$$\tilde{f}_p(\mathbf{x},t) = \int_\Sigma d\xi\ \mathcal{M}_{pq}(\xi,t)\frac{\partial}{\partial x_q}\delta(\mathbf{x}-\xi), \tag{A.5}$$

with $\mathcal{M}_{pq}$ denoting the *moment tensor density* defined as

$$\mathcal{M}_{pq}(\xi,t) = \nu_j(\xi)c_{ijpq}(\xi)[\![u_i(\xi,t)]\!], \quad \text{for} \quad \xi \in \Sigma.$$

The p-component of the effective body force $\tilde{f}_p$, according to equation A.5, can be interpreted as the superposition of combined dipole terms $\frac{\partial}{\partial \xi_q}\delta(\mathbf{x}-\xi)$ with magnitude $\mathcal{M}_{pq}(\xi,t)$ as a function of time and position in surface Σ. More specifically, $\mathcal{M}_{pq}$ corresponds to the magnitude of a point-dipole (also referred to as a couple) in the *p-direction* with *q-orientation*. Figure A.2 illustrates the possible directions and orientations for the different components of the seismic moment tensor density in 3D.

The displacement field as computed by equation A.4 can be approximated by replacing the Green's function with its truncated Taylor series centered at $\mathbf{x}-\xi^* \in V$ for some $\xi^* \in \Sigma$, namely

$$\begin{aligned} u_n(\mathbf{x},t) &\approx \int_\Sigma d\xi\ \mathcal{M}_{pq}(\xi,t) * \frac{\partial}{\partial x_q}\left(\sum_{|\alpha|=0}^{N}(-1)^{|\alpha|}\frac{(\xi-\xi^*)^\alpha}{\alpha!}D^\alpha G_{np}(\mathbf{x}-\xi^*,t)\right) \\ &= \sum_{|\alpha|=0}^{N}\frac{(-1)^{|\alpha|}}{\alpha!}\frac{\partial}{\partial x_q}D^\alpha G_{np}(\mathbf{x}-\xi^*,t) * \left(\int_\Sigma d\xi\ \mathcal{M}_{pq}(\xi,t)(\xi-\xi^*)^\alpha\right), \end{aligned}$$

using multi-index $\alpha = (\alpha_1,\alpha_2,\alpha_3)$. The term in parenthesis in the last equation

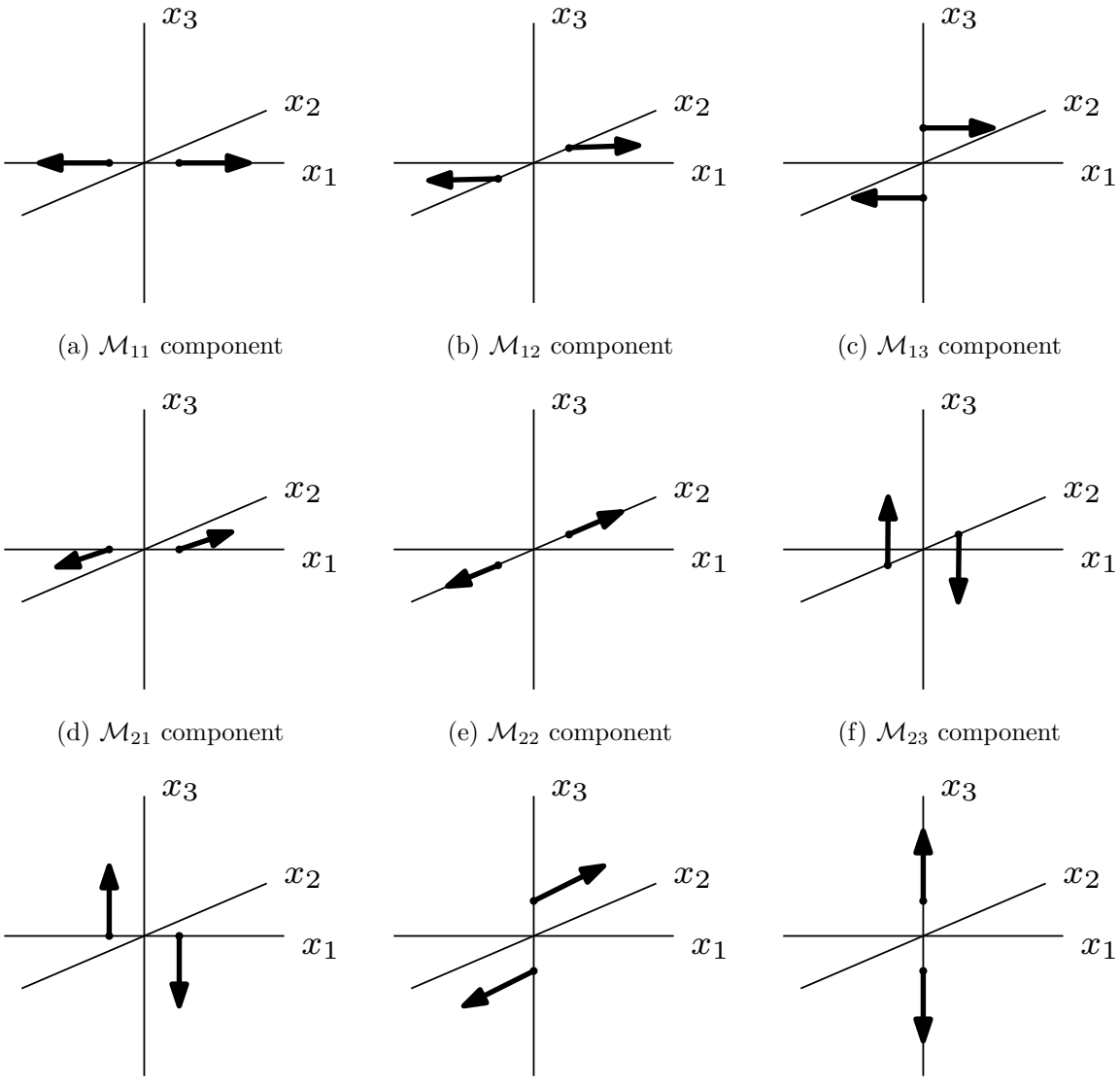

(a) $\mathcal{M}_{11}$ component (b) $\mathcal{M}_{12}$ component (c) $\mathcal{M}_{13}$ component

(d) $\mathcal{M}_{21}$ component (e) $\mathcal{M}_{22}$ component (f) $\mathcal{M}_{23}$ component

(g) $\mathcal{M}_{31}$ component (h) $\mathcal{M}_{32}$ component (i) $\mathcal{M}_{33}$ component

Figure A.2 : Corresponding point-couples for different $\mathcal{M}_{pq}$ components.

alludes to the definition of the *stress moment-tensor*. In standard notation, the N-order stress moment tensor is defined as the following $(N+2)$-order tensor,

$$\mathcal{M}_{ij;k_1k_2\ldots k_N}(\xi^*,t)=\int_\Sigma d\xi\ \mathcal{M}_{ij}(\xi,t)(\xi_{k_1}-\xi^*_{k_1})(\xi_{k_2}-\xi^*_{k_2})\cdots(\xi_{k_N}-\xi^*_{k_N})$$

for $i,j,k_1,k_2,\cdots,k_N=1,2,3$. I introduce an alternative, but equivalent, definition of the stress moment tensor using multi-index notation, for some $|\alpha|=N$,

$$\mathcal{M}^{(N)}_{ij;\alpha}(\xi^*,t)=\int_\Sigma d\xi\ \mathcal{M}_{ij}(\xi,t)(\xi-\xi^*)^\alpha. \tag{A.7}$$

Thus the approximation for displacement field takes the form of a multi-channel convolution with stress moment tensors and derivatives of the Green's function,

$$u_n(\mathbf{x},t)\approx\sum_{\substack{|\alpha|=n\\ n=0}}^{N}\frac{(-1)^{|\alpha|}}{\alpha!}\frac{\partial}{\partial x_q}D^\alpha G_{np}(\mathbf{x}-\xi^*,t)*\mathcal{M}^{(n)}_{ij;\alpha}(\xi^*,t). \tag{A.8}$$

Similar to equation A.4, approximation A.8 can be expressed in terms of convolution in time-space with an effective body force which I denote by $\tilde{\tilde{f}}_p$,

$$\tilde{\tilde{f}}_p(\mathbf{x},t)=-\sum_{\substack{|\alpha|=n\\ n=0}}^{N}\frac{1}{\alpha!}\mathcal{M}^{(n)}_{pq;\alpha}(\xi^*,t)\frac{\partial}{\partial x_q}D^\alpha\delta(\mathbf{x}-\xi^*). \tag{A.9}$$

Comparing effective body forces in equations A.5 and A.9 it is observed that approximation A.8 is equivalent to approximating $\tilde{f}_p$, the superposition of point dipoles

distributed over Σ, by a single multipole point-source centered at ξ^*. Thus the use of stress moment tensors to model earthquake source mechanisms is a particular application of the multipole approximation, and hence fits into with my MPS framework. Furthermore, the stress moment tensors play a role similar to that of the MPS coefficient.

Appendix B

Analytical Solutions to Wave Equation with Multipole Sources

Consider the d-dimensional ($d = 1, 2, 3$) acoustic wave equation in an unbounded homogenous medium with homogenous initial conditions and some causal source term f (i.e., $f(\mathbf{x}, t) = 0$ for $t << 0$),

$$\left(\frac{\partial}{\partial t^2} - c^2\nabla^2\right) p(\mathbf{x}, t) = f(\mathbf{x}, t), \qquad p(\mathbf{x}, t) = 0, \quad t << 0 \tag{B.1}$$

for pressure field p, where $c = \sqrt{\beta\kappa}$ is the speed of sound or wave velocity. Analytical solutions to equation B.1 is given by convolving source term f in time and space with the causal Green's function G which solves equation B.1 with an impulsive point-source,

$$\left(\frac{\partial}{\partial t^2} - c^2\nabla^2\right) G(\mathbf{x}, t) = \delta(t)\delta(\mathbf{x}), \qquad G(\mathbf{x}, t) = 0, \quad t << 0.$$

In particular, the Green's function has a closed form for the unbounded homogeneous problem:

$$G(\mathbf{x},t) = \begin{cases} \dfrac{1}{2c} H(t - \frac{|\mathbf{x}|}{c}), & \text{for } d = 1; \\ \dfrac{1}{2\pi c} \dfrac{H(t - \frac{|\mathbf{x}|}{c})}{\sqrt{c^2 t^2 - |\mathbf{x}|^2}}, & \text{for } d = 2; \\ \dfrac{1}{4\pi c^2} \dfrac{\delta(t - \frac{|\mathbf{x}|}{c})}{|\mathbf{x}|}, & \text{for } d = 3; \end{cases}$$

with H denoting the Heaviside function and δ the Dirac delta function. For the special case where f is a point source, e.g., $f(\mathbf{x},t) = \tilde{w}(t)\delta(\mathbf{x})$, the pressure field reduces to a convolution in time,

$$p(\mathbf{x},t) = G(\mathbf{x},t) * \tilde{w}(t). \tag{B.2}$$

Analytical solutions to the acoustic wave equation with multipole sources are derived by differentiating equation B.2 in space. Let p be the analytical solution to the acoustic wave equation with point source $\tilde{w}(t)\delta(\mathbf{x})$ as given by equation B.2. Given multi-index $\mathbf{s} = (s_1, ..., s_d)$, it follows that $D^{\mathbf{s}}p$ is the solution to the acoustic wave equation with multipole source $\tilde{w}(t)D^{\mathbf{s}}\delta(\mathbf{x})$; this follows from linearity of the wave equation and derivative $D^{\mathbf{s}}$ operator, and the fact that they commute (assuming necessary differentiability of p). In the following subsections I derive explicit formulas for analytical solutions to the acoustic wave equation with multipole sources, that is $D^{\mathbf{s}}p$, is several dimensions.

1-D Analytical Solutions

Let $\tilde{w}^{(-1)}$ denote the anti-derivative of $\tilde{w}$, then it follows that $p(x,t) = \frac{1}{2c}\tilde{w}^{(-1)}(\tau)$, where $\tau = t - |x|/c$ is referred to as the *travel time*. Thus,

$$D^s p(x,t) = \frac{1}{2c}\left(\frac{\partial}{\partial x}\right)^s \tilde{w}^{(-1)}(\tau).$$

For $s = 1$, I use the chain-rule to differentiate with respect to x,

$$\frac{\partial}{\partial x}p(x,t) = -\frac{1}{2c^2}\tilde{w}(\tau)\ \mathrm{sgn}(x)$$

where $\mathrm{sgn}(x)$ is the *sign function*,

$$\mathrm{sgn}(x) = \begin{cases} -1, & x \leq 0 \\ \\ 1, & x > 0. \end{cases}$$

and is the weak derivative of $|x|$. Applying another derivative yields,

$$\frac{\partial^2}{\partial x^2}p(x,t) = \frac{1}{2c^3}\tilde{w}'(\tau) - \frac{1}{c^2}\tilde{w}(\tau)\delta(x)$$

where I have used the fact that $\mathrm{sign}^2(x) \equiv 1$ and that $\frac{d}{dx}\mathrm{sign}(x) = 2\delta(x)$ in the weak sense.

2-D Analytical Solutions

The analytical solution for the 2-D case is special in that it yields an integral with a singular kernel,

$$p(\mathbf{x},t) = \frac{1}{2\pi c}\int_{\mathbb{R}} ds\ \frac{H(s-\frac{|\mathbf{x}|}{c})}{\sqrt{c^2s^2-|\mathbf{x}|^2}}\tilde{w}(t-s).$$

Applying a change of variables will simplifies the expression above and eliminates the singularity; take $\sigma = \sqrt{s-\frac{|\mathbf{x}|}{c}}$, then the resulting integral takes the form

$$p(\mathbf{x},t) = \frac{1}{\pi c^2}\int_0^{\sqrt{\tau}} d\sigma\ \tilde{w}(\tau-\sigma^2)\Omega(\mathbf{x},\sigma) \tag{B.3}$$

where I have introduced the function $\Omega(\mathbf{x},\sigma)$ in order to simplify upcoming derivations;

$$\Omega(\mathbf{x},\sigma) = \frac{1}{\sqrt{\sigma^2+2\frac{|\mathbf{x}|}{c}}}.$$

To compute partial derivatives of p I will enact Leibniz rule for differentiation: Let

$$\phi(x,t,\sigma) = \tilde{w}(\tau-\sigma^2)\Omega(\mathbf{x},\sigma),$$

then

$$\begin{aligned}\frac{\partial}{\partial x_i}\left(\int_{a(\mathbf{x},t)}^{b(\mathbf{x},t)} d\sigma\ \phi(\mathbf{x},t,\sigma)\right) &= \phi(\mathbf{x},t,b(\mathbf{x},t))\cdot\frac{\partial b}{\partial x_i}(\mathbf{x},t) - \phi(\mathbf{x},t,a(\mathbf{x},t))\cdot\frac{\partial a}{\partial x_i}(\mathbf{x},t)\\ &\quad + \int_{a(\mathbf{x},t)}^{b(\mathbf{x},t)} d\sigma\ \frac{\partial}{\partial x_i}\phi(\mathbf{x},t,\sigma),\end{aligned}$$

where $a(\mathbf{x},t) \equiv 0$ and $b(\mathbf{x},t) = \sqrt{\tau} = \sqrt{t - |\mathbf{x}|/c}$. Note that

$$\phi(\mathbf{x},t,b(\mathbf{x},t)) = \frac{\tilde{w}(\tau-\tau)}{\sqrt{\tau + 2\frac{|\mathbf{x}|}{c}}} = 0$$

since $\tilde{w}$ is causal, that is $\tilde{w}(0) = 0$. Moreover,

$$\begin{aligned}\frac{\partial}{\partial x_i}\phi(\mathbf{x},t,\sigma) &= \tilde{w}'(\tau-\sigma^2)\left(-\frac{\gamma_i}{c}\right)\Omega(\mathbf{x},\sigma) + \tilde{w}(\tau-\sigma^2)\left(-\frac{1}{2}\right)\Omega^3(\mathbf{x},\sigma)\left(\frac{2\gamma_i}{c}\right) \\ &= -\frac{\gamma_i}{c}\Big\{\tilde{w}'(\tau-\sigma^2)\Omega(\mathbf{x},\sigma) + \tilde{w}(\tau-\sigma^2)\Omega^3(\mathbf{x},\sigma)\Big\}.\end{aligned}$$

with $\gamma_i = \frac{\partial}{\partial x_i}|\mathbf{x}| = \frac{x_i}{r}$. Thus,

$$\frac{\partial}{\partial x_i}p(\mathbf{x},t) = -\frac{\gamma_i}{\pi c^3}\int_0^{\sqrt{\tau}} d\sigma\,\Big\{\tilde{w}'(\tau-\sigma^2)\Omega(\mathbf{x},\sigma) + \tilde{w}(\tau-\sigma^2)\Omega^3(\mathbf{x},\sigma)\Big\}.$$

3-D Analytical Solutions

Spatial derivatives of the pressure field in 3-D is quite straight forward:

$$\begin{aligned}\frac{\partial}{\partial x_i}p(\mathbf{x},t) &= -\frac{1}{4\pi c^2}\frac{\gamma_i}{|\mathbf{x}|^2}\tilde{w}(\tau) + \frac{1}{4\pi}\frac{1}{|\mathbf{x}|}\tilde{w}'(\tau)\left(-\frac{\gamma_i}{c}\right) \\ &= -\frac{1}{4\pi c^2}\left\{\frac{\gamma_i}{|\mathbf{x}|^2}\tilde{w}(\tau) + \frac{1}{c}\frac{\gamma_i}{|\mathbf{x}|}\tilde{w}'(\tau)\right\}\end{aligned}$$

I skip over some of the computations for the second derivative and instead summarize all of the derivations above in the following table.

	Source Term	Analytical Solution
1-D	$\tilde{w}(t)\delta(x)$	$\frac{1}{2c}\int_0^\tau ds\ \tilde{w}(s)$
	$\tilde{w}(t)\frac{d}{dx}\delta(x)$	$-\frac{1}{2c^2}\tilde{w}(\tau)\ \mathrm{sgn}(x)$
	$\tilde{w}(t)\frac{d^2}{dx^2}\delta(x)$	$\frac{1}{2c^3}\tilde{w}'(\tau)-\frac{1}{c^2}\tilde{w}(\tau)\delta(x)$
2-D	$\tilde{w}(t)\delta(\mathbf{x})$	$\frac{1}{\pi c^2}\int_0^{\sqrt{\tau}} d\sigma\ \tilde{w}(\tau-\sigma^2)\Omega(\mathbf{x},\sigma)$
	$\tilde{w}(t)\frac{\partial}{\partial x_i}\delta(\mathbf{x})$	$-\frac{\gamma_i}{\pi c^3}\int_0^{\sqrt{\tau}} d\sigma\ \left\{\tilde{w}'(\tau-\sigma^2)\Omega(\mathbf{x},\sigma)+\tilde{w}(\tau-\sigma^2)\Omega^3(\mathbf{x},\sigma)\right\}$
3-D	$\tilde{w}(t)\delta(\mathbf{x})$	$\frac{1}{4\pi c^2\lvert\mathbf{x}\rvert}\tilde{w}(\tau)$
	$\tilde{w}(t)\frac{\partial}{\partial x_i}\delta(\mathbf{x})\tilde{w}(t)$	$-\frac{1}{4\pi c^2}\left\{\frac{1}{c}\frac{\gamma_i}{\lvert\mathbf{x}\rvert}\tilde{w}'(\tau)+\frac{\gamma_i}{\lvert\mathbf{x}\rvert^2}\tilde{w}(\tau)\right\}$
	$\tilde{w}(t)\frac{\partial^2}{\partial x_j\partial x_i}\delta(\mathbf{x})$	$\frac{1}{4\pi c^2}\left\{\frac{\gamma_i\gamma_j}{c^2\lvert\mathbf{x}\rvert}\tilde{w}''(\tau)-\frac{\delta_{ij}-3\gamma_i\gamma_j}{c\lvert\mathbf{x}\rvert^2}\tilde{w}'(\tau)-\frac{\delta_{ij}-3\gamma_i\gamma_j}{\lvert\mathbf{x}\rvert^3}\tilde{w}(\tau)\right\}$

Table B.1 : Analytical solutions to wave equation with multipole point sources in 1-D, 2-D, and 3-D.

Summary

Inspection of the analytical solutions given above, starting with 1-D, reveals a pattern as the multipole order is increased. Namely, the resulting pressure field from a multipole source $f(\mathbf{x},t)=\tilde{w}(t)\frac{d^s}{dx^s}\delta(x)$ resembles the source wavelet $\tilde{w}$ scaled by c,

$$p(x,t)\sim\frac{1}{c^{s+1}}\left(\frac{d}{dt}\right)^{s-1}\tilde{w}(t) \tag{B.4}$$

where the derivative of negative order is interpreted as the antiderivative. A similar observation is made for 3-D when considering only terms that dominate as $|\mathbf{x}|\to\infty$, also referred to as *far-field* terms. Thus,

$$p(\mathbf{x},t) \sim \frac{1}{c^{s+2}} \left(\frac{d}{dt}\right)^{s} \tilde{w}(t). \tag{B.5}$$

The 2-D case is a bit tricky due to the integrand term Ω. Considering only far-field terms, it turns out that the integro-differential form of 2-D analytical solutions is quiet similar to the (Caputo) fractional derivative/integral; see appendix C for a short overview of fractional calculus operators. In particular,

$$p(\mathbf{x},t) \sim \frac{1}{c^{s+2}} \left(\frac{d}{dt}\right)^{s-1/2} \tilde{w}(t). \tag{B.6}$$

The discussion above concerns analytical solutions to the acoustic wave equation, that is the second order form. Similar derivations follow for the first order system (equation 2.4) with scalar source terms $f(\mathbf{x},t) = w(t)D^{\mathbf{s}}\delta(\mathbf{x})$ after realizing $\tilde{w}(t) = \frac{d}{dt}w(t)$. This results in equations B.4, B.6, and B.5 with an extra derivative.

I provide some plots to further validate my claim for the 2-D case. Figure B.1 contains single trace plots of pressure fields due to a scalar multipole $f(\mathbf{x},t) = w(t)D^{\mathbf{s}}\delta(\mathbf{x},t)$ in an unbounded acoustic medium for different multi-indexes $\mathbf{s}$. The MPS coefficient $w(t)$ used here is a Ricker wavelet with peak frequency of $10Hz$, see figure 5.1a. Plots show almost identical waveforms when comparing pressure traces with fractional derivative of the MPS coefficient $w(t)$ and a similar drop in magnitude with increasing MPS order. The latter point will be of importance in when inverting for multipole sources of mixed order.

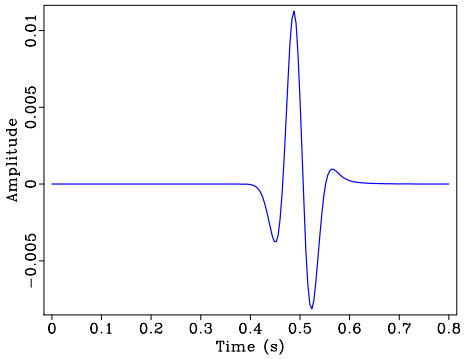

(a) Pressure field $p(\mathbf{x}_r, t)$ for $\mathbf{s} = (0, 0)$.

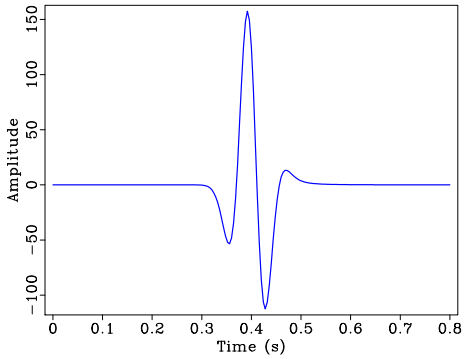

(b) Fractional derivative of MPS coefficient, $(\frac{d}{dt})^{1/2} w_1(t)$.

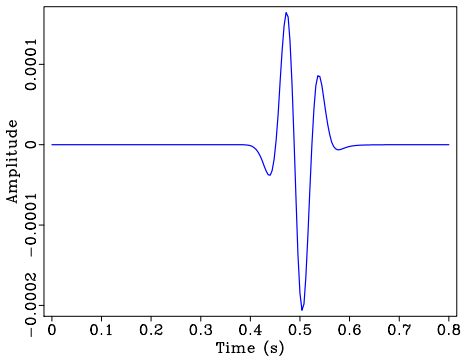

(c) Pressure field $p(\mathbf{x}_r, t)$ for $\mathbf{s} = (0, 1)$.

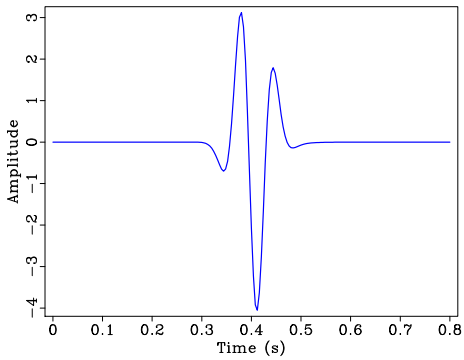

(d) Fractional derivative of MPS coefficient, $\frac{1}{c}(\frac{d}{dt})^{3/2} w_1(t)$.

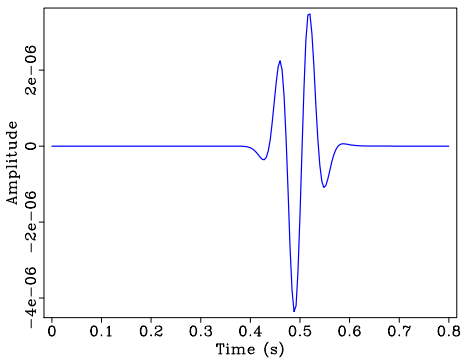

(e) Pressure field $p(\mathbf{x}_r, t)$ for $\mathbf{s} = (0, 2)$.

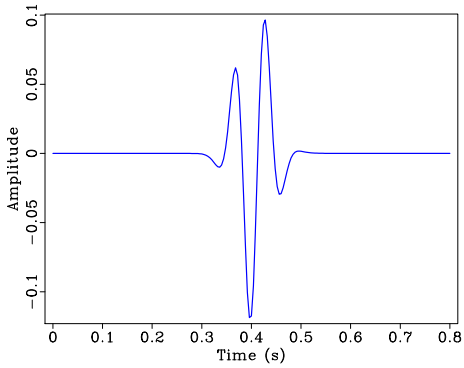

(f) Fractional derivative of MPS coefficient, $\frac{1}{c^2}(\frac{d}{dt})^{5/2} w_1(t)$.

Figure B.1 : Pressure waveforms (left column) and fractional time derivatives (right column) related to scalar multipole source $f(\mathbf{x}, t) = w_1(t) D^{\mathbf{s}} \delta(\mathbf{x} - \mathbf{x}^*)$ in a 2-D homogeneous unbounded acoustic medium. MPS coefficient $w_1(t)$ is a Ricker wavelet with peak frequency of $10Hz$. Source location $\mathbf{x}^* = (-1km, 1km)$ and receiver location $\mathbf{x}_r = (-800m, 800m)$.

Appendix C

Fractional Derivative/Integral Operators

I follow the Grünwald-Letnikov definition of the left fractional derivative as a basis for a numerical implementation of fractional derivatives/integrals; see Li and Zeng (2015) for further details on numerical methods for fractional calculus. The left fractional derivative of order $\alpha > 0$, of a given function $f(t)$, $t \in (0, T)$, is defined as

$$D^{\alpha}_{GL} f(t) := \lim_{\substack{\Delta t \to 0 \\ N\Delta t = t}} \Delta t^{-\alpha} \sum_{j=0}^{N} (-1)^j \binom{\alpha}{j} f(t - j\Delta t), \tag{C.1}$$

where $\binom{\alpha}{j}$ is interpreted to be the generalized binomial coefficient for $\alpha \in \mathbb{R}$, i.e.,

$$\binom{\alpha}{j} = \frac{\Gamma(\alpha + 1)}{\Gamma(\alpha - j + 1) j!}.$$

The discrete operator, which we will simply denote by D^{α}, is given by not taking the limit in equation C.1, thus yielding a finite-difference-like approach to computing fractional derivatives: Suppose the time interval $(0, T)$ uniformly discretized into N_t segments of length $\Delta t = \frac{T}{N_t}$. The *discrete fractional derivative* of order $\alpha > 0$, for f

at time $t = n\Delta t$, for $n = 0, 1, ..., N_t$, is defined as

$$D^{\alpha} f(t) := \Delta t^{-\alpha} \sum_{j=0}^{N^*} (-1)^j \frac{\Gamma(\alpha+1)}{\Gamma(\alpha-j+1)j!} f((n-j)\Delta t). \tag{C.2}$$

where

$$N^* = \begin{cases} \min(n, \alpha), & \alpha \in \mathbb{N}, \\ n, & \text{otherwise.} \end{cases}$$

The discrete fractional integral of order $\alpha > 0$ is derived by taking $\alpha \to -\alpha$ in equation C.1, and making sense out of the binomial coefficients. For $\alpha, j \in \mathbb{N}$, binomial coefficients with $\alpha \to -\alpha$ gives

$$\begin{aligned} \binom{-\alpha}{j} &= \frac{-\alpha(-\alpha-1)\cdots(-\alpha-j+1)}{j!}, \\ &= (-1)^j \frac{\alpha(\alpha+1)\cdots(\alpha+j-1)}{j!}, \\ &= (-1)^j \frac{(\alpha+j-1)!}{(\alpha-1)!j!}. \end{aligned}$$

The *discrete fractional integral* of order $\alpha > 0$, for f at time $t = n\Delta t$, for $n = 0, 1, ..., N_t$, is defined as

$$D^{-\alpha} f(t) := \Delta t^{\alpha} \sum_{j=0}^{n} \frac{\Gamma(\alpha+j)}{\Gamma(\alpha)j!} f((n-j)\Delta t). \tag{C.4}$$

Bibliography

Aki, K. and Richards, P. G. (2002). *Quantitative seismology / Keiiti Aki, Paul G. Richards.* Sausalito, Calif. : University Science Books, c2002.

Aster, R. C., Borchers, B., and Thurber, C. H. (2005). *Parameter estimation and inverse problems.* Elsevier Academic Press, Amsterdam, The Netherlands.

Barker, D. and Landrø, M. (2013). An alternative method for modeling close-range interactions between air guns. *Geophysics*, 79(2):P1–P7.

Bube, K., Lailly, P., Sacks, P., Santosa, F., and Symes, W. W. (1988). Simultaneous determination of source wavelet and velocity profile using impulsive point-source reflections from a layered fluid. *Geophysical Journal International*, 95(3):449–462.

Caldwell, J. and Dragoset, W. (2000). A brief overview of seismic air-gun arrays. *The leading edge*, 19(8):898–902.

Cohen, G. C. (2002). *Higher Order Numerical Methods for Transient Wave Equations.* Springer, New York.

Cohen, J. K. and Stockwell, J. J. W. (2015). CWP/SU: Seismic Unix release no. 44: a free package for seismic research and processing. Center for Wave Phenomena, Colorado School of Mines.

Constable, S. C., Parker, R. L., and Constable, C. G. (1987). Occam's inversion: A practical algorithm for generating smooth models from electromagnetic sounding data. *Geophysics*, 52(3):289–300.

Courant, R. and Hilbert, D. (1962). *Methods of Mathematical Physics*, volume II. Wiley-Interscience, New York.

Delprat-Jannaud, F. and Lailly, P. (2005). A fundamental limitation for the reconstruction of impedance profiles from seismic data. *Geophysics*, 70(1):R1–R14.

Eaton, D. W. and Forouhideh, F. (2010). Microseismic moment tensors: The good, the bad and the ugly. *CSEG Recorder*, 35(9):45–49.

Epanomeritakis, I., Akcelik, V., Ghattas, O., and Bielak, J. (2009). A Newton-cg method for large-scale three-dimensional elastic full-waveform seismic inversion. *Inverse Problems*, 24:24:034015 (26pp).

Evans, L. C. (1997). Partial differential equations and monge-kantorovich mass transfer. *Current developments in mathematics*, 1997(1):65–126.

Fehler, M. and Keliher, J. (2011). *SEAM Phase 1: Challenges of Subsalt Imaging in Tertiary Basins, with Emphasis on Deepwater Gulf of Mexico*. Society of Exploration Geophysicists, Tulsa.

Fomel, S. (2009). Madagascar web portal. http://www.reproducibility.org, accessed 5 April 2009.

Giles, B. and Johnston, R. (1973). System approach to air-gun array design. *Geophysical Prospecting*, 21(1):77–101.

Gilmore, F. R. (1952). The growth or collapse of a spherical bubble in a viscous compressible liquid.

Golub, G. H. and Pereyra, V. (1973). The differentiation of pseudo-inverses and nonlinear least squares problems whose variables separate. *SIAM Journal on numerical analysis*, 10(2):413–432.

Gustafsson, B. and Mossberg, E. (2004). Time compact high order difference methods for wave propagation. *SIAM Journal on Scientific Computing*, 26:259–271.

Gustafsson, B. and Wahlund, P. (2004a). Time compact difference methods for wave propagation in discontinuous media. *SIAM Journal on Scientific Computing*, 26:272–293.

Gustafsson, B. and Wahlund, P. (2004b). Time compact high order difference methods for wave propagation, 2d. *Journal of Scientific Computing*, 25:195–211.

Hörmander, L. (1969). *Linear Partial Differential Operators*. Springer Verlag, New York, 3rd edition.

Hosseini, B., Nigam, N., and Stockie, J. M. (2016). On regularizations of the dirac delta distribution. *Journal of Computational Physics*, 305:423–447.

Hu, W., Abubakar, A., and Habashy, T. (2007). Application of the nearly perfectly matched layer in acoustic wave modeling. *Geophysics*, 72:SM169–SM176.

Jost, M. u. and Herrmann, R. (1989). A students guide to and review of moment tensors. *Seismological Research Letters*, 60(2):37–57.

Julian, B. R., Miller, A. D., and Foulger, G. (1998). Non-double-couple earthquakes 1. theory. *Reviews of Geophysics*, 36(4):525–549.

Kirkwood, J. and Bethe, H. (1942). Osrd report no. 588.

Koch, K. (1991). Moment tensor inversion of local earthquake data?i. investigation of the method and its numerical stability with model calculations. *Geophysical Journal International*, 106(2):305–319.

Komatisch, D., Barnes, C., and Tromp, J. (2000). Simulation of anisotropic wave propagation based upon a spectral element method. *Geophysics*, 65:1251–1260.

Kouri, D., Ridzal, D., van Bloemen Waanders, B., and von Winckel, G. (2015). ROL Web page (http://trilinos.org/packages/rol).

Landrø, M. and Sollie, R. (1992). Source signature determination by inversion. *Geophysics*, 57(12):1633–1640.

Levander, A. (1988). Fourth-order finite-difference pw seismograms. *Geophysics*, 53(11):1425.

Lewis, R. M. (1989). *Source-velocity identification for a layered model of reflection seismology*. PhD thesis, PhD thesis, Department of Mathematical Sciences, Rice University, Houston, Texas, USA.

Li, C. and Zeng, F. (2015). *Numerical methods for fractional calculus*, volume 24. CRC Press.

Li, J., He, Y.-M., and Yao, Z.-X. (2006). Source finiteness and rupture propagation using higher-degree moment tensors. *Bulletin of the Seismological Society of America*, 96(4A):1241–1256.

MacGillivray, A. (2006). *An acoustic study of seismic airgun noise in Queen Charlotte Basin*. PhD thesis, MSc Thesis.

Minkoff, S. E. and Symes, W. W. (1995). Estimating the energy source and reflectivity by seismic inversion. *Inverse Problems*, 11(2):383.

Minkoff, S. E. and Symes, W. W. (1997). Full waveform inversion of marine reflection data in the plane-wave domain. *Geophysics*, 62(2):540–553.

Moczo, P., Robertsson, J. O. A., and Eisner, L. (2006). The finite-difference time-domain method for modeling of seismic wave propagation. *Advances in Geophysics*, 48:421–516.

Öktem, O. e. a. (2016). Operator discretization library. https://github.com/odlgroup/odl.

Padula, A. D., Symes, W., and Scott, S. D. (2009). A software framework for the abstract expression of coordinate-free linear algebra and optimization algorithms. *ACM Transactions on Mathematical Software*, 36:8:1–8:36.

Ramm, A. (1985). Inversion of the backscattering data and a problem of integral geometry. *Physics Letters A*, 113(4):172–176.

Rayleigh, L. (1917). Viii. on the pressure developed in a liquid during the collapse of a spherical cavity. *The London, Edinburgh, and Dublin Philosophical Magazine and Journal of Science*, 34(200):94–98.

Rickett, J. (2013). The variable projection method for waveform inversion with an unknown source function. *Geophysical Prospecting*, 61(4):874–881.

Robinson, E. A. (1957). Predictive decomposition of seismic traces. *Geophysics*, 22(4):767–778.

Ruhe, A. and Wedin, P. Å. (1980). Algorithms for separable nonlinear least squares problems. *Siam Review*, 22(3):318–337.

Safar, M. (1976). Efficient design of air-gun arrays. *Geophysical Prospecting*, 24(4):773–787.

Santosa, F. and Symes, W. W. (2000). Multipole representation of small acoustic sources. *Chinese Journal of Mechanics*, 16:15–21.

Sertleka, H. Ö. and Ainslieb, M. A. (2015). Airgun source model (agora): Its application for seismic surveys sound maps in the dutch north sea. https://www.researchgate.net, accessed 28 February 2017.

Shearer, P. M. (2009). *Introduction to seismology*. Cambridge University Press.

Song, F. and Toksöz, M. N. (2011). Full-waveform based complete moment tensor inversion and source parameter estimation from downhole microseismic data for hydrofracture monitoring. *Geophysics*, 76(6):WC103–WC116.

Stump, B. W. and Johnson, L. R. (1982). Higher-degree moment tensors – the importance of source finiteness and rupture propagation on seismograms. *Geophysical Journal International*, 69(3):721–743.

Symes, W. (2014). IWAVE structure and basic use cases. In *TRIP 2014 Annual Report*. The Rice Inversion Project, CAAM, MS 134, Rice University, Houston TX 77251-1892 USA. available summer 2015.

Symes, W. W., Sun, D., and Enriquez, M. (2011). From modelling to inversion: designing a well-adapted simulator. *Geophysical Prospecting*, 59:814–833. DOI:10.1111/j.1365-2478.2011.00977.x.

Tornberg, A.-K. and Engquist, B. (2004). Numerical approximations of singular source terms in differential equations. *Journal of Computational Physics*, 200(2):462–488.

Ulrych, T. (1971). Application of homomorphic deconvolution to seismology. *Geophysics*, 36(4):650–660.

Virieux, J. (1986). P-SV wave propagation in heterogeneous media; velocity-stress finite-difference method. *Geophysics*, 51(4):889–901.

Waldén, J. (1999). On the approximation of singular source terms in differential equations. *Numerical Methods for Partial Differential Equations*, 15(4):503–520.

Wang, K., Krebs, J. R., Hinkley, D., Baumstein, A., et al. (2009). Simultaneous full-waveform inversion for source wavelet and earth model. In *SEG Int'l. Expo. & Ann. Meeting, Expanded Abstracts*, pages 2537–2541.

Yilmaz, O. (2001). Seismic data processing. In *Investigations in Geophysics No. 10*. Society of Exploration Geophysicists, Tulsa.

Zhou, C., Schuster, G. T., Hassanzadeh, S., and Harris, J. M. (1997). Elastic wave equation traveltime and waveform inversion of crosswell data. *Geophysics*, 62(3):853–868.

Ziolkowski, A. (1970). A method for calculating the output pressure waveform from an air gun. *Geophysical Journal International*, 21(2):137–161.

Ziolkowski, A. (1991). Why don't we measure seismic signatures? *Geophysics*, 56(2):190–201.

Ziolkowski, A., Parkes, G., Hatton, L., and Haugland, T. (1982). The signature of an air gun array: Computation from near-field measurements including interactions. *Geophysics*, 47(10):1413–1421.